



Faculty of Sciences

Department of Physics and Astronomy

**INVESTIGATION OF $\text{Cu}_2\text{ZnSnS}_4$ (CZTS) NANOSTRUCTURED
MATERIAL SYSTEM FOR ENERGY CONVERSION**

by

MOMPOLOKI KEFOSITSE

Student ID number: 14001893

BSc (Physics) (BIUST)

A Thesis Submitted to the Faculty of Sciences in Partial Fulfilment of the Requirements
for the Award of the Degree of Master of Science in Physics of BIUST

Supervisor(s): Prof, Mario Einax

Department of Physics and Astronomy

Faculty of Science, BIUST

einaxm@biust.ac.bw

March, 2022

DECLARATION REGARDING THE WORK AND COPYRIGHT

Candidate: MOMPLOKI KEFOSITSE

Student ID: 14001893

Thesis Titled: INVESTIGATION OF $\text{Cu}_2\text{ZnSnS}_4$ (CZTS) NANOSTRUCTURED MATERIAL SYSTEM FOR ENERGY CONVERSION

I, the **Mompoloki Kefositse**, certify that the Thesis is all my own original work and that I have not obtained a degree in this University or elsewhere on the basis of any of this work.

(If the thesis is based on a group project, then the student must indicate the extent of her / his contribution, with reference to any other theses submitted or published by each collaborator in the project, and a declaration to this effect must be included in the thesis)

This dissertation/thesis is copyright material protected under the Berne Convention, the Copyright and Neighbouring Rights Act, Act. No. 8 of 2000 and other international and national enactments, in that behalf, on intellectual property. It must not be reproduced by any means, in full or in part, except for short extracts in fair dealing; for researcher private study, critical scholarly review or discourse with an acknowledgement, without the written permission of the office of the Postgraduate School, on behalf of both the author and the BIUST.

Signed: *M. Kefositse* Date: 07/03/2022

Primary Supervisor (please write in caps or type) **PROF. MARIO EINAX**

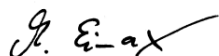
I, the Candidate's **Primary Supervisor**, hereby confirm that I have inspected the above titled thesis and, to the best of my knowledge, it is based on the original work of the candidate.

Signed: *J. Einax* Date: 07/03/2022

CERTIFICATION

The undersigned certifies that he has read and hereby recommends for acceptance by the College of Science a dissertation titled: **INVESTIGATION OF $\text{Cu}_2\text{ZnSnS}_4$ (CZTS) NANOSTRUCTURED MATERIAL SYSTEM FOR ENERGY CONVERSION**, in fulfilment of the requirements for the degree of Master of Science in Physics (MSc Physics) of the Botswana International University of Science and Technology

Supervisor(s):



Prof Mario Einax

(Supervisor)

Date: 07/03/2022

ACKNOWLEDGEMENTS

At first I would like to express my sincere gratitude to my supervisors Prof. Mario Einax and Prof. Cosmas Muiva for the support and guidance they provided throughout my study. I am really thankful of the guidance you gave me during the struggle and when I wanted to give up, I made it because your guidance and support. I would also love to thank other members of academic staff in the department of Physics and Astronomy for the remarks they made during presentation of this work, those remarks helped me a lot in improving this work.

I would also like to appreciate the support and courage I got from my colleagues (Dineo Sebuso, Keadiretse Lefatshe, Tlotlo Setlhare, Thuso Gaosenngwe, Ndakizilo Nthoiwa and Romang Bosigo). I nearly gave up but the support and courage you gave me lead to these fruitful results.

I am also thankful to all technicians in BIUST and other institutions for helping me with sample preparation, acquisition of data and analysis.

Finally, yet important I would like to thank my mother (Grace Difemo) and my siblings (Sonkie Kefositse, Thabane Difemo, Tirelo Difemo and Mosimanegape Kefositse) for the support and love they showed me during my entire study. I am grateful of the motivation you gave me every day to finish this thesis.

DEDICATION

This work is devoted to my parents, thank you for your long-lasting support.

TABLE OF CONTENTS

DECLARATION REGARDING THE WORK AND COPYRIGHT	i
CERTIFICATION.....	ii
ACKNOWLEDGEMENTS.....	iii
DEDICATION	iv
TABLE OF CONTENTS.....	v
LIST OF TABLES.....	viii
LIST OF FIGURES.....	ix
LIST OF ABBREVIATIONS AND SYMBOLS.....	xii
ABSTRACT.....	xiv
CHAPTER 1 : INTRODUCTION	1
1.1 Statement of the problem	3
1.2 Aims and objectives	4
1.3 Significance of study	4
1.4 Outline of the thesis.....	5
CHAPTER 2 : THEORY AND BACKGROUND INFORMATION	6
2.1 The photovoltaic effect.....	6
2.2 A p-n junction.....	6
2.3 How does a photovoltaic cell work?	7
2.4 Types of recombination mechanisms occurring across a p-n junction.....	8
2.4.1 Auger recombination	8
2.4.2 Shockley-Read-Hall recombination.....	9
2.5 Modelling a photovoltaic cell and characteristic parameters	10
2.5.1 Model of an ideal photovoltaic cell	10
2.5.2 Model of a real photovoltaic cell (Single diode model)	11
2.5.3 Open-Circuit voltage	13
2.5.4 Short-Circuit Current (I_{sc}).....	13
2.5.5 Fill Factor (FF).....	13
2.5.6 Efficiency (η).....	14
2.6 Current trends in photovoltaic technology.....	15
2.7 Crystal structure of a Cu_2ZnSnS_4 (CZTS) compound	18
2.7.1 Observable secondary phases in CZTS structure	19

2.8 Electrical and optical properties of a CZTS absorber	20
2.9 Design of CZTS solar cells	21
2.10 Background Information of kesterites solar cells	21
2.11 Methods of growing CZTS thin films	24
2.11.1 Thermal evaporation.....	25
2.11.2 Sputtering.....	26
2.11.3 Sol gel.....	27
2.11.4 Spray pyrolysis	29
CHAPTER 3 : MATERIALS AND METHODS	31
3.1 Arrangement of a spray machine	31
3.2 Cleaning the substrates.....	31
3.3 Depositing the CZTS thin films	32
3.4 Synthesizing In_2S_3 thin films	33
3.5 Fabricating FTO/CZTS/Ag and FTO/ In_2S_3 /CZTS/Ag solar cells	34
3.6 Deposition of Ag electrodes.....	35
3.7 Characterizing the CZTS and In_2S_3 layers	36
3.7.1 X-Ray Diffraction	36
3.7.2 Raman Spectroscopy.....	38
3.7.3 Stylus Profiler	40
3.7.4 UV-Vis Spectroscopy	41
3.7.5 Hall Measurement	43
3.7.6 Scanning Electron Microscopy	44
3.7.7 Atomic Force Microscopy (AFM).....	46
3.8 Studying the performance of the cell	48
CHAPTER 4 RESULTS AND DISCUSSION.....	52
4.1 Characterisation of CZTS thin films.....	52
4.1.1 Structural Characterization of CZTS thin films	52
4.1.2 Thickness measurements.....	55
4.1.3 Optical studies of CZTS samples.....	56
4.1.4 Electrical properties	60
4.1.5 Morphology.....	61
4.1.6 Elemental composition	63
4.2 Characterisation of In_2S_3 thin films	65
4.2.1 Structural properties.....	65

4.2.2 Measurement of thickness	67
4.2.3 Optical measurements.....	68
4.2.4 Electrical properties	70
4.2.5 Atomic Force Microscopy results.....	72
4.3 PERFORMANCE OF THE CELLS.....	73
4.3.1 The photo-conductivity of CZTS thin films.....	73
4.3.2 The I-V characteristics of the CZTS solar cells.....	74
CHAPTER 5 CONCLUSION AND RECOMMENDATIONS.....	78
5.1 Conclusion.....	78
5.2 Recommendations.....	79
REFERENCES.....	80

LIST OF TABLES

Table 1: Highest efficiencies obtained through various solar cells configurations[59].....	16
Table 2: Pair of zinc and tin sources used for preparation of four CZTS samples.....	33
Table 3: Values of crystallite sizes, dislocation densities and lattice parameters for CZTS samples.....	54
Table 4: Thickness of the CZTS thin films.....	55
Table 5: The electrical parameters of the CZTS samples prepared from different precursor solutions	61
Table 6: Elemental composition of the CZTS thin films.....	65
Table 7: Values of crystallite sizes and dislocation densities of In ₂ S ₃ thin films.....	66
Table 8: The bulk concentration, resistivity, mobility and average hall coefficient of In ₂ S ₃ thin films.....	71
Table 9: Roughness of In ₂ S ₃ thin films.....	73
Table 10: The photovoltaic parameters of Cell – A and Cell – B	77

LIST OF FIGURES

Figure 1: Consumption of solar energy in United States of America between 1989 and 2016 [12].	2
Figure 2: A typical structure of a p-type semiconductor material, n-type semiconductor material and p-n junction [30].	7
Figure 3: Typical design of a photovoltaic cell [31].	8
Figure 4: Schematic diagrams for various auger recombination process (a) direct intra-band, (b) indirect intra-band, (c) direct inter-band and (d) indirect interband [35].	9
Figure 5: Shockley-Read-Hall mechanism [36].	9
Figure 6: Equivalent circuit of (a) an ideal and (b) a practical PV cell [37].	10
Figure 7: The current-voltage (I-V) and power-voltage (P-V) curves of a PV cell [40].	12
Figure 8: Efficiency of the solar cells as function of their energy gaps [50].	15
Figure 9: Trend in photovoltaic technology since 1960 [58].	16
Figure 10: The global market share of various solar cells in 2010 [63].	17
Figure 11: The abundance of elements in atoms of element per 10^6 atoms of Si.	18
Figure 12: A unit cell of a kesterite CZTS (left) and stannite CZTS (right) [72].	19
Figure 13: Equilibrium phase diagram for the $\text{Cu}_2\text{S-ZnS-SnS}_2$ [74].	19
Figure 14: Typical XRD diffractographs of CZTS layers prepared at different temperatures [75].	20
Figure 15: A typical architecture of a CZTS solar cell [82].	21
Figure 16: I-V characteristics and EQE of the CZTS/ZnSnO cells [86].	22
Figure 17: Current -Voltage curves of a cell fabricated with absorber under stoichiometric conditions and a cell obtained by reducing Cu and increasing amount of Zn [90].	23
Figure 18: Current - Voltage curves of Na and Sb doped cell and the complete cell [92].	23
Figure 19: Current -Voltage characteristics of FTO/CZTSSe and ITO/CZTSSe solar cells under bifacial, front, rear and dark illumination [94].	24
Figure 20: Typical representation of (a) resistive heating and (b) inductive heating [99].	25
Figure 21: A simplified description for a sputtering system [103].	27
Figure 22: Steps involved in sol-gel method and some possible products obtained from sol-gel technique [108].	28
Figure 23: Typical Set-up for spray pyrolysis [115].	30
Figure 24: Experimental set-up for spray pyrolysis.	31

Figure 25: The glass substrates in (a) acetone and (b) ethanol.	32
Figure 26: The (a) architecture of the FTO/In ₂ S ₃ /CZTS/Ag solar cells and (b) FTO/In ₂ S ₃ /CZTS/Ag.	35
Figure 27: TF 500 machine.	36
Figure 28: Bruker D8 Advance diffractometer.	37
Figure 29: Bragg's scattering [119].	38
Figure 30: The LabRAM HR Evolution Raman spectrometer.	40
Figure 31: KLA Tencor D-100 profiler.	41
Figure 32: The Perkin Elmer 750 UV/VIS/NIR spectrometer.	43
Figure 33: ECOPIA HMS5500 Hall measurement system.	44
Figure 34: The MERLIN ZEISS GEMINI SEM.	46
Figure 35: Basic components of atomic force microscopy[124].	47
Figure 36: The BRUKER Atomic Force Microscope.	48
Figure 37: The SciSun-150 solar simulator.	49
Figure 38: The spectral Match obtained from SciSun-150 solar simulator[125].	49
Figure 39: (a) The Keithley 4200A-SCS parameter analyzer and (b) schematic connection of the solar cell to one SMU and GNDU)[126].	50
Figure 40: A circuit for finding the I-V curve of a cell.	51
Figure 41: X-Ray diffraction patterns of the CZTS samples.	53
Figure 42: Raman spectra of the CZTS thin films.	55
Figure 43: (a) Absorbance and (b) Reflectance of the CZTS thin films.	57
Figure 44: Absorption coefficient (α) for the CZTS thin films.	59
Figure 45: Tauc's plots for the CZTS samples prepared from solutions containing (a) SnCl ₂ and (b) SnCl ₄	60
Figure 46: SEM images of (a) CZTS001, (b) CZTS002, (c) CZTS003, and (d) CZTS004 thin films.	62
Figure 47: The EDX spectra of (a) CZTS001, (b) CZTS002, (c) CZTS003 and (d) CZTS004.	64
Figure 48: XRD spectra of In ₂ S ₃ thin films.	66
Figure 49: Raman spectra of In ₂ S ₃ thin films.	67
Figure 50: Thickness of In ₂ S ₃ thin films prepared at various concentrations of thiourea.	68
Figure 51: Transmittance spectra of spray deposited and annealed In ₂ S ₃ thin films.	69

Figure 52: Optical band gaps of In_2S_3 thin films obtained by varying thiourea concentration.	70
Figure 53: Conductivity of In_2S_3 thin films as a function of thiourea concentration.	72
Figure 54: AFM micrographs of (a) $\text{In}_2\text{S}_3_{0.090}$, (b) $\text{In}_2\text{S}_3_{0.095}$, (c) $\text{In}_2\text{S}_3_{0.100}$ and (d) $\text{In}_2\text{S}_3_{0.105}$ thin films.	73
Figure 55: I-V curves of the samples CZTS001 and CZTS003 measured in the dark and under illumination.	74
Figure 56: The (a) dark, (b) illuminated I – V characteristics and (c) P – V curves for cell-A and cell-B.	76

LIST OF ABBREVIATIONS AND SYMBOLS

A – Absorbance

Å – Angstroms

AFM – Atomic Force Microscope

at.% - Atomic percentage

CZTS – copper zinc tin sulfide

D – Grain size

EDS – Energy dispersive Spectroscopy

E_g – optical band gap

eV – Electron volts

FTO – Fluorine doped tin oxide

FWHM - Full width at half maximum

\hbar – Plank's constant

I – current

ITO – Indium tin oxide

R – Reflectance

R_s – Sheet resistance

SEM – Scanning electron microscope

t – Thickness

TCO – Transparent conducting oxides

XRD – X-ray diffraction

α – Absorption coefficient

β – Full width at half maximum

θ – Bragg's angle

λ – Wavelength

π – Pi

ρ – Resistivity

Ω - Ohm

Ω cm – Ohm centimetre

ABSTRACT

Photovoltaic technology is a very crucial technology and it is gradually growing worldwide as there is plenty of sunshine daily especially in African countries. The aim of photovoltaic technology is to generate electricity from solar power using photovoltaic devices like solar (photovoltaic) cells. Photovoltaic cells are mostly used to provide electricity in rural areas which are not connected to the national grid like farms (cattle posts). In this work superstrate CZTS solar cells (Cell-A and Cell-B) were fabricated from optimised CZTS absorber layers and In_2S_3 buffer layer by a cost-effective spray pyrolysis technique. Firstly, CZTS absorber layers were grown on borosilicate glass substrates from various precursor solutions and their properties were studied through X-ray diffraction, Raman spectroscopy, UV-Vis spectroscopic analysis, Hall measurement, and Scanning electron microscopy. X-ray diffraction results revealed similar patterns for all samples that are three peaks: (1 1 2), (2 2 0), and (2 1 2) belonging to kesterite CZTS with tetragonal structure. All thin films were growing along (1 1 2) plane. Results obtained via Raman spectroscopy revealed two wide peaks at 248 cm^{-1} and 331 cm^{-1} in all thin films. Both peaks belonging to CZTS with tetragonal structure. Both the X-ray diffraction and the Raman spectrometry results revealed that samples prepared from solutions containing tin (IV) chloride were highly crystalline. The maximum absorbance obtained for all thin films was between 1.5 and 4 in the visible and near infrared region. Unlike crystallinity, the absorbance was high for samples that were prepared from solutions containing tin (II) chloride as a tin source. As revealed by the Hall measurement, the resistivity of the thin films was ranging from $2.84 \times 10^{-2}\ \Omega\text{cm}$ to $3.29 \times 10^{-1}\ \Omega\text{cm}$ and the sample with the lowest resistivity (labelled as CZTS003) was prepared from a solution containing copper (II) chloride, zinc acetate, tin (IV) chloride and thiourea solutions. The SEM micrographs showed well defined grains for all thin films except the one that was prepared from a solution containing copper (II) chloride, zinc nitrate, tin (IV) chloride and thiourea. A sample that had the lowest resistivity also exhibited the largest grains.

In the second part of this work, In_2S_3 buffer layers were also deposited on glass substrates from a mixture of indium chloride solution and thiourea solution. The concentration of indium chloride solution was held constant and the concentration of thiourea was varied between 0.090 M and 0.105 M in steps of 0.005 M. After deposition, the thin films were characterised via X-ray diffraction, Raman spectrometry, UV-Vis spectroscopy, Atomic Force Microscopy, and Hall measurement. The results obtained by X-ray diffraction revealed

polycrystalline β - In_2S_3 , and the increased concentration of thiourea lead to decreased crystallinity of the thin films. Similar Raman spectra of all thin films was obtained via Raman spectroscopy. The two peaks found at 306 cm^{-1} and 365 cm^{-1} on the Raman spectra belong to β - In_2S_3 . All the thin films exhibited similar transmittance spectra, and the transmittance of the thin films was lying between 60 % and 80 % in the visible and near infrared region of the electromagnetic spectrum. Transmittance was highest in the visible region for the sample prepared from solution containing 0.095 M of thiourea solution. In addition, the thin films had wide optical band gaps lying between 2.75 eV and 3.0 eV. The electrical resistivity of In_2S_3 thin-film layers increased from $5.6249 \times 10^{-2}\ \Omega\text{cm}$ to $4.0953\ \Omega\text{cm}$ when concentration of thiourea solution was increased from 0.090 M to 0.100 M, however, when the concentration was further increased to 0.105 M the resistivity of the In_2S_3 thin film layers decreased.

The performance of fabricated solar cells (denoted as Cell-A prototype and Cell-B prototype) was studied. Cell-A prototype performed better than Cell-B prototype, because the efficiency at maximum power point of Cell-A was 0.158 % while the efficiency at the maximum power point of Cell-B was 0.07 %. In addition, Cell-A exhibited higher open-circuit voltage and short-circuit current density compared to Cell-B. The open-circuit voltage and short-circuit current density of Cell-A were 200 mV and 2.26 mA/cm^2 , respectively, while Cell-B had shown open-circuit voltage of 80mV and short-circuit current density of 1.75 mA/cm^2 .

CHAPTER 1 : INTRODUCTION

Energy is very crucial in our daily lives. Various activities that human beings carry out every day, such as cooking, lighting, heating water or mobile communication, need energy [1],[2]. Among different forms of energy, electrical energy is the most flexible form of energy. It can be easily transformed to other forms of energy. Electrical energy can be produced from both renewable (solar, wind) and non-renewable (coal, natural gas, oil) sources, however, non-renewable sources (coal, natural gas, oil) have a higher input towards the amount of electricity required to power the whole world. Recently the demand of electricity in the world for a single year was higher than 10^{12} kWh. About three quarters of this value is produced from non-renewable sources and the remainder is generated from renewable sources [3]. Despite the fact that renewable energy sources had contributed less towards power generation in recent years, it still remain a glimpse of hope that can help everyone in the world to survive the climatic changes in future. In developing countries, particularly in Africa, the access of renewable energy is still a problem and people who need the help of renewable energy are those who stay in remote areas like cattle posts or villages which are not connected to the grid. The building of new technology based on renewable sources in Africa is affected by several factors including: lack of education and training, poor economies and inconsistent energy regulations [4].

At the current stage, most African countries depend on non-renewable sources. They mainly utilize fossil fuels for energy, however, their use in power generation can lead to serious environmental problems. For example, the burning of fossil fuels generates greenhouse gases like carbon dioxide (CO_2) gas that is released into the atmosphere. The increasing level of CO_2 gas in the atmosphere leads to warming of global temperatures and unstable climate [5]. Due to the negative effects of using fossil fuels on the environment, the clean and safer renewable sources such as solar, wind or biomass are recently gaining attention. Among all these sources, solar energy is the most promising [6]. Solar energy is one of the most plentiful source of energy in the world, the average intensity of solar radiation emitted by the sun onto earth on a clear day is approximately 1000 W/m^2 [7]. The use of solar power is growing nowadays and the manufacturing cost has also reduced significantly. Photovoltaic devices like solar panels are now used in many households and industries. Figure 1 shows that consumption of electricity generated from solar energy in United States of America between

1989 and 2016, which has been drastically increasing from 2010 to 2016. However, in Africa, generation of electricity from renewable energy sources (like solar energy) is still one of the major challenges. The fact that African countries receive the highest amount of solar radiation on earth is a great advantage to solve this challenge. For instance Botswana receives an average solar radiation of 21 MJm^{-2} per day [8]. This amount is very high and favourable for power generation from solar energy. Now it is time for Africa to take the opportunity of photovoltaics by developing more sustainable industries and research activities at universities that can specialize in solar.

In particular, various technologies like concentrating solar power (CSP) systems, solar heating/cooling and solar photovoltaics (PV) can be used to capture energy from the sun and transform it into electricity. In CSP systems the solar concentrators are used to concentrate solar radiation from the environment to the receiver where it will be transformed into heat. The generated heat can be used to operate the turbines and produce power [9],[10]. Frontier research focuses on the conversion of solar radiation into electrical energy by the use of a clean and safe PV technology. Photovoltaic devices, such as solar cells, are used to capture radiation coming from the sun and transform the solar energy into electrical energy. This energy conversion process follows a principle denoted as photovoltaic effect [11].

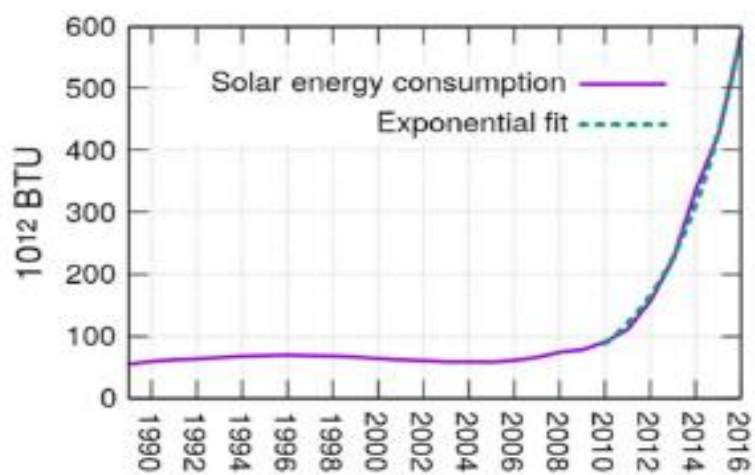


Figure 1: Consumption of solar energy in United States of America between 1989 and 2016 [12].

1.1 Statement of the problem

Several categories of solar cells had been developed and used in the past few decades. The first category is based on silicon (silicon wafer, mono-crystalline silicon and polycrystalline silicon) while the second category refers to thin films (amorphous silicon, CdTe, CuInSe, CuInGaSe₂, etc.). Currently polycrystalline solar cells are mass produced and dominating the solar market worldwide. However, thin films solar cells are expected to replace slowly the polycrystalline cells and dominate the market in the coming years, because materials needed to fabricate these cells become cheaper together with the reduction of production cost per kilowatt-hour (kWh). Amongst thin film solar cells, only the cells made up of CdTe, CuInGaSe₂ (CIGS) and thin film silicon absorbers are commercialized with thin film silicon highly produced at the current stage. The CdTe and CuInGaSe₂ have a record efficiency of 19 % and 20.3 % respectively [13],[14].

However, the toxicity of some elements such as cadmium (Cd) and selenium (Se) raises a lot of hazards about the CdTe and CuInGaSe₂ (CIGS) solar cells. In addition, the shortage of indium (In) tellurium (Te) and gallium (Ga) pose some other problems about these solar cells [15]. These disadvantages were taken care of by developing a low price, stable and environmentally friendly Cu₂ZnSnS₄ (CZTS) absorber [16]. The rare elements indium and gallium were replaced by abundant elements zinc (Zn) and tin (Sn) [17]. The CZTS solar cells have lower efficiency compared to their counterparts (CIGS). A very high open circuit voltage (V_{OC}) deficit obtained from the CZTS solar cells might be one of the factors contributing to lower efficiency of these solar cells [18]. This might be caused by an observed cliff like conduction band offset at the boundary between the absorber (CZTS) and buffer (CdS) [19]. Moreover detrimental phases such as Cu_xS, ZnSnS, ZnS, CuSnS₃ and others that can be found in the light absorber, in addition to the kesterite CZTS structure, may also degrade the performance of the cells as they increase recombination rate [20],[21]. Nevertheless, there is still a lot of improvements that can be implemented to enhance the performance of the CZTS solar cells, especially when looking at the low-cost fabrication methods like spray pyrolysis. In this project a CZTS solar cell were fabricated based on an eco-friendly In₂S₃ buffer layer. At room temperature In₂S₃ buffer layer has small optical band gap (about 2.1 eV)[22], however, wide optical band gaps (2.75 eV and 3.25 eV)[23] have been achieved from In₂S₃ layers grown by chemical bath deposition and atomic layer deposition, respectively. The wide band gaps achieved from In₂S₃ thin films makes them to be suitable buffer layers that can replace CdS layer.

1.2 Aims and objectives

The intention of this project is to fabricate a solar cell prototype based on the abundant and eco-friendly CZTS absorber. This will be achieved through the following objectives:

- Synthesis of the CZTS and In_2S_3 thin films through a simple and cost effective a spray pyrolysis method under different conditions.
- Analysis of the structural, optical, morphological and electrical properties of both CZTS and In_2S_3 thin films. The CZTS layers that exhibit good properties will be used for fabricating photovoltaic cell prototypes.
- Building two photovoltaic cell prototypes with the structure FTO/CZTS/ In_2S_3 /Ag based on two CZTS thin films and one In_2S_3 thin film with good properties. Silver (Ag) contacts will be deposited on the CZTS and FTO layers through Radio frequency magnetron sputtering.
- Evaluating the performance of the produced solar cells under standard test conditions by using a solar simulator. Measurement of key parameters of the cells namely short circuit current, open circuit voltage and efficiency will be performed.

1.3 Significance of study

Photovoltaic technology is becoming a prominent field these days. Unlike other conventional technologies, photovoltaic technology has interesting environmental advantages as it helps to reduce the emission of hazardous gases (sulfur dioxide, carbon monoxide and carbon dioxide) into the atmosphere. As stated before in photovoltaic technology solar cells are used in the process of energy conversion, however, there some problems associated with various manufacturing processes and materials involved while fabricating these cells. But at the end the low-cost photovoltaic devices that do not cause a lot of pollution to the surrounding have to be built. In this project the efficiency of the eco-friendly and low-cost CZTS thin film solar cells were studied based on spray pyrolysis technique. A focus was on how different precursor solutions can help to improve the cell efficiency. The prototype products of this project can be used in future to provide power especially in rural and remote areas. The output of this research will also help researchers to find possible ways of improving the performance of new absorber and window layer materials based on the low-cost spray pyrolysis technique. Moreover, a CZTS layer can also be used as counter electrode in dye sensitized solar cell (DSSC) concepts to replace the environmental unfriendly Pt counter electrode.

1.4 Outline of the thesis

The content of this thesis is written in five separate chapters. And the chapters are as follows: Introduction, Theory and Background information, Methodology, Results and Discussion, Conclusion.

Chapter 1: Introduction

In this Chapter the importance of energy is mentioned. The generation of electrical energy from renewable and non-renewable sources was described. The challenges of renewable sources and advantages of using renewable sources (especially solar energy) in power generation are outlined. Furthermore, the ways of capturing solar energy (concentrated solar power systems and solar photovoltaics) are described and a few examples of solar cells are stated.

Chapter 2: Theory and Background information

This Chapter focus more on the origin and current status of photovoltaic technology and a brief description of photovoltaic effect and p-n junction is given. The kesterite (CZTS and CZTSe) solar cells are the main focus in this chapter. Therefore, the origin, structure and performance of kesterite solar cells are discussed, moreover the problems leading to poor performance of the CZTS solar cells are stated. In addition, the structural, electrical and optical properties of the CZTS absorber layer are described. Lastly the in-depth descriptions on vacuum and non-vacuum-based methods that were previously employed to deposit CZTS absorber layer are given.

Chapter 3: Methodology

In this chapter, a detailed description on the preparation of the CZTS absorber layer, In_2S_3 buffer layer and FTO/CZTS/ In_2S_3 /Ag solar cell is given. The methods of characterizing the obtained products are also described in details.

Chapter 4: Results and Discussion

Here, the results obtained from various instruments, thorough analysis and full discussion of results are given.

Chapter 5: Conclusion

In the last chapter a summary of results and important tasks that can be carried out in future to improve the current work are presented.

CHAPTER 2 : THEORY AND BACKGROUND INFORMATION

2.1 The photovoltaic effect

When semiconductor materials absorb photons, electron-hole pairs are generated and an electric field builds within a semiconductor. This process is called the photovoltaic effect and was discovered in 1839 by Edmund Becquerel [24]. The Photovoltaic effect can be easily detected on photosensitive semiconducting materials with very high absorption coefficient. After the discovery of the photovoltaic effect most researchers came up with different technologies for generating electricity from solar energy. Selenium was the first material studied around 1870, however, the obtained efficiency was very low (1% to 2%). Later in 1954 a 4 % solar cell was fabricated using a crystalline silicon at the Bell Labs. After some further improvements an efficiency of 11 % was achieved and this led to the development of the first generation of solar cells [25].

2.2 A p-n junction

To understand diodes and solar cells it is very essential to understand how a p-n junction is formed and the mechanisms taking place in a p-n junction. Electrical and optical properties of semiconductors can be improved by doping. Doping is a process in which impurities are introduced to semiconductors leaving behind an extra electron or hole in the structure of the semiconductor [26]. A semiconductor with more electrons than holes is referred to as n-type, while the one with more holes than electrons is p-type. A p-n junction is formed by assembling a p-type semiconductor material with an n-type semiconductor material [27].

Now it would be very interesting to understand the motion of electrons and holes in a p-n junction. The electrons in the n-region (free electrons) are free to move randomly so those closer to the interface of the junction will cross the junction to p-region and combine with the holes, as electrons and holes combine, the p region loses some of the holes. As a result of this motion, a layer of positive charges and a layer of negative charges build along the interface of the junction in the n-region and p-region respectively [28]. These layers of charges form an electric field (the so-called built-in electric field). This built-in electric field now opposes the motion of charges caused by diffusion [29]. Eventually the flow (diffusion) of electrons across the junction will be stopped by the electric field and external energy will be required to

move an electron across the junction. Figure 2 shows the configuration of a p-type material, n-type material and p-n junction.

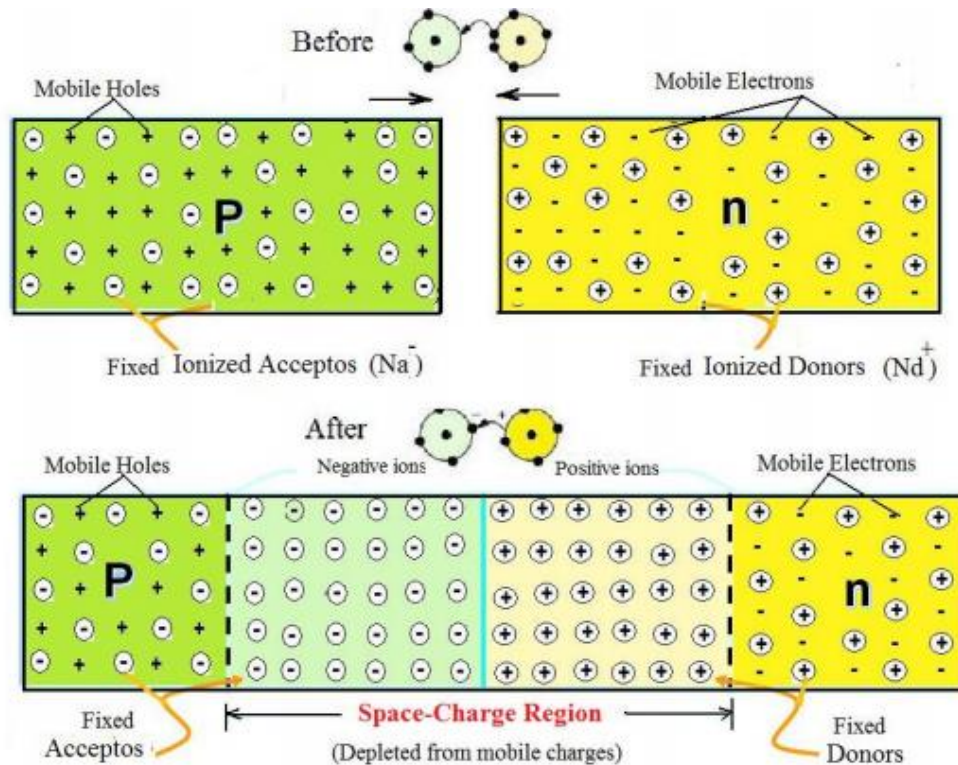


Figure 2: A typical structure of a p-type semiconductor material, n-type semiconductor material and p-n junction [30].

This concept of a p-n junction is applied in many photovoltaic devices such as solar cells to generate and separate the charges. For an electrical current to be produced in solar cells, charges need to be separated and electrons and holes must flow towards positive and negative contacts. The gradients of Fermi energies are the ones that give rise to this flow.

2.3 How does a photovoltaic cell work?

A photovoltaic cell (also known as a solar cell) is a device that generates electrical energy directly from solar power. It is made up of p-type (usually the absorber) and n-type (usually a window/buffer layer) semiconductor materials. When sunlight shines over the surface of a photovoltaic cell, electron-hole pairs are generated and separated by a p-n junction. This phenomenon leads to current flow in the cell and induces voltage across the contacts (front and back) of a solar cell. A typical design of a photovoltaic cell is shown in Figure 3.

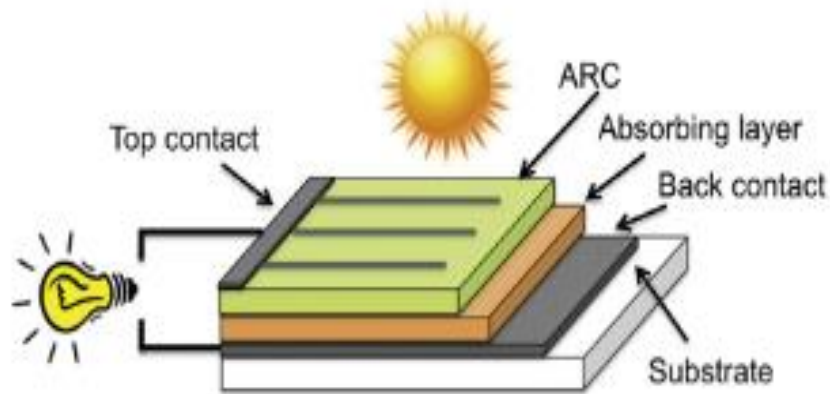


Figure 3: Typical design of a photovoltaic cell [31].

2.4 Types of recombination mechanisms occurring across a p-n junction

In section 2.3 it was clearly discussed how electrons and holes are generated across a p-n junction, however, this process can be reversed through a process called recombination. Recombination is a mechanism whereby an electron reacts with a hole to produce energy, photons or phonons. There are two major types of recombination processes being radiative and non-radiative recombination. In radiative recombination only photons are produced while in non-radiative recombination the energy produced is absorbed by other particles such as phonons, electrons and holes. Furthermore, non-radiative recombination is divided into three forms, namely, auger recombination, surface recombination, and Shockley-Read-Hall recombination [32],[33]. The Shockley-Read-Hall is the main mechanism that occurs in practical solar cells.

2.4.1 Auger recombination

Auger recombination requires three different charge carriers. When the two charge carriers (an electron and hole) recombine, energy is released and this energy is given to a third charge carrier (either an electron or a hole). Energy gained by a third charge carrier leads to the excitation of the third charge carrier. The third charge carrier moves to higher level within the conduction band, if it is an electron or be pushed down to the valence band, if it is a hole. Figure 4 presents the four schematic diagrams of auger recombination processes in a case where the third charge carrier is an electron. Auger recombination strongly depends on the

band gap of a semiconductor. It occurs at a higher rate in semiconductors with small optical band gaps and its rate decreases with increasing optical band gap [34].

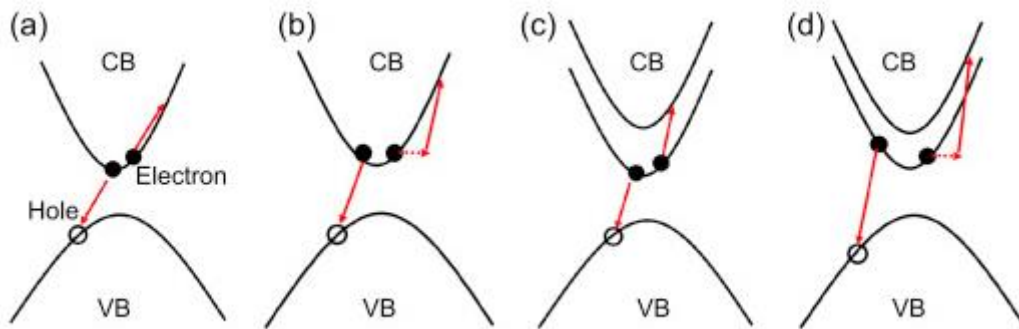


Figure 4: Schematic diagrams for various Auger recombination process (a) direct intra-band, (b) indirect intra-band, (c) direct inter-band and (d) indirect interband [35].

2.4.2 Shockley-Read-Hall recombination

As shown in Figure 5 there are some impurities that exist in the centre of a forbidden zone. These impurities play a pivotal role by capturing excited electrons and holes. Let us consider a homogeneously charged semiconductor under open circuit condition. As the semiconductor absorbs photons, the concentration of electrons at the conduction band increases, because electrons are generated at a rate G , which is equal to the generation rate of holes in the valence band. However, some electrons are trapped by the impurity states, which are found in between the valence band and conduction band. As a consequence, this changes the concentration of electrons in the conduction band by a capture rate $R_{e,imp}$. The electrons trapped by the impurities can also be ejected from such impurities back to the conduction band at an emission rate $G_{e,imp}$. Similarly the concentration of holes in the valence band is affected by the generation rate (G), capture rate ($R_{h,imp}$) and emission rate ($G_{h,imp}$). This phenomenon is called Shockley-Read-Hall recombination [31].

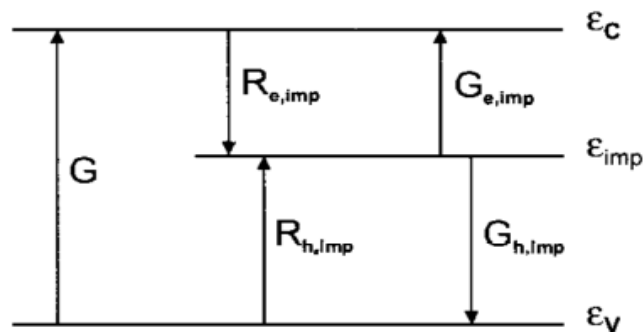


Figure 5: Shockley-Read-Hall mechanism [36].

2.5 Modelling a photovoltaic cell and characteristic parameters

A photovoltaic cell can be modelled from an ideal point of view. To achieve the most accurate results compared to that of practical cell, the ideal model can be improved by including other important parameters (like resistors and diodes that represent losses and recombination) that real PV cells exhibit. The equivalent circuits of an ideal and a practical PV cell are shown in a Figure 6.

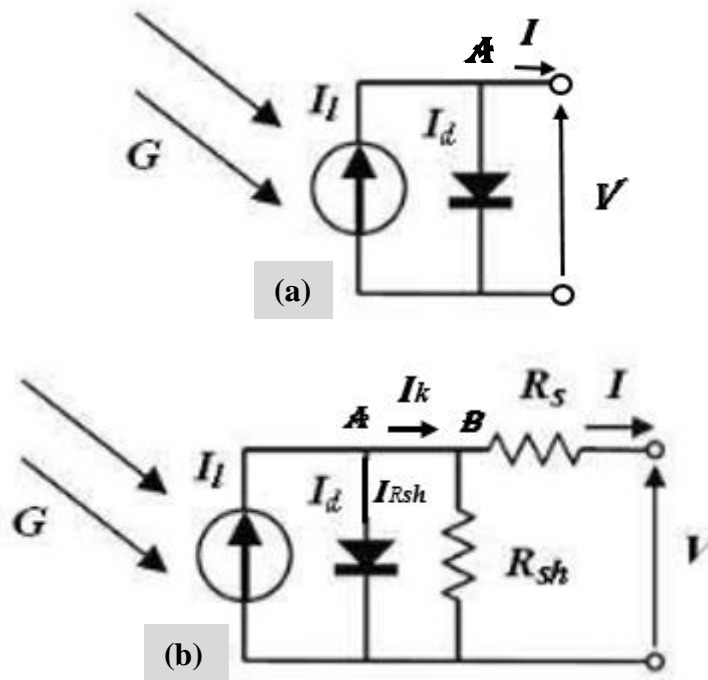


Figure 6: Equivalent circuit of (a) an ideal and (b) a practical PV cell [37].

2.5.1 Model of an ideal photovoltaic cell

As shown in Figure 6, a PV cell is like a current source under illumination and diode in the dark, respectively. This is the starting point to formulate an ideal model of PV cell in order to describe the current-voltage characteristic. To derive the I-V characteristic the Kirchhoff's junction rule is applied at junction A in Figure 6 (a), which represents the ideal PV cell. At junction A:

$$I_l = I_d + I, \quad (1)$$

where I_l is the current under illumination, while I_d is the dark current. A simple rewriting of (1) leads to

$$I = I_l - I_d \quad (2)$$

The current passing through a diode in dark (I_d) is given by the Shockley diode equation[38]:

$$I_d = I_0 \left[\exp\left(\frac{qV}{nkT}\right) - 1 \right] \quad (3)$$

Based on Eqs. (2) and (3), we are able to determine the I-V characteristic of an ideal PV cell. The parameters I_0 , q , V , n , k and T in (3) are the reverse saturation current of a diode, charge of an electron, voltage across the diode, diode ideality, Boltzmann's constant, and temperature, respectively. When a p-n junction is connected in reverse bias mode some of the current carriers start leaking across it. The measure of such leakage is known as a reverse saturation current. The value of an ideality factor n helps to identify the type of recombination that lowers the cell performance and its location within the cell[39]. For an ideal diode there are no defects and the current flowing across the junction is due to diffusion only, i.e., the n is equal to one. But when deficiencies increase recombination also climbs. Thus, the value of n can rise up to two.

Hence inserting (3) into (2) leads the current – voltage (I-V) characteristic of an ideal photovoltaic cell:

$$I = I_l - I_0 \left[\exp\left(\frac{qV}{nkT}\right) - 1 \right] \quad (4)$$

2.5.2 Model of a real photovoltaic cell (Single diode model)

In practical solar cells there are some losses that takes place within in a cell. Such losses can be compensated by including series and parallel resistors to the equivalent circuit as shown in Figure 6 (b). Series and parallel resistors represent the total resistance that takes place at the surface of a cell and losses caused current leaking at the p-n junction, respectively. Series resistance lowers the value of a fill factor and in an ideal PV cell its value is equivalent to zero. The approximate value of series resistance can be found by computing the gradient of an I-V curve near the open circuit voltage point. To compensate for recombination another diode can be added to a single diode model, however, in this section we restrict our discussion to an I-V characteristic for a single diode model. Kirchhoff's junction and loop rules are also used here to come up with I-V characteristic of a real cell. Looking at Figure 6 (b), applying Kirchhoff's junction rule at junction A leads to:

$$I_l = I_d + I_k, \quad (5)$$

and at junction B we obtain:

$$I_k = I + I_{Rsh}. \quad (6)$$

The current I , produced by PV cell, can be found by inserting (6) into (5), which leads to the relation:

$$I = I_l - I_d - I_{Rsh} \quad (7)$$

By applying the Kirchoff's loop rule to a loop on the right that consists of R_{sh} and R_s gives the following equation:

$$I_{Rsh} = \frac{V + IR_s}{R_{sh}}. \quad (8)$$

Therefore inserting (3) and (8) into (7) lead to the I-V characteristic of a practical cell:

$$I = I_l - I_0 \left[\exp\left(\frac{q(V + IR_s)}{nkT}\right) - 1 \right] - \frac{V + IR_s}{R_{sh}} \quad (9)$$

In the above equation, there is an extra voltage term (IR_s) due the series resistance and it influences the total voltage across the diode. When this term is included the voltage across the diode becomes $V + IR_s$. Figure 7 shows two plots of I versus V and P versus V from which four main parameters of a photovoltaic cell (open circuit voltage (V_{oc}), short circuit current (I_{sc}), fill factor (FF), and maximum power point (P_{mp})) can be obtained. A fill factor is defined as a fraction between a red rectangle and blue rectangle.

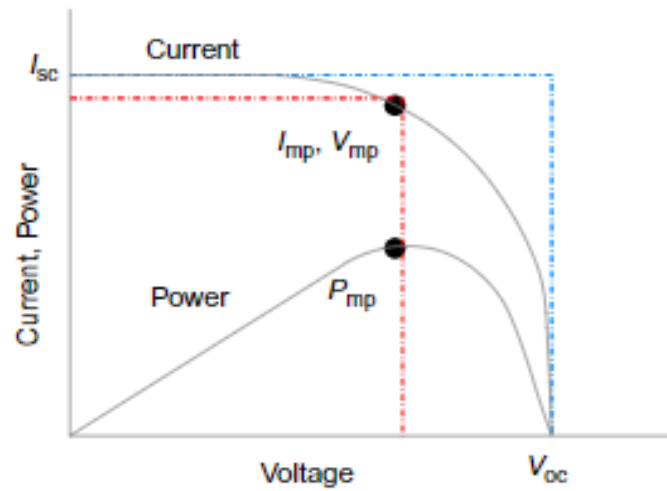


Figure 7: The current-voltage (I-V) and power-voltage (P-V) curves of a PV cell [40].

2.5.3 Open-Circuit voltage

Open-circuit voltage (V_{OC}) is the parameter of great significance when working with a photovoltaic cell. It refers to the maximum voltage that can be obtained across the contacts of a cell under open circuit conditions. That is when there is no current passing through a cell. The V_{OC} depends on the various factors such as photo-generated current and optical band gap of the absorber materials. V_{OC} obtained from a cell made of a particular material will be always be smaller compared to the optical band gap of that material. Under open circuit conditions the shunt resistance is assumed to be very high, so the third term on I-V characteristic equation (9) becomes very small and can be neglected. Thus, by setting $I = 0$, a rewriting of equation (9) gives:

$$V_{OC} = \frac{nkT}{q} \ln\left(\frac{I_l}{I_0} - 1\right) \quad (10)$$

According to the above equation V_{OC} and I_0 are “inversely” related, the highest value of V_{OC} can be obtained if I_0 is at the lowest point. The value of I_0 is mainly influenced by the recombination mechanism occurring within a cell [41].

2.5.4 Short-Circuit Current (I_{SC})

Another vital parameter of solar cell is the short-circuit current. It is the most possible current that can be measured when the potential difference across the contacts of a cell is zero. This parameter is influenced by the amount of photons incident upon the surface area of a cell. In most cases short circuit current density (I_{SC}) is used to explain the highest possible current that a cell can produce per cm^2 . I_{SC} depends on the optical parameters of the absorber material, such as band gap and absorption coefficient. To understand how does band gap affects the value of I_{SC} , we consider two absorber materials one with a small band gap and the other with a large band gap under light. The one with a small band gap will suck up more photons than the one with a wide band gap. Therefore, it can be concluded that the short circuit current is inversely related to the band gap of the absorber material [42].

2.5.5 Fill Factor (FF)

A fill factor is also a useful parameter to characterize photovoltaic cells. It is defined as the highest amount of electrical power that can be scooped out from a photovoltaic cell. The

equation (11)[43] that follows can be used for determining the fill factor and also proves that it is always less than one.

$$FF = \frac{V_m I_m}{V_{OC} I_{SC}} \quad (11)$$

Note that the value of a fill factor of an ideal solar cell is 100 %. That corresponds to a square I-V graph. However, it is not possible to obtain a square I-V graph with a real solar cell due to the losses occurring in a real solar cell. High quality photovoltaic cells (like silicon solar and inorganic cells) are characterized by high values of the fill factor (above 80 %) [44],[45].

2.5.6 Efficiency (η)

The efficiency of a photovoltaic cell is defined as the ratio of the maximum power produced by a cell to the power incident upon a cell, it is given by the following equation[46]:

$$\eta = \frac{V_m I_m}{P_{in}} \quad (12)$$

where the numerator is given by the $P_{mp}=V_m I_m$. Equation (12) is mostly used when analysing and contrasting the performance of various solar cells. The efficiency of a photovoltaic cell is affected by several factors like solar spectrum and temperature. To evaluate the efficiency of a photovoltaic cell, the standard test conditions, defined as value at a temperature of 25 °C, a solar irradiance (1000 W/m²) and AM 1.5 spectrum, have to be considered. By introducing the fill factor (11), the efficiency at maximum power point can be written as:

$$\eta = \frac{V_{OC} I_{SC} FF}{P_{in}} \quad (13)$$

The last equation shows that efficiency is directly related to V_{OC} and J_{SC} as well as the fill factor FF. which can be estimated from the current-voltage curve if we are simultaneously tracking the maximum power point. Both J_{SC} and V_{OC} are related to the band gap of a material [47],[48]. This gives a clear idea that optical band gaps of the absorber materials has to be optimized in order to design new solar cells with higher efficiencies. William Shockely and Hans Queisser were the first describing a thermodynamic approach for determining the highest theoretical efficiency of a one p-n junction solar cell absorber material [49]. They have shown that 30 % is the highest possible value in an absorber material with a band gap of 1.1 eV. The variation of efficiency with band gap is shown in the Figure 8.

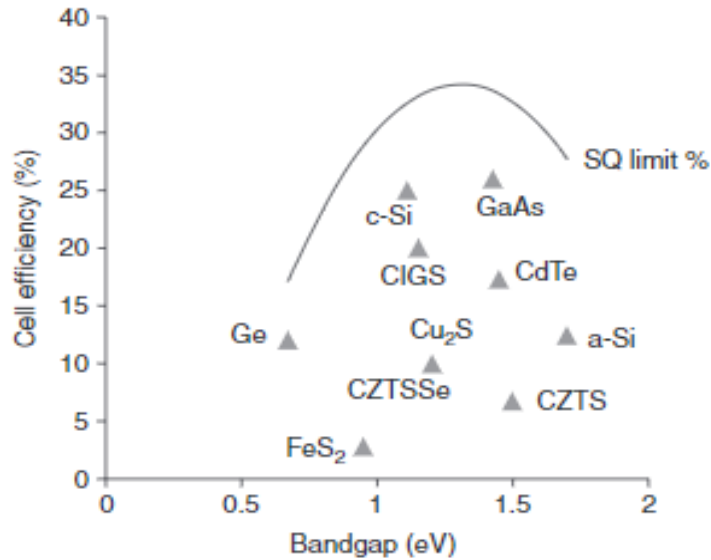


Figure 8: Efficiency of the solar cells as function of their energy gaps [50].

2.6 Current trends in photovoltaic technology

Solar cells are categorized into various generations based on the cost of materials and conversion efficiency. Over the past years highly efficient solar cells based on silicon (silicon wafers, mono-crystalline and poly-crystalline silicon) were developed and are used worldwide [51],[52]. Although the silicon solar cells were more efficient, the materials that were used to manufacture them were very expensive. Due to material cost, especially for silicon wafers, the second generation solar cells also called thin films were developed. Few examples of thin film solar cells include but not limited to CuInSe_2 , a-Si, CdTe, Cu(In, Ga)Se_2 and $\text{Cu}_2\text{ZnSnS}_4$ [53],[54]. Unlike the first generation (silicon) solar cells, thin film solar cells are cheaper, easy to fabricate and malleable, however, this type of solar cells are subjected to shorter lifetime and lower efficiency [55],[56]. As the new photovoltaic materials were gradually developing, the cost effective third generation solar cells were also developed. Examples of third generation solar cells are quantum dot solar cells, dye sensitized solar cells, organic solar cells and many more [57]. While third-generation solar cells have better conversion efficiency than thin film solar cells, they degrade easily due various factors such as humidity, temperature and ultra-violet light. The trend of photovoltaic technology development is shown in Figure 9.

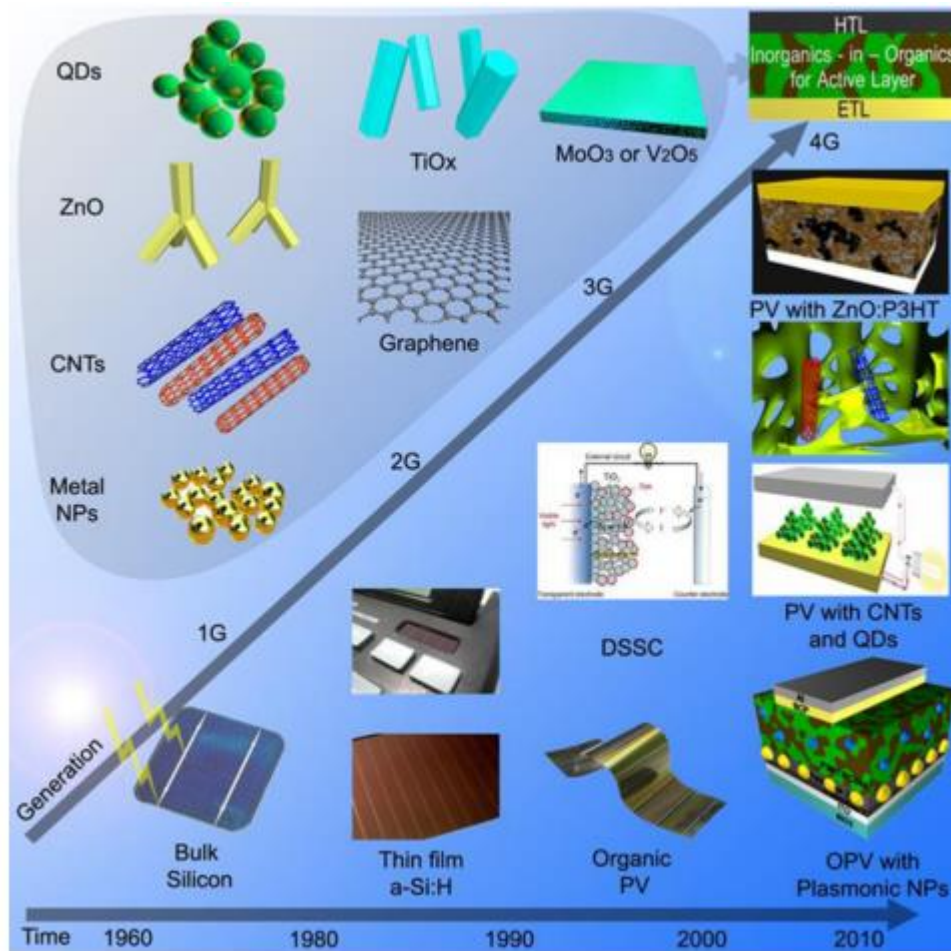


Figure 9: Trend in photovoltaic technology since 1960 [58].

Table 1 gives an overview and summarizes the efficiency achieved by various types of solar cells materials.

Table 1: Highest efficiencies obtained through various solar cells configurations[59].

Solar cell type	Efficiency	Laboratory/Institution
Crystalline Si	24.7	University of New South Wales
Multi Crystalline Si	20.3	Fraunhofer Institute of Solar Energy System
Amorphous Si	10.1	Kaneka
HIT cell	23	Sanyo Corporation
GaAs cell	26.1	Radbound University Nijmegen
InP cell	21.9	Spire Corporation
Multi junction cell	40.8	National Renewable Energy Laboratory
CdTe	16.5	National Renewable Energy Laboratory
CIGS	19.9	National Renewable Energy Laboratory
CuInS ₂	12.5	Hahn Meitner Institute
DSSC	11.1	Sharp
Organic solar cell	6.1	Gwangju Institute of Science and Technology

Since 2000 the photovoltaic production has been growing rapidly at a rate larger than 40 % worldwide. As a result the price of electricity dropped by 40 % between 2008 and 2011 [60]. In 2018 the global production data for solar cells was ranging from 100 GW to 115 GW [61]. However, it was later reported that the rate at which the electricity is consumed worldwide will drop to 2.4 % by the year 2030 [62]. This can be mitigated by increasing the usage of solar power globally. The first generation solar cells has been covering more than 80 % of the photovoltaic market in the past decade, however, second generation photovoltaic cells are expected to dominate the market in future. There is still room for improvement for thin film solar cells. New technology based on organic solar cells and dye sensitized solar cells are still under research level and not yet commercialized. As shown in Figure 10 the production of thin film solar cells was very low (about 13 % of the total produced power) in 2010. The global market is still dominated by standard crystalline silicon solar cells.

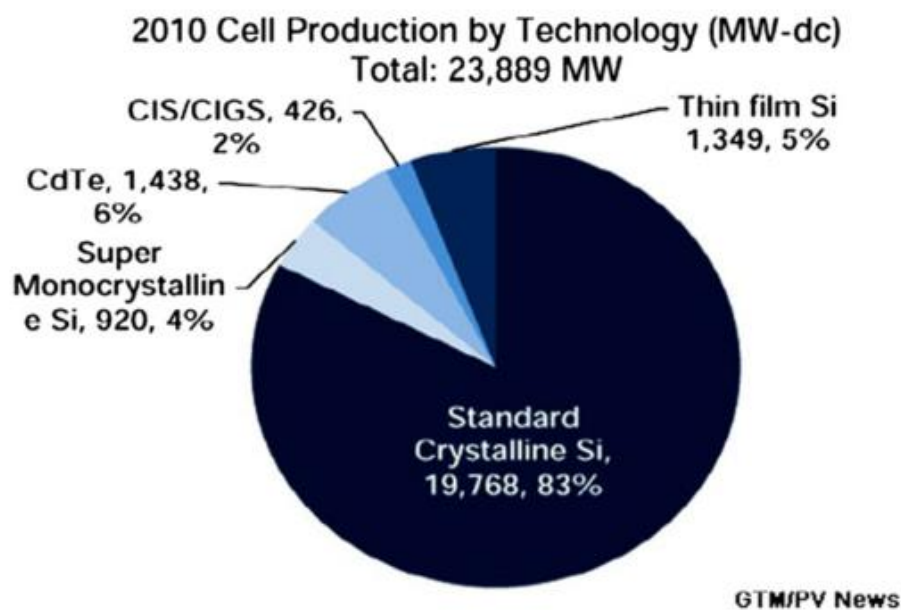


Figure 10: The global market share of various solar cells in 2010 [63].

Even though some thin film solar cells developed from CdTe and CIGS absorbers are commercialized and have a high record efficiency, they suffer from the issues of toxicity and scarcity. Materials like tellurium, gallium and indium are rarely found on the earth crust [64],[65],[66] and this issue limits the number of solar modules that could be manufactured from these elements in the market. Figure 11 shows the abundance of elements relative to their atomic number. On the other hand an element Cd is very harmful to the environment [67],[68],[69], any waste containing has to be handled and deposited with care. To address

these problems the environmentally friendly CZTS absorber was developed from earth abundant elements. This absorber material was developed by replacing In and Ga with Zn and Sn. The record efficiency achieved from a CZTS solar cell with structure CZTS/CdS is around 9.5 %. Though the efficiency is low there is still lot that can be improved to achieve a higher efficiency [70].

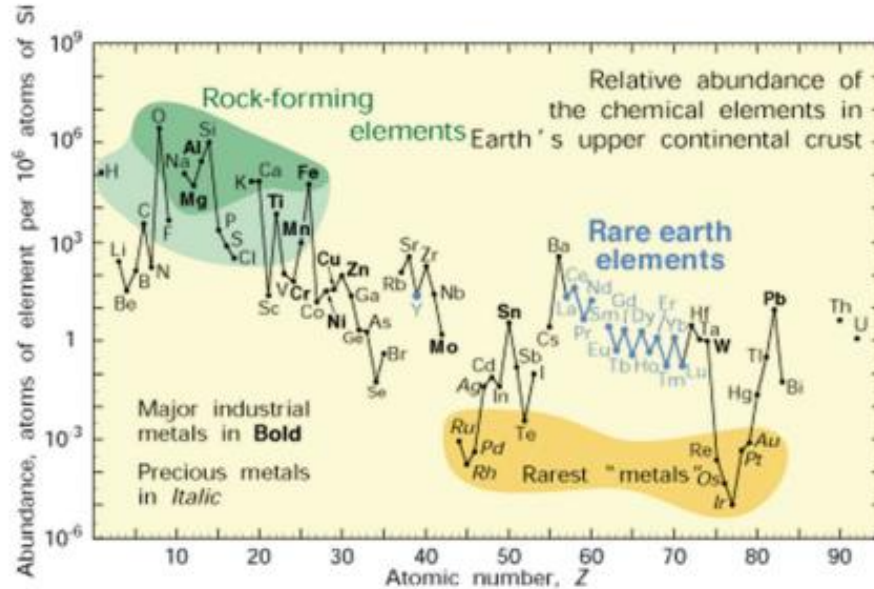


Figure 11: The abundance of elements in atoms of element per 10^6 atoms of Si as a function of atomic number [71].

2.7 Crystal structure of a $\text{Cu}_2\text{ZnSnS}_4$ (CZTS) compound

CZTS is a quaternary compound made up of the elements which are less toxic and abundant on the earth crust. Such elements are copper (Cu), zinc (Zn), tin (Sn) and sulfur (S). A quaternary CZTS compound exists in two dominant tetragonal crystal structures namely a kesterite and stannite, respectively. A kesterite structure is Zn rich while a stannite structure is Zn poor. Even though these structures have some similar properties, the position of the cations among them give rise to two different space groups, $I\bar{4}$ and $I\bar{4}2m$, respectively. A kesterite type structure belongs to the $I\bar{4}$ space group. Here, a single copper atom shares the same position 2a (0, 0, 0) with a zinc atom. The other remaining copper atoms go to the 2c (0, 1/2, 1/4) site and the 2d (0, 1/2, 3/4) site. The distribution of copper and zinc atoms in this structure leads to a p-type conductivity. On one hand a stannite type structure is a member of the $I\bar{4}2m$ space group in which the divalent cations are situated at the 2a site and monovalent

cations are located at the 4d (0, 1/2, 1/4) site. In both structures the position of Sn is the same, at 2b position (0, 0, 1/2). A unit cell of both a kesterite type structure and stannite type structure is shown in Figure 12. The atoms of copper, zinc and tin are denoted by blue, orange and red spheres, respectively.

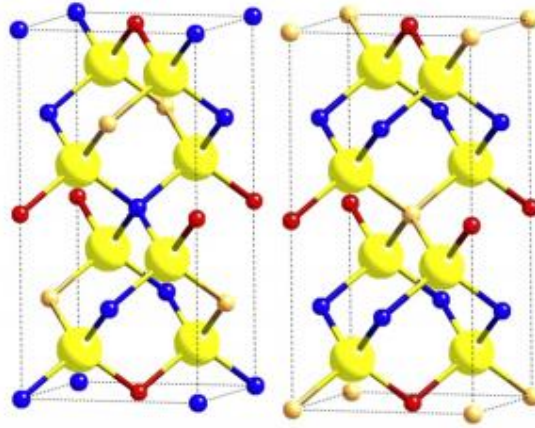


Figure 12: A unit cell of a kesterite CZTS (left) and stannite CZTS (right) [72].

2.7.1 Observable secondary phases in CZTS structure

It is not easy to obtain a single phase CZTS compound. In most cases secondary phases such as CuS_2 , SnS_2 , Cu_2SnS_3 , $\text{Cu}_2\text{ZnSn}_3\text{S}_8$ and many others are found in the CZTS structure [73]. To get more insight on how CZTS and all these additional compounds are formed, we need to consider the equilibrium phase diagram of Cu_2S - ZnS - SnS_2 given in Figure 13.

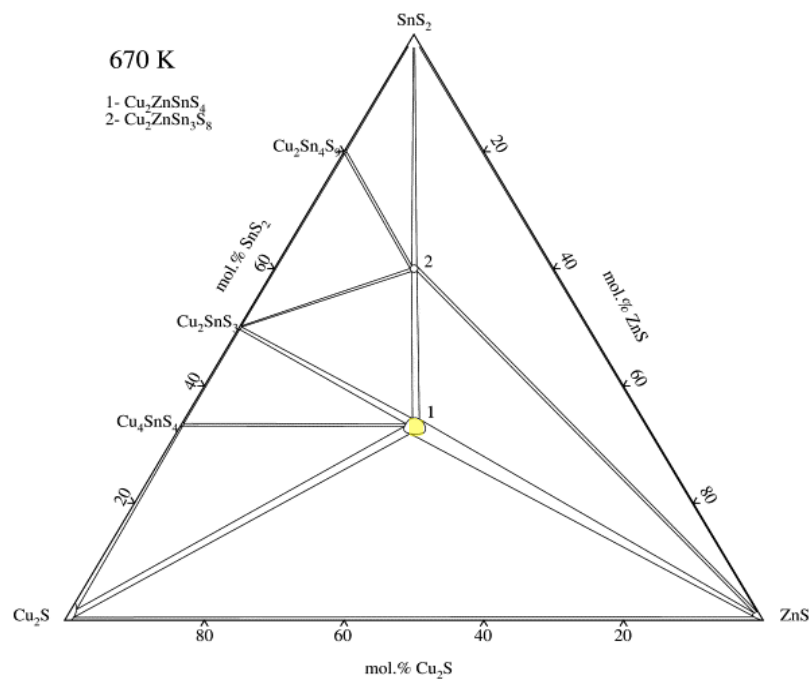


Figure 13: Equilibrium phase diagram for the Cu_2S - ZnS - SnS_2 [74].

As shown in Figure 13, a pure phase of CZTS crystals can only be obtained at specific region (region 1), while the secondary phases are formed at any other region except region 1. Many researchers had obtained a combination of CZTS and different secondary phases in a single structure. Some of the examples of CZTS thin films with secondary phases were prepared by sputtering from various source targets containing Zn, Sn, S, and Cu at room temperature. Immediately after sputtering the films were sulfurized at temperatures between 250 °C and 550 °C. As shown in Figure 14 the XRD patterns revealed that secondary phases (ZnS, Cu₂S and SnS₂) exist in the structure.

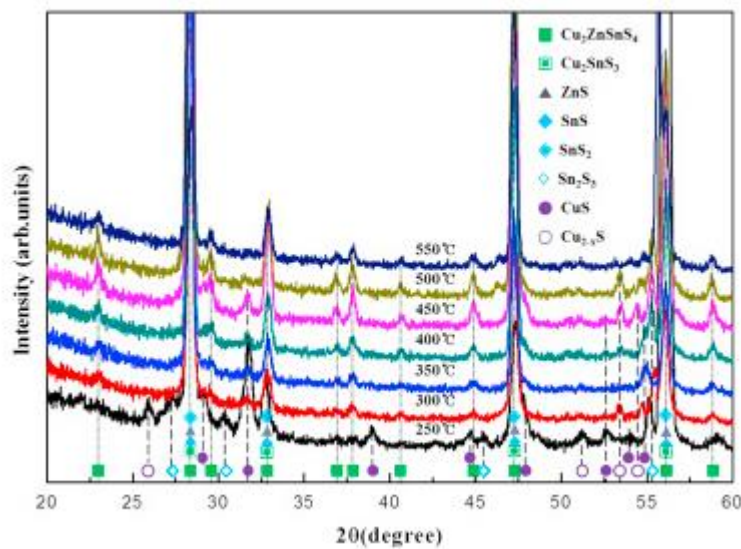


Figure 14: Typical XRD diffractograms of CZTS layers prepared at different temperatures [75].

2.8 Electrical and optical properties of a CZTS absorber

The electrical and optical properties are very important when selecting the best materials for photovoltaic applications. The electrical features of CZTS thin films are influenced by temperature (substrate and annealing temperature) and composition: The resistivity of the films decreases as the temperature increases. CZTS thin films, which are rich in Cu and Sn, have a low resistivity. Thus, those are not good for application in photovoltaic cells. As reported in literature, CZTS absorber exhibit p-type conductivity with values of resistivity ranging from 10^{-3} to $10^3 \Omega\text{cm}$ [76],[77]. The reported values of carrier concentration are in order of 10^{17}cm^{-3} [78],[79].

Like the electrical properties, the optical properties are also dependant on temperature. The optical band gap of the CZTS thin films narrows as the temperature rises. The optical band of the CZTS thin films reported in literature ranges from 1.4 to 1.7 eV which is very close to its optimum band gap of 1.5 eV [80], however, some researchers had found a optical band gap of 1.2 eV. In addition, CZTS thin films have a very high absorption coefficient, which is greater than 10^4 cm^{-1} in the visible range [81]. All these properties together make a CZTS absorber to be a good absorber material for converting solar energy to electrical energy.

2.9 Design of CZTS solar cells

The CZTS solar cell belongs to the second generation of photovoltaic technology known as thin films solar cells. It is an emerging substitute for the CIGS solar cell. All thin film solar cells have a similar structure, but only the structure of traditional CZTS solar cell will be described in this section. Traditional CZTS solar cell consists of a p-type absorber (CZTS) layer deposited on a glass coated with an electrode layer (usually molybdenum). Then an n-type buffer layer grown on top of absorber forming a p-n junction. Other two n-type thin film (window) layers of transparent conducting oxides (i-ZnO and ZnO:Al) are deposited on the buffer layer. A cell is completed by growing the aluminium grids. These grids act as front contacts. A typical architecture of a traditional CZTS solar cell is shown in the Figure 15.

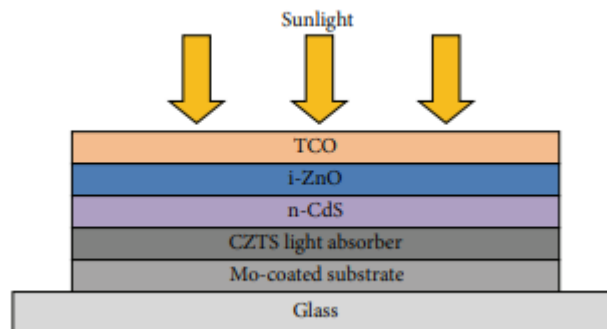


Figure 15: A typical architecture of a CZTS solar cell [82].

2.10 Background Information of kesterites solar cells

A large V_{OC} deficit associated with the CZTS solar cells can be improved by exploring other Cd free buffer layers. Most of these Cd-free buffer layers are based mainly on zinc (Zn) and indium (In) compounds. Few examples are ZnS, ZnO and In_2S_3 [83]. On the other hand, the optical band gap of CdS is very narrow, ranging from 2.4 to 2.5 eV and this lowers the

performance of the cell. Most of the Cd-free buffer layers like ZnS have a wider band gap which can help to optimize the performance of the cells [84]. In 2018 Xin Cui et al [85] reported CZTS with efficiency of 9.3 % using Cd-free buffer layer ZnSnO. Figure 16 shows the current density versus voltage (I-V) curves as well as the external quantum efficiency (EQE) of the CZTS/ZnSnO cells obtained.

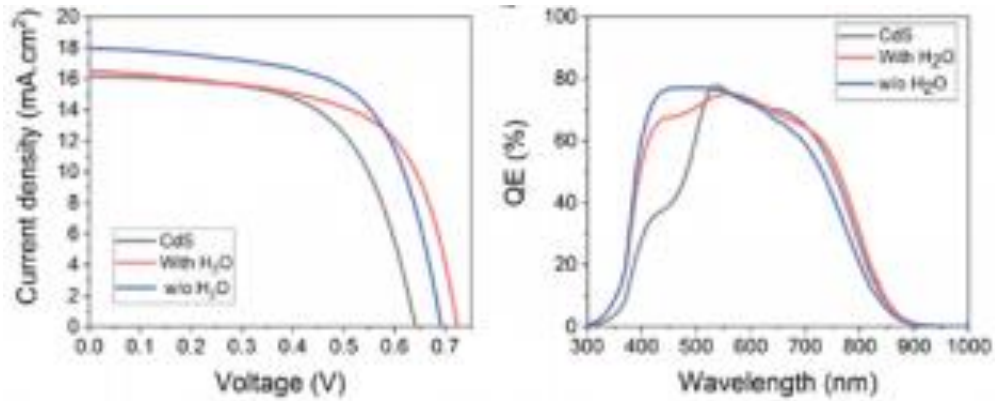


Figure 16: I-V characteristics and EQE of the CZTS/ZnSnO cells [86].

Studying how the elemental composition of CZTS or CZTSSe films influence the efficiency of a cell is also a crucial step towards improving the efficiency of the kesterite solar cells. Best performing cells are found to have Zn rich and Cu poor regions in their absorbers [87],[88]. In addition, the presence of secondary phases caused by the reaction of copper and sulfur in the CZTS films degrades the conversion efficiency of CZTS solar cells. Such phases make it very difficult to achieve a CZTS compound with most favourable values of $Cu/(Zn + Sn)$ and Zn/Sn ratios. Therefore, reducing the amount of copper in the samples decreases the chances getting secondary phases hence improving efficiency the cells. A significant increase of the $Cu/(Zn + Sn)$ ratio lowers efficiency of the CZTS cell [89]. Figure 17 shows the current – voltage curves of two kesterite cells, one prepared under stoichiometric conditions and the other by tuning $Cu/(Zn + Sn)$ ratio. The efficiency of the built cells was 0.37 % and 1% respectively.

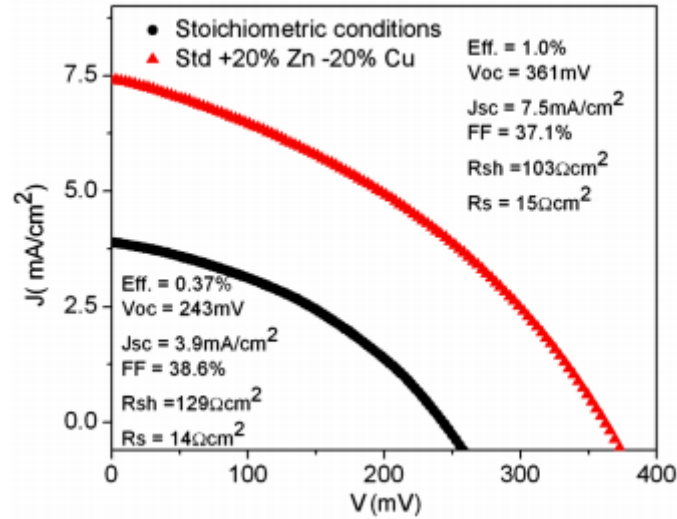


Figure 17: Current -Voltage curves of a cell fabricated with absorber under stoichiometric conditions and a cell obtained by reducing Cu and increasing amount of Zn [90].

Doping the CZTS absorber with alkali metals like sodium (Na) and potassium (K) helps to enhance the efficiency of CZTS solar cell. The enhanced efficiency is associated with improved crystallinity, grain size and band gap. Zhengfu Tong et al [91] produced a CZTS films with improved crystallinity and grain size by doping with K. The complete solar cell showed that short circuit current density raise up while open circuit voltage and series resistance (R_s) dropped. Incorporation of these alkali metals to the CZTS also increases the carrier concentration and this improves the electrical performance. Figure 18 shows the current – voltage curves for Na and Sb doped kesterite solar cells with efficiency about 5.7 %.

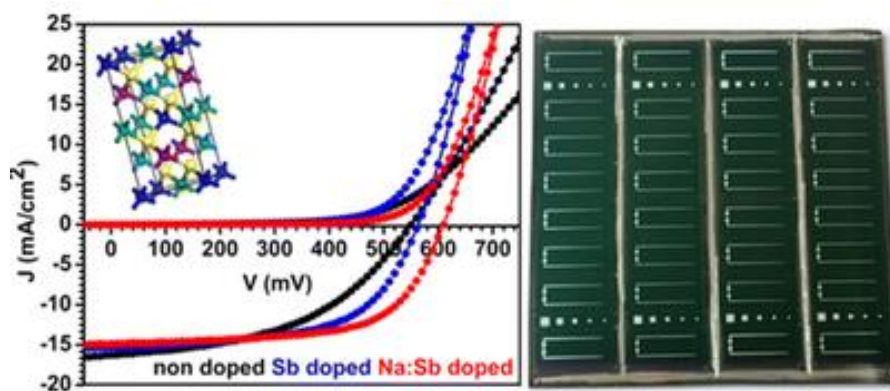


Figure 18: Current - Voltage curves of Na and Sb doped cell and the complete cell [92].

Another way of increasing the efficiency of the kesterites (CZTS or CZTSSe) solar cells is by adopting the bifacial cell structure. Here the Transparent Conducting Oxides (TCO), such as fluorine doped tin oxides (FTO) or tin doped indium oxide (ITO) are used as the back contacts or electrodes instead of molybdenum (Mo). The problem encountered with bifacial cell configuration is that some of these transparent conducting oxides, like ITO, reacts with the absorber at a higher temperature leading to expansion of the lattice, however, the optical variables like band gap and absorption coefficient are slightly affected [93]. Figure 19 shows the current – voltage curves of bifacial kesterite (FTO/CZTSe and ITO/CZTSe) solar cells prepared at a temperature greater than 500 °C. The efficiency of FTO/CZTSSe and ITO/CZTSSe obtained under illumination were 6.05 % and 4.31 %, respectively. The lower conversion efficiency of ITO/CZTSSe cell might be caused diffusion of indium from ITO substrate to the absorber. Several solar devices such as solar windows, tandem solar cells and others use bifacial solar cells.

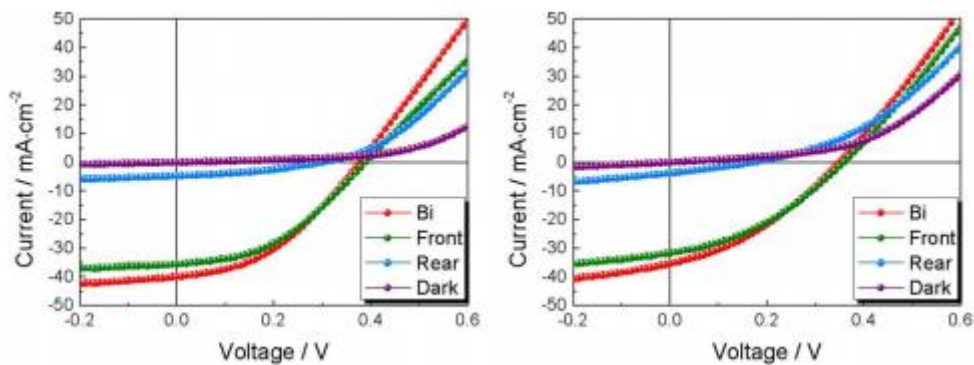


Figure 19: Current -Voltage characteristics of FTO/CZTSSe and ITO/CZTSSe solar cells under bifacial, front, rear and dark illumination [94].

2.11 Methods of growing CZTS thin films

The techniques of growing CZTS films can be split into two classes namely vacuum based techniques (co-evaporation, pulsed laser deposition and sputtering) and non-vacuum techniques (sol-gel and spray pyrolysis). Although the physical vapour deposition techniques can lead to thin films with higher power conversion efficiency, they are more expensive compared to the simple and low-cost chemical methods. One of the common limitations among all these methods is the difficulty in obtaining thin films that exhibit pure phase of kesterite. Controlling the composition of the thin films is also a challenge. Despite these

challenges several CZTS thin films with excellent properties had been achieved [95],[96]. Some physical vapour and chemical growth methods are described below.

2.11.1 Thermal evaporation

Thermal evaporation is one of the vacuum-based techniques that can be used to deposit various thin films. This technique is further divided into few methods namely resistive heating and inductive heating [97],[98]. Resistive heating is a simple method under which the heating electrodes are used to heat the source material (usually a powder) carried in a dimple boat. One important factor that has to be considered when choosing a suitable material for designing a boat is the melting temperature of both the dimple boat and source. The melting temperature of a dimple boat has to be greater than that of a source. In this method the rate at which the material is evaporated can be controlled by regulating the amount of current supplied to the electrodes. The problem with thermal evaporation is that when temperature is very high the boat may evaporate and contaminate the source material, the source material may mix with a vapour from boat leading to films with poor composition ratio. Moreover, a boat can break due high temperature if inappropriate material for designing a boat is chosen. Most of the problems encountered in resistive heating can be effectively eliminated by depositing through inductive heating. Here a crucible surrounded by water-cooled radio frequency (RF) inductive coils is used to carry the source material. These inductive coils are the ones that supplies energy. Though inductive heating is better than resistive heating, it is still difficult to avoid contamination. The contamination here arises from the crucible. The typical representations of resistive heating (a) and inductive heating methods (b) are shown in Figure 20.

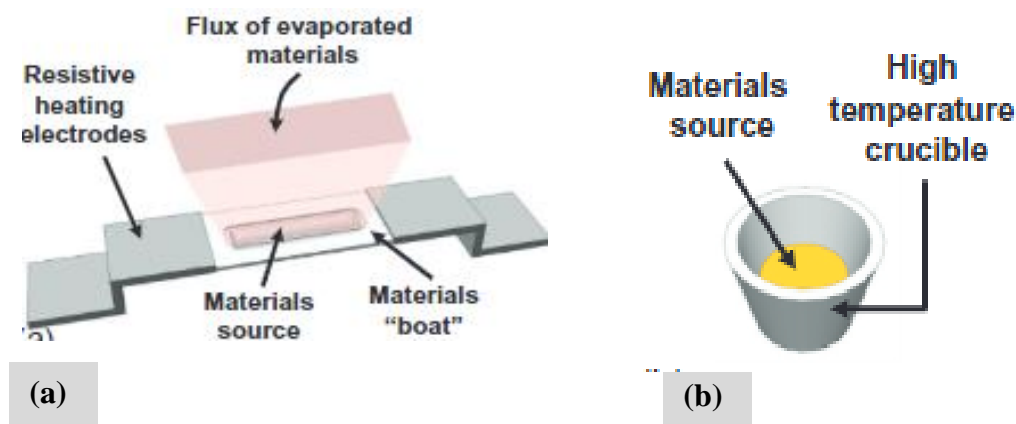


Figure 20: Typical representation of (a) resistive heating and (b) inductive heating [99].

Thermal evaporation had been used by a lot of researchers in recent years to synthesize CZTS films. Shi et al [100] had successfully grown the CZTS thin films via thermal evaporation from a powder that was prepared by mixing CuS, ZnS and SnS powders. The grown films had amorphous structure and the films with crystalline structure were obtained after annealing at 300 °C under nitrogen atmosphere. In 2013 Jiang et al [101] synthesized the CZTS films following a two-step process. They started by depositing Cu, Zn and Sn precursors on glass substrates coated with molybdenum via thermal evaporation followed by sulfurization under sulfur ambience. In their work they studied the effects of sulfurization temperature and source composition on the properties of the films, their results showed that films prepared from Cu-rich sources exhibit multi-phase structure with $\text{Cu}_{1.96}\text{S}$ and CZTS phases while those prepared from Cu-poor sources does not show any secondary phase.

2.11.2 Sputtering

Sputtering is another technique for depositing thin films. In this technique the ionised Ar gas (plasma) is used for depositing the materials. To activate plasma a voltage source either direct current (DC) or alternating current (AC) is applied across the anode and cathode. An Ar atom is ionized to an Ar^+ ion by a collision between Ar atoms and a free electron discharged close to the cathode while on its way to the anode. As a result of this collision an additional free electron is produced that will in turn collide with other Ar atoms as it will be accelerated towards the anode. In contrast Ar^+ ions produced in this process will go up to the cathode, a portion of these Ar^+ ions with high kinetic energy may sputter off the uppermost layer of the target source and the sputtered material will undergoes a semi-ballistic motion from the source to the substrate [102]. Another portion of the Ar^+ ions help to maintain plasma's self-sustaining activity whereas the remaining portion can be embedded into the source. In the sputtering system the target source and substrate are placed at the cathode and anode respectively. Figure 21 shows a simplified representation of a sputtering system. Sputtering can help to prepare various materials like insulators, mixtures and metals with precise composition and uniform thickness. Furthermore, the distribution of particles and size of the gains can be controlled in sputtering. The rate at which materials grow during the deposition is influenced by few factors; these are sputtering power, sputtering yield and pressure of ionizing gas. Sputtering deposition technique can be further divided into three methods namely magnetron, DC and RF sputtering. DC sputtering is a very simple method, however, it is characterized by lower deposition rates. RF sputtering has a larger deposition rate compared to DC sputtering. Unlike in DC sputtering it is easier to deposit insulators through

RF sputtering method. Magnetron sputtering has higher rates compared to DC and RF sputtering: This method also helps to achieve materials with better adhesion.

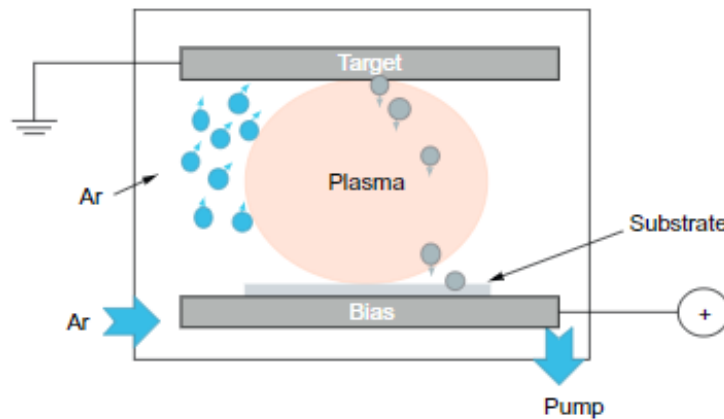


Figure 21: A simplified description for a sputtering system [103].

Many researchers had already used sputtering methods to deposit CZTS thin films. In 2005 Tanaka et al [104] fabricated CZTS thin films using hybrid sputtering set-up consisting of two sputter sources (for Cu and Sn) and two effusion cells (for Zn and S). The films were obtained by depositing Sn, Zn and Cu sequentially followed annealing in S containing environment. They also varied the substrate temperature. A pure phase of CZTS was achieved at 400 °C. Early 2012 Sun et al [105] took a different route of sputtering. This group used RF magnetron sputtering to deposit CZTS layers on glass substrates using a CZTS target as source. The CZTS layer were further sulfurized in Ar + H₂S atmosphere. The thin films, obtained before annealing, exhibit a single phase CZTS structure as revealed by the X-Ray diffraction and Raman spectroscopy. Later in 2013 Inamdar et al [106] grown the CZTS thin films on the soda lime glass substrates via RF magnetron sputtering technique. The films were further annealed in a nitrogen atmosphere at 350 °C and 550 °C. The grown films had a poor Cu/ (Zn + Sn) ratio and this ratio was enhanced by growing a thin layer of Cu on top of the CZTS layer and subsequent annealing in a nitrogen atmosphere. As result crystal structure of the films were improved.

2.11.3 Sol gel

In a sol-gel technique, materials such as sheets, fibres, thin films, and thick films can fabricated at a low temperature from solutions that contain precursors (metal compounds), water, alcohol and acid or a base. Here water, alcohol and acid or base work as hydrolysing agent, solvent and catalysts, respectively. In this technique two major processes (hydrolysis

and poly-condensation) are involved. Firstly, metal compounds are hydrolysed followed by subsequent poly-condensation of products released from hydrolysis. These two processes produce sol. A sol would be turned into a wet gel in the next series of reactions. A wet gel consists of solvents, which can be removed by evaporation producing a dry gel. Further heating a gel gives rise to different products as shown in Figure 22. The advantage of using sol-gel technique is to achieve the most stable surfaces and larger surface area. There are several methods that fall under sol-gel, some of them include casting and spin coating [107]. Casting is used to make bulk bodies (sheets) and spin coating is used for producing thin and thick films. Spin coating is the mainly used method by researchers in the field of material science and solar energy conversion to deposit CZTS thin films.

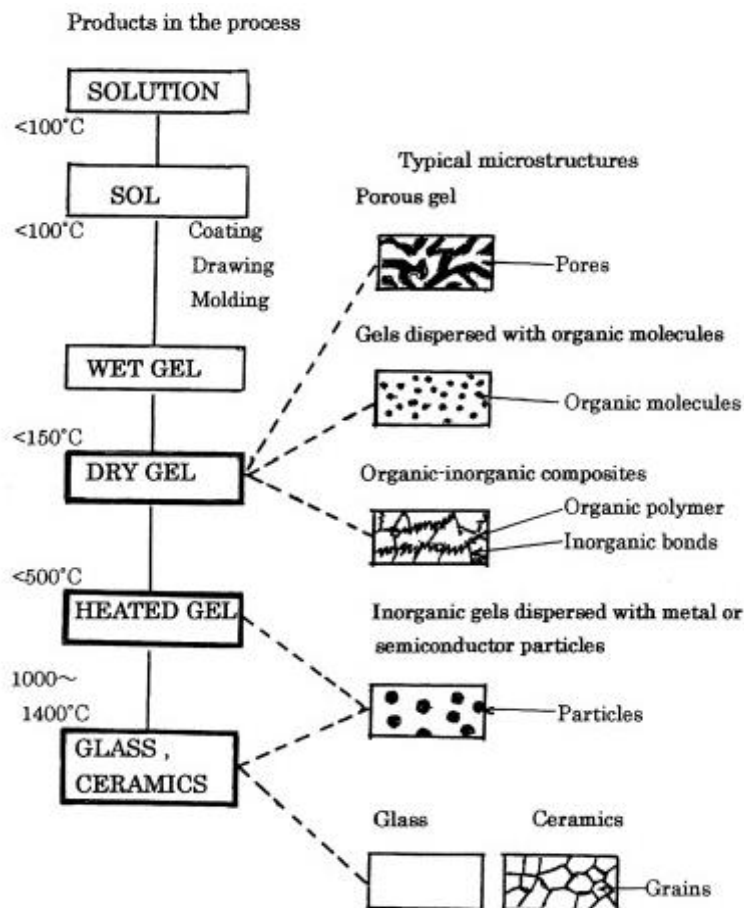


Figure 22: Steps involved in sol-gel method and some possible products obtained from sol-gel technique [108].

In 2009 Tanaka et al [109] prepared CZTS layers on glass substrates coated with molybdenum through sol gel method. They deposited the thin films by spin coating the precursor onto the glass substrates at 3000 rpm followed by drying at 300°C for 5 minutes in

open air. The thin films obtained were further annealed at 500 °C for an hour under $N_2 + H_2S$ containing environment. Their results showed that some MoS_2 and Mo phases exist in the CZTS structure, however, the band gap was close to 1.5 eV which is the theoretically determined band gap of the CZTS. Later in 2011 Tanaka et al [110] also investigated the effects of varying Cu/ (Zn + Sn) ratio in the sol-gel solution on the morphology and optical properties of the thin films. In their work Zn/ Sn ratio was not varied. They concluded that decreasing Cu/ (Zn + Sn) in the sol-gel solution leads to an increase of the grain sizes and band gap. In the year 2011 Maeda et al [111] studied the effects of reducing the amount H_2S gas during sulfurization on the properties of CZTS thin films grown by sol-gel method. They varied the concentration of H_2S between 3 % and 20 % during sulfurization. They found that as the concentration of H_2S was reduced the quantity of S in the thin films also reduced until the concentration reached 5 %. Below 5 % the concentration of S increased. Furthermore, the grain size of the thin films sulfurized at a lower concentration of H_2S (3 %) was larger compared to others.

2.11.4 Spray pyrolysis

Recently the spray pyrolysis technique had been applied in wide range of research industries to prepare thin films, powders and ceramic coatings. Many researchers adopt this technique because it is easy and cost-effective [112]. It is very simple to build a custom made set up for spray pyrolysis. The apparatus needed are the atomizer, substrate heater, pumps and small precursor solution container. During the spray pyrolysis method, the precursor solution is carried by a gas (compressed air or nitrogen) to a heated substrate in form of droplets. When these droplets hit the substrate, they form a disk-shaped structure and go through pyrolysis. The main factors that determine the thickness, particle size and shape of the resulting nanostructure include temperature of the furnace or substrate, distance between the substrate and atomizer, momentum of the droplets and spray duration [113]. In addition, the additives and concentration of the reactants in the precursor affects the morphology of the films [114]. Figure 23 shows the typical set-up for spray pyrolysis technique.

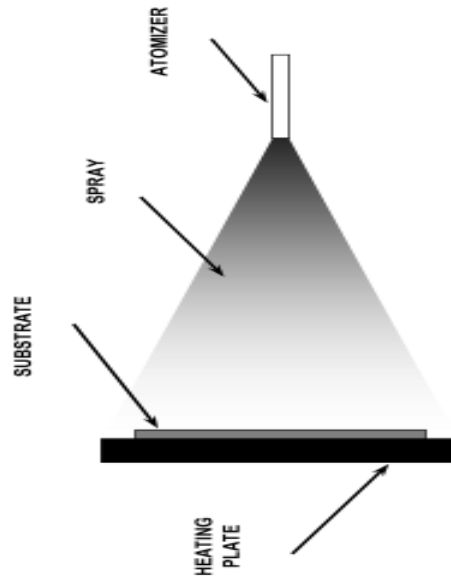


Figure 23: Typical Set-up for spray pyrolysis [115].

In 2006, Kamoun et al [116] carried out a study to find out how does varying the substrate temperature and period of deposition affects the properties of CZTS thin films grown by spray pyrolysis. In order to investigate these two conditions, they deposited the thin films for a duration of 30 and 60 minutes at a temperature ranging from 553 to 633 K. From their observation the thin films with the best crystallinity were obtained at higher substrate temperature, and the thin films were deposited for longer duration (60 minutes). The X-Ray diffraction showed that the thin films were multi-phase with peaks corresponding to CuS, CZTS and Cu₂S. Kumar et al [117] reported on the effects of temperature on the properties of CZTS thin films around 2009. They had successfully deposited the CZTS thin films at temperature range from 643 K to 683 K, and their results had showed that the crystal structure of the CZTS thin films was enhanced by increasing temperature. In 2011 Rajeshmon et al [118] investigated on how the precursor influence the properties of CZTS thin films. They varied the source of tin, stannous chloride and stannic chloride, which were used as sources of tin. They found that a film prepared from solution containing stannic chloride exhibit better crystalline structure and optical properties (a band gap was 1.5 eV and absorption coefficient greater than 10^4 cm^{-1}) compared to a film grown from solution containing stannous chloride. For this project the CZTS thin films were fabricated through a simple and cost-effective spray pyrolysis method.

CHAPTER 3 : MATERIALS AND METHODS

3.1 Arrangement of a spray machine

In this project, the CZTS and In_2S_3 thin films were deposited on the glass substrates by home-made spray pyrolysis system. Compressed air was used to carry solution towards the substrate. The experimental set for this experiment is shown on Figure 24, the components are labelled with numerical numbers and their purposes are also described in what follows.

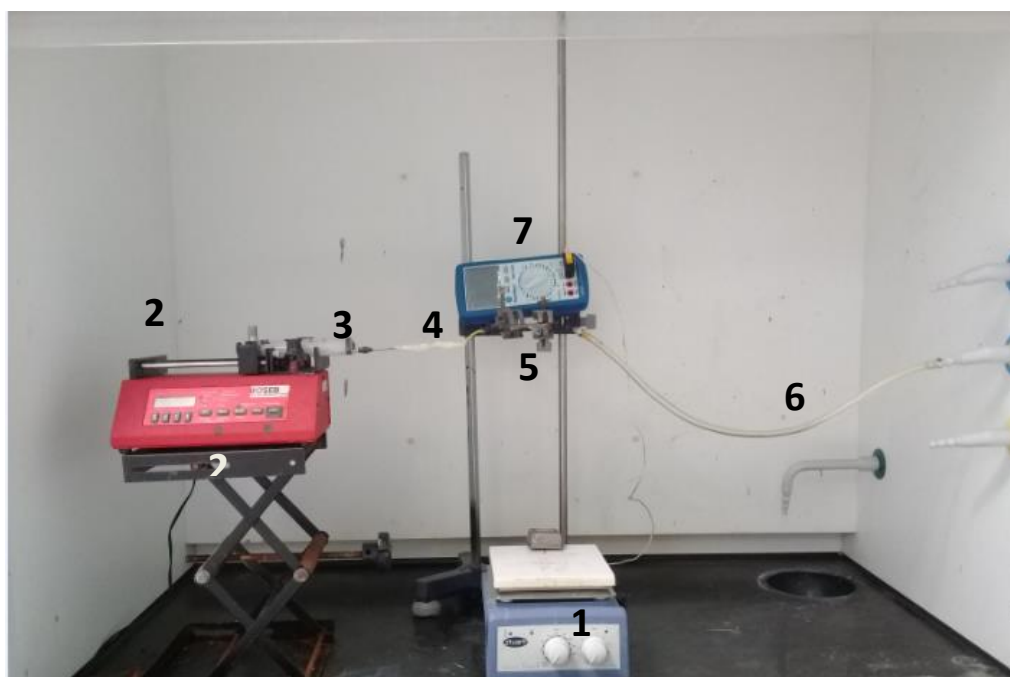


Figure 24: Experimental set-up for spray pyrolysis.

The purpose of the heater (1) is to heat the substrates to a particular temperature. The pump labelled as (2) pumps the precursor solution in the syringe, and the solution from the syringe (3) is carried by a tube (4) to the nozzle (5) where it meets with a compressed air coming from the compressor through tube (6). A compressed air carries the solution from the nozzle to the substrates in form of droplets. The multi-meter (7) measures the substrate temperature.

3.2 Cleaning the substrates

In this research the borosilicate glasses and Fluorine-doped Tin Oxide (FTO) coated glasses were used as substrates. Prior to deposition the glass substrates were washed sequentially with acetone, ethanol and distilled water. The purpose of cleaning the substrates was to remove any dust or dirt from the glass surfaces that might lead to uneven thin film growth.

Furthermore, the dirt on the surface of the glass substrates may cause failure of thin-films to stick to the surfaces of the substrates. Firstly, the glass substrates were placed in a beaker containing acetone and heated to 250 °C for 10 minutes using a hot plate. Figure 25 (a) shows the heated glass substrates. After 10 minutes the glass substrates were removed from acetone, dipped in distilled water and immersed in a beaker with ethanol. Then the beaker was placed in an ultrasonic bath tank (Bransonic) containing water as shown Figure 25 (b). The ultrasonic bath tank knob was then adjusted to 35 sonics and the beaker with the glass substrates was left in the tank for 35 minutes. Lastly the glass substrates were rinsed with distilled water three times and dried with flowing nitrogen gas.

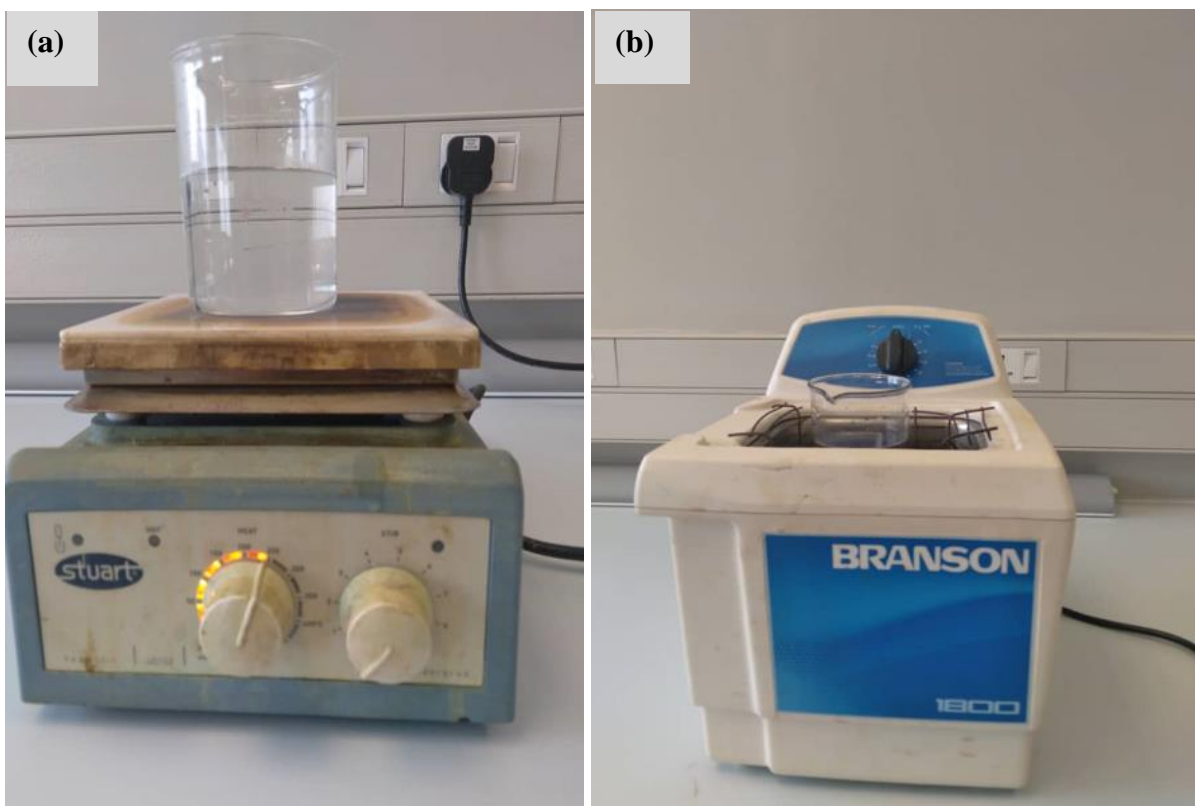


Figure 25: The glass substrates in (a) acetone and (b) ethanol.

3.3 Depositing the CZTS thin films

Various salts such as copper chloride dehydrate, zinc acetate dehydrate, zinc nitrate hexahydrate, tin (II) chloride dehydrate, and thiourea from Sigma Aldrich were used for preparation of CZTS thin films, however, tin (IV) chloride was used in a liquid state. All salts were dissolved in distilled water to obtain 0.02 M of (copper chloride, zinc acetate, zinc nitrate, tin (II) chloride) and 0.08 M of thiourea solutions, tin (IV) chloride solution was

diluted with distilled water to obtain 0.02 M aqueous solution of tin (IV) chloride. The concentration of thiourea was four times that of copper chloride to avoid reduction of copper by thiourea and also to compensate for loss of sulfur during pyrolysis. In this study four different CZTS samples were obtained by varying the two sources of zinc and two sources of tin, the copper salt and sulfur were not changed throughout the experiment. The table 2 shows how the zinc and tin salts were selected to obtain four different samples.

Table 2: Pair of zinc and tin sources used for preparation of four CZTS samples.

Sample name	Source of zinc	Source of tin
CZTS001	Zinc acetate dehydrate	Tin (II) chloride dehydrate
CZTS002	Zinc nitrate hexahydrate	Tin (II) chloride dehydrate
CZTS003	Zinc acetate dehydrate	Tin (IV) chloride
CZTS004	Zinc nitrate hexahydrate	Tin (IV) chloride

The four different solutions used for depositing CZTS thin films were prepared by mixing 0.02 M of (copper (II) chloride, zinc acetate or nitrate, tin (II) or tin (IV) chloride) solutions and 0.08 M of thiourea solution in a beaker as described earlier (see table 2). The solutions were stirred with a magnetic stirrer for 10 minutes to obtain clear solutions. Then 35 ml of each solution was sucked using a syringe and the syringe pump was set to a rate of 1.0 ml/min. Before spraying each solution, the spraying system was adjusted such that the distance between the substrates and the nozzle was 25 cm. Cleaned glass substrates were heated up to 300 °C for five minutes with a hot plate. Then the solution was sprayed on the heated glass substrates using compressed air as a carrier gas and substrate temperature was held constant at 300 °C during deposition of all samples. After deposition, the four samples were allowed to cool naturally and taken for characterization.

3.4 Synthesizing In₂S₃ thin films

The In₂S₃ thin films were also deposited by the spray pyrolysis technique. For the deposition of the In₂S₃ samples, indium chloride tetra-hydrate and thiourea from Sigma Aldrich were used as sources of indium and sulfur, respectively. In this experiment the composition of the In₂S₃ thin films was examined by varying thiourea concentration in steps of 0.005 M. An aqueous solution of indium chloride (0.015 M) was prepared by dissolving indium chloride tetra-hydrate salt in distilled water and the four aqueous solutions of thiourea (0.090 M, 0.095 M, 0.100 M and 0.105 M) were obtained by dissolving specific masses of thiourea in distilled

water. An excess amount of thiourea was required to compensate for loss of sulfur at higher temperatures.

Four set of precursor solutions were prepared by mixing 0.015 M of indium chloride solution with each of the four thiourea solutions in separate beakers, and the mixtures were stirred with a magnetic stirrer for 10 minutes. Then In_2S_3 thin films were grown on preheated glass substrates at $300\text{ }^\circ\text{C}$ by spraying 15 ml of each prepared solution over the substrates at a rate of 1.0 ml/min. Compressed air was used to carry the solutions in form of mist towards the substrates and the distance between the substrates and nozzle was set at 25 cm for deposition of all samples. After deposition all samples were annealed at $300\text{ }^\circ\text{C}$ for 30 minutes. After annealing the samples were allowed to cool naturally before taken for characterisation. The samples were given names as $\text{In}_2\text{S}_3_{0.090}$, $\text{In}_2\text{S}_3_{0.095}$, $\text{In}_2\text{S}_3_{0.100}$ and $\text{In}_2\text{S}_3_{0.105}$. The numerical numbers indicate the corresponding concentration of thiourea used in sample preparation.

3.5 Fabricating FTO/CZTS/Ag and FTO/ In_2S_3 /CZTS/Ag solar cells

In order to investigate the photo response of CZTS thin films, the CZTS layers with good structural and electrical properties (CZTS001 and CZTS003) were selected and deposited on FTO coated glass substrates as described under section 3.3. Then a 100 nm Ag layer and Ag strip were deposited on the CZTS layer and FTO layer, respectively. Ag was deposited as outlined under section 3.6.

The two CZTS absorber layers and the one In_2S_3 layer with best characteristics were chosen and used for building two superstrate-type CZTS solar cell prototypes with structure FTO/ In_2S_3 /CZTS/Ag. Figure 26 (a) shows the architecture of the solar cells produced in this work. Firstly, the n-type In_2S_3 buffer layer ($\text{In}_2\text{S}_3_{0.095}$) was deposited on the two FTO coated glass substrates, the In_2S_3 layer was deposited as described under section 3.4. Then each p-type CZTS layer (CZTS001 or CZTS003) was grown on top of the prepared n-type In_2S_3 buffer layer forming a p-n junction. The CZTS layers were prepared as described under section 3.3. Finally, the contacts of each cell were made by depositing Ag layer on top of CZTS layer and Ag strip on the FTO layer through radio-frequency (RF) magnetron sputtering as described under section 3.6. After depositing Ag layer, Cu tape was used to connect the cables to Ag layer. The two produced solar cells prototypes are named as Cell-A (FTO/ In_2S_3 /CZTS003/Ag) and Cell-B (FTO/ In_2S_3 /CZTS001/Ag), respectively. Figure 26 (b) presents the two solar cells (Cell-A and Cell-B) produced in this work.

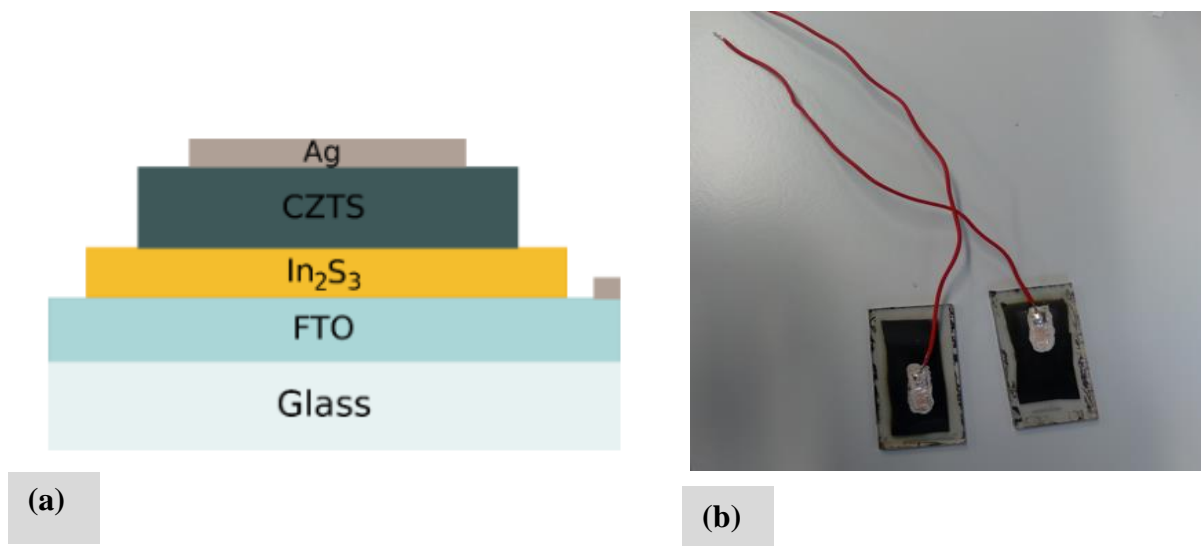


Figure 26: The (a) architecture of the FTO/ In_2S_3 /CZTS/Ag solar cells and (b) FTO/ In_2S_3 /CZTS/Ag.

3.6 Deposition of Ag electrodes

The Ag layers was firstly grown on a cleaned borosilicate glass substrates through RF magnetron sputtering using TF500 machine as shown in Figure 27. This machine can perform three deposition methods being thermal evaporation, electron beam, and RF magnetron sputtering. The Ag target attached to the Cu plate was used as a source. The diameter, thickness and purity of the target were 2 inches, 4 mm and 99.99 %, respectively. Firstly, the target was placed in the target holder and the glass substrates were placed on the substrates holders which was about 25 cm above the target. Then the deposition chamber was evacuated to 6.51×10^{-5} mbar, the RF power and argon rate were set to 100 W and 14.0 SCCM respectively. When chamber pressure reached 6.51×10^{-5} mbar, pre-sputtering was carried out for 10 minutes. After pre-sputtering, the first sample was deposited for a period of 20 minutes. Since the first sample was very thick, the experiment was repeated but the time for actual sputtering was reduced 5 minutes in-order to obtain a thin film about 100 nm thickness with good properties. After obtaining a good Ag film at 5 minutes, the contacts for the cells were made by depositing 1 cm x 2 cm Ag layer and 1 cm long Ag strip on the CZTS layer and FTO layer respectively. Hence the active area of each cell was 2 cm^2 .



Figure 27: TF 500 machine.

3.7 Characterizing the CZTS and In₂S₃ layers

Various techniques were employed in the characterisation of CZTS and In₂S₃ thin films. The structural properties of the films were studied via X-Ray diffraction and Raman Spectroscopy. Other properties such as thickness, optical properties, electrical properties, morphology, and composition were studied through Stylus profilometry, UV-Vis spectroscopy, Hall measurement, Scanning electron microscopy, Atomic force microscopy and Energy-Dispersive X-Ray spectroscopy. These methods are briefly described below.

3.7.1 X-Ray Diffraction

X-Ray diffraction is a non-destructive method that uses the X-ray scattering phenomenon to identify the nature of materials. Various structural parameters of materials like grain size, crystallinity, dislocation density, strain, crystal defects and others, can be obtained through this method. An instrument used in this technique is called an X-ray diffractometer. It has an X-ray tube which consists of a pair of electrodes (anode and cathode). The anode is usually made from metals with high density such as Cu, W, Mo and others. The cathode is made from a tungsten filament which produces electrons through a process known as thermionic emission when it is heated. When electrons with high kinetic strike a metallic target at the anode in an X-ray tube, X-rays are produced. A high voltage has to be applied across the

anode and cathode to speed up the motion of electrons from the cathode towards the anode. When the electrons reach the anode a small portion of their kinetic energy is converted to X-rays and the remaining larger portion is transformed to heat. As a result, there will be more heat in the X-ray tube, and the tube need to be cooled by placing it in a coolant.

In this project the Bruker D8 Advance X-ray diffractometer was used to study the structural properties of the CZTS and In_2S_3 thin films. The machine was equipped with CuK_α radiation having a wavelength of 0.154056 nm. The current and voltage of the X-ray diffractometer was set to 40 mA and 40 kV, respectively. Figure 28 depicts a diagram of Bruker D8 Advance X-ray diffractometer.



Figure 28: Bruker D8 Advance diffractometer

X-rays are electromagnetic waves with short range of wavelengths (0.01 nm – 10 nm). This range of wavelengths is almost the same as the spacing between atoms in most solid materials. Due to short wavelength, X-rays are very penetrative and are suitable to be used

for study the structural properties of materials. A beam of X-rays penetrating a crystal will be dispersed in different directions by the atoms in a crystal, when the beam is dispersed in a specular fashion (Bragg diffraction) as shown in Figure 29, constructive interference will take place.

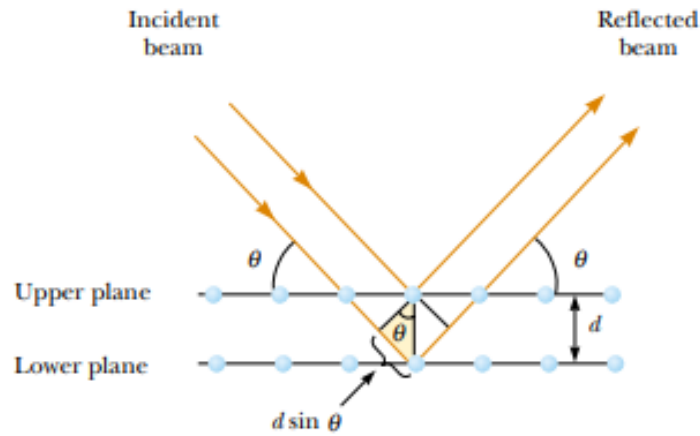


Figure 29: Bragg's scattering [119].

According to Bragg's law the dispersed beam will only interfere constructively if the path difference between the X-rays scattered by the planes is a multiple of the wavelength. Mathematically, Bragg's law can be expressed as shown in equation (14)[120]:

$$n\lambda = 2d_{hkl}\sin\theta \quad (14)$$

In the above equation, n is the order of diffraction and the value of n is always an integer. Other variables like λ , d and θ refers to the wavelength of incident X-ray beam, path difference and incident angle.

Solid materials can exist in two forms being amorphous and crystalline. The examples of an amorphous and crystalline solid materials glass and copper metal, respectively. In amorphous solid materials, atoms are not arranged in order while in crystalline solids atoms are arranged in a regular pattern. Most solids exist in crystalline form. There seven examples of crystal systems namely cubic, tetragonal, hexagonal, orthorhombic, monoclinic and triclinic.

3.7.2 Raman Spectroscopy

Raman spectroscopy is a technique that employs light scattering phenomenon to obtain the chemical and structural properties of the samples. This technique was named in honour of C.V. Raman who discovered Raman scattering in 1928. The radiation incident upon the

sample always scatters in different directions due to the vibrations of molecules within the sample. During this process more radiation scatter with the same wavelength as of the incident radiation, this is called Rayleigh (elastic) scattering. In addition, less radiation scatter at wavelengths greater or smaller than that of the incident radiation and this is known as Raman (inelastic) scattering. The occurrence of Raman scattering is determined by wavelength of the incident radiation.

An instrument that is used in Raman spectroscopy is known as Raman spectrometer. Most Raman spectrometers consists of various excitation lasers. The structural and chemical information of a sample is extracted by illuminating it with a certain laser beam. The interaction between the beam and molecules from the sample creates scattered light. Only light that undergoes elastic scattering is used for modelling the Raman spectrum of the sample. A Raman spectrum is graph of intensity as a function of Raman shift. A Raman shift is defined as the difference between the energy of the incident radiation and scattered radiation. It is independent on the wavelength of the incident light. When the wavelength of the radiation incident upon the sample is smaller compared to the one of scattered radiation, stokes lines are seen on the spectrum. But when the wavelength of the radiation incident upon the sample is greater than the wavelength of scattered radiation, the anti-stokes lines are observed on the Raman spectra.

Most Raman spectrometers can record the Raman spectra from 10 cm^{-1} to $4\ 000\text{ cm}^{-1}$, however, this range can vary depending on the model and optical elements of the machine. In this study the LabRAM HR Evolution Raman spectrometer, shown in Figure 30, was used for further characterising the structure of the produced thin films. This spectrometer have three (325 nm, 532 nm and 785 nm) lasers, however, a 532 nm laser was used in this poject.

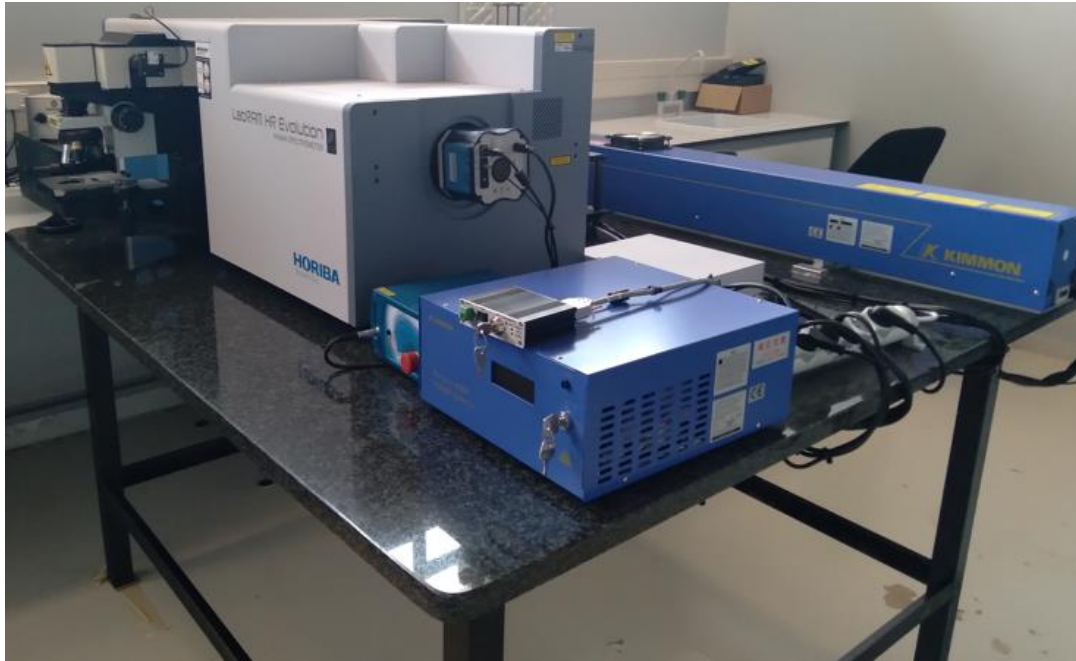


Figure 30: The LabRAM HR Evolution Raman spectrometer.

3.7.3 Stylus Profiler

A stylus profilometer is an instrument that is used to measure various parameters (roughness, texture, thickness, e.t.c) of thin films. This instrument has a metallic probe which scans over the surface of a sample. Next the process of measuring thickness of thin films with a stylus profilometer is described. The first step for measuring thickness involves making a step on sample by scratching with a thin metallic pin or etching by placing in a suitable solution like hydrochloric acid. Then the sample is placed on the sample stage just below the probe. After placing a sample with a step below the probe, the probe has to be lowered vertically downward until it comes into contact with the surface of a sample. The last step is to scan the surface. The scanning will give step profile on the screen of the computer, which is used for determination of thickness.

It is crucial to note that thickness is the height from the surface of the substrate to the surface of the thin film. Therefore, a step had to be made carefully without scratching deep into the substrate. In addition, the roughness of the sample may limit the accuracy of results from stylus profilometer as it adds more noise to the profile and as a result it may be difficult to locate the position of the step. Furthermore, the vibration of the profiler, which might be caused by the vibrations on the background, may also affect the results that are obtained. This can be minimised fitting suitable shock mountings and rigid supports.

The model of the profiler used in this project is KLA Tencor D-100 depicted in Figure 31. This profiler works by generating the analogue signal through the position of a stylus. The analogue signal will be converted to digital signal which can be stored and analysed.

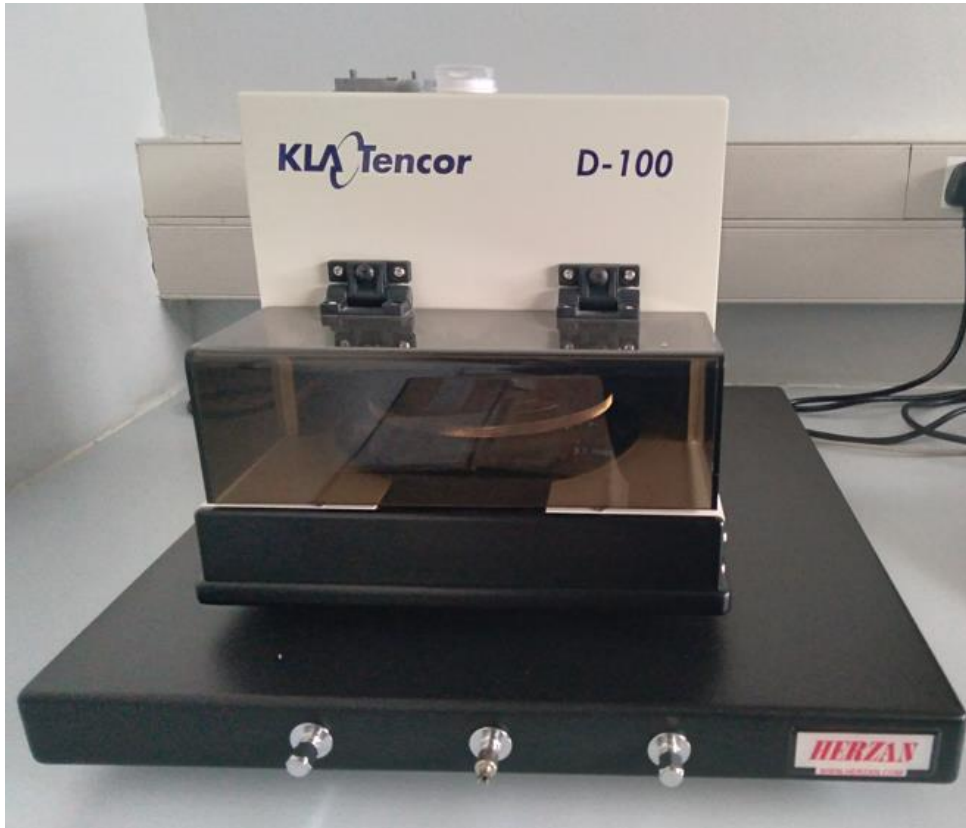


Figure 31: KLA Tencor D-100 profiler.

3.7.4 UV-Vis Spectroscopy

UV-Vis spectroscopy is a basic technique used to measure the amount of radiation (light) absorbed by various materials in the ultraviolet and visible regions of the electromagnetic spectrum. Any radiation incident upon the material may undergo absorption, reflection or transmission depending on the materials' properties such as thickness, surface texture and others. When a material absorbs sufficient amount radiation its molecules changes from the ground state to excited state, this process is known as excitation.

Most UV-Vis spectrometers consist of radiation source (usually xenon or mercury lamps), diffraction grater, half mirror and detectors. The diffraction grater splits the beam of light from the radiation source into its makeup wavelengths. A half mirror divides monochromatic beam from a diffraction grater into two beams with equal intensity. One beam is used for

reference and the other beam will pass through the material under investigation. The purpose of detectors is to measure the intensities of reference and sample beams. The results are usually presented as graphs (absorbance and transmittance spectra). A UV-Vis spectrum is a graph that shows how transmittance, absorbance or reflectance varies with wavelength. The wavelength is plotted on the x-axis and the dependent variable (transmittance, absorbance or reflectance) is plotted on the y-axis.

Absorbance (A) and transmittance (T) are related quantities. Transmittance is defined as the ratio of the intensity of a sample beam to the intensity of a reference beam. The value of transmittance is one if the material does not absorb any radiation. A mathematical expression of transmittance is given as follows[121]:

$$T = \frac{I}{I_0} \quad (15)$$

I denotes the intensity of light passing through the material and I_0 denotes the intensity of light incident upon the material.

Absorbance is the amount of radiation absorbed by a material and the value of absorbance is zero if the material does not absorb any radiation incident upon its surface. The absorbance can be expressed mathematically as[122]:

$$A = -\log T \quad (16)$$

Reflectance is another important optical quantity of materials. It is the measure of a small amount of incident radiation that bounces back at the surface of the material. Just like absorbance and transmittance, reflectance depends on the wavelength of the incident radiation. A mathematical equation that relates reflectance to absorbance and transmittance reads[123]:

$$T + R + A = 1 \quad (17)$$

The Perkin Elmer 750 UV/VIS/NIR spectrometer, shown in Figure 32, was used in this project to measure absorbance, transmittance and reflectance of the thin films. This spectrophotometer can measure optical quantities from 300 nm to 1100 nm.



Figure 32: The Perkin Elmer 750 UV/VIS/NIR spectrometer.

3.7.5 Hall Measurement

Hall Effect measurement is one of the most common methods used for studying the electrical properties of semiconductors. Typical Hall Effect Measurement systems consists of vacuum chambers, magnets, current source and others. The vacuum chambers in these systems allows for measurements to be taken under defined conditions. The Hall Effect measurement systems employs the Hall Effect in which electric field set up and magnetic field, applied on the semiconductor material (sample), is used to obtain information about the charge carriers (electrons and holes) found in it. When working with a Hall Effect measurement system, it is important to ensure that the distance between current contacts and voltage contacts are fairly large.

In Hall measurements the magnetic field is applied perpendicular to the sample and voltage is applied across the sample. The applied voltage creates an electric field which is perpendicular to the magnetic field and this causes current to flow. The charge carriers in a semiconductor with current flowing perpendicular to the magnetic field are deflected due to the Lorentz force. This induces a voltage (Hall voltage). Polarity of the Hall voltage is determined by the charge on the carrier. The size of Hall voltage is influenced by several parameters such as magnetic field strength, current and charge density. Several electrical parameters of semiconductor materials such Hall coefficient, resistivity, mobility, charge carrier

concentration and many more can be obtained by the Hall Effect measurement systems. The type of conductivity of a semiconductor material is determined by the Hall coefficient. The positive and negative signs on the Hall coefficients indicate that the semiconductor materials are p-type and n-type, respectively.

In this study ECOPIA HMS5500 Hall measurement system, shown in Figure 33, was used. It consists of two systems being AMP55T and AHT55T5, respectively. The AMP55T measures the parameters at room temperature and it was used to measure electrical parameters of CZTS and In_2S_3 thin films at room temperature. The AHT55T5 allows for measurement of electrical parameters at various temperatures.

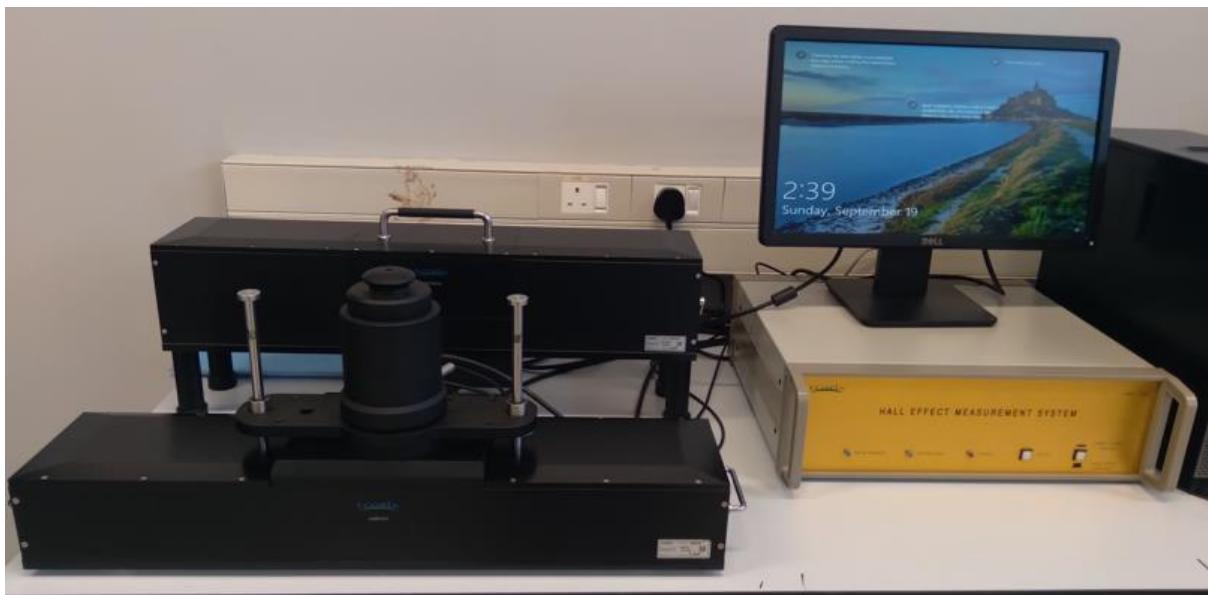


Figure 33: ECOPIA HMS5500 Hall measurement system.

3.7.6 Scanning Electron Microscopy

Scanning electron microscopy (SEM) is the most widely used technique for examining the morphology and microstructure of various materials. A SEM is one of the best tools for analysing particle size, because of its good resolution (about 10 nm). Even a resolution of 2.5 nm can be achieved with modern SEM devices. Some techniques like energy-dispersive X-ray spectroscopy (EDS) are used in conjunction with SEM for examining the elemental composition of the materials.

Some main components of SEM are sample stage, electron gun, electromagnetic lenses, apertures, vacuum system and detection system. The first step involved in characterization of materials with SEM is to mount the sample to the sample stage. Then a beam of electrons is

emitted from electron gun which is located at the top of the column. This beam is accelerated to higher energies ranging from 0.1 keV to 30 keV. This process requires a high vacuum environment to prevent scattering and absorption of electrons by air. The beam is shaped and directed to the sample surface when passing through the aperture and electromagnetic lenses. The interaction that takes place when the beam reaches and penetrates the sample results in ejection of electrons and photons from the surface of the sample. The emitted electrons and photons are collected in the detector system used to generate signals. Generated signals are used to produce images of the samples.

The EDS technique involves ionization of the atoms that make up the sample by focusing a beam of electrons towards the sample. This beam may knock off an electron from the inner shell in one of the atoms leaving a hole behind. When an electron from outer shell loses energy and fills the hole left behind in the inner shell, energy is emitted in form of an X-ray. The emitted X-ray is specific for every element and it is used to analyse elemental composition of the sample with the energy dispersive detector.

The MERLIN ZEISS GEMINI SEM, shown in Figure 34, was used in this work to study the morphology of the CZTS thin films. This machine had EBSD system and EDS detector installed. Therefore, EDS detector was also used for analysing the composition of the CZTS films.

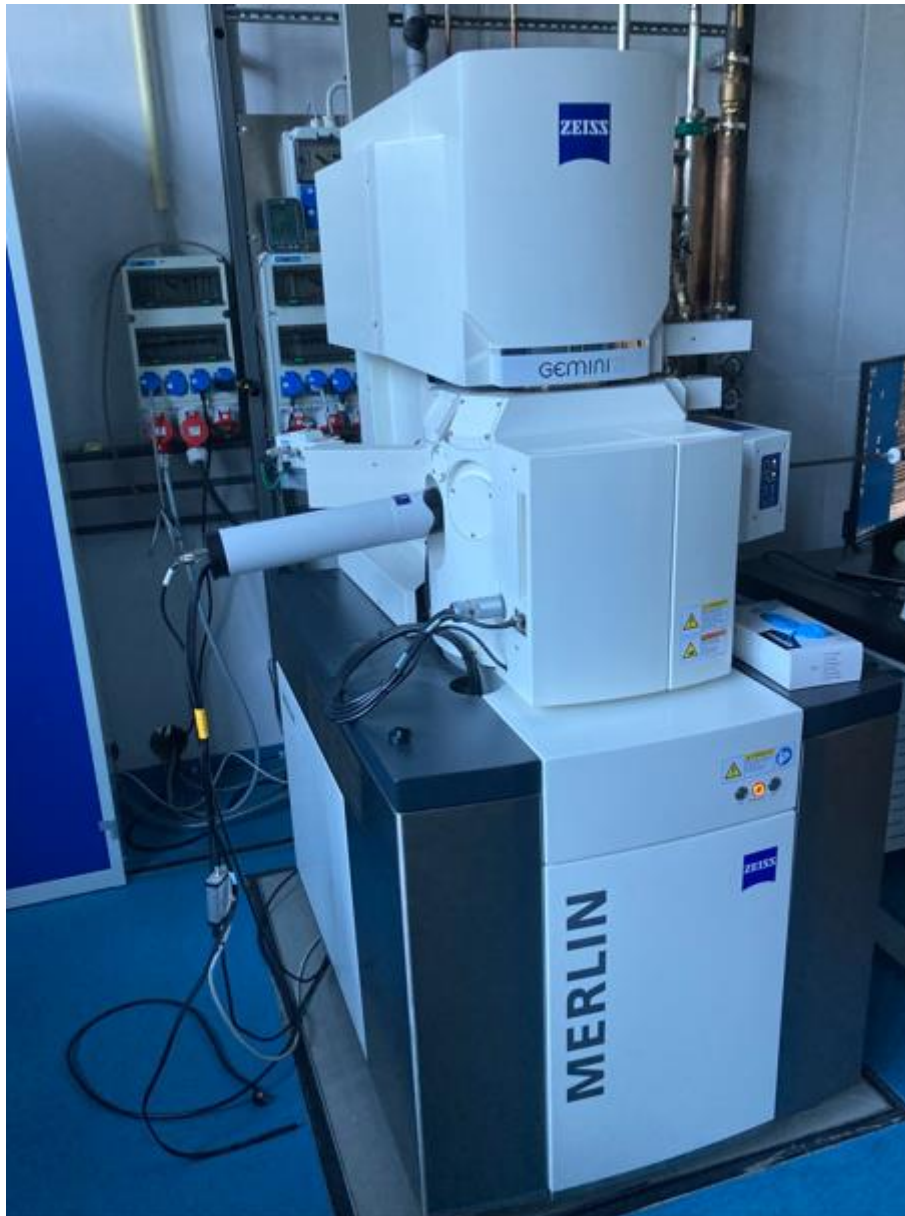


Figure 34: The MERLIN ZEISS GEMINI SEM.

3.7.7 Atomic Force Microscopy (AFM)

Atomic force microscopy is a high resolution (the order of nanometre) method developed in 1985 by Binnig and his fellow workers. This method can be used for analysing the surface of the sample. Various properties of the sample such as topography, chemical, electrical and mechanical properties can be obtained through this technique.

The atomic force microscope consists of laser beam, cantilever, photo sensitive diode, piezoelectric scanner and many more. A sharp tip (usually made from silicon) at one end of the cantilever is used to scan over the surface of a sample. Prior to scanning a sample surface,

the tip is brought closer to the sample surface. The assembly of cantilever and tip is known as a probe. Its lateral and vertical position of the probe with respect to the sample surface is controlled by a piezoelectric scanner. During scanning the cantilever is deflected due to changing topography on the sample surface and the deflection of the cantilever is traced through a laser beam that bounces on the back of the cantilever. The reflected beam is gathered by a photo sensitive diode and directed towards a detector and feedback system. Figure 35 shows the basic components involved in atomic force microscopy. The points obtained during scanning with the tip are combined and used to produce a three-dimensional image of the sample surface.

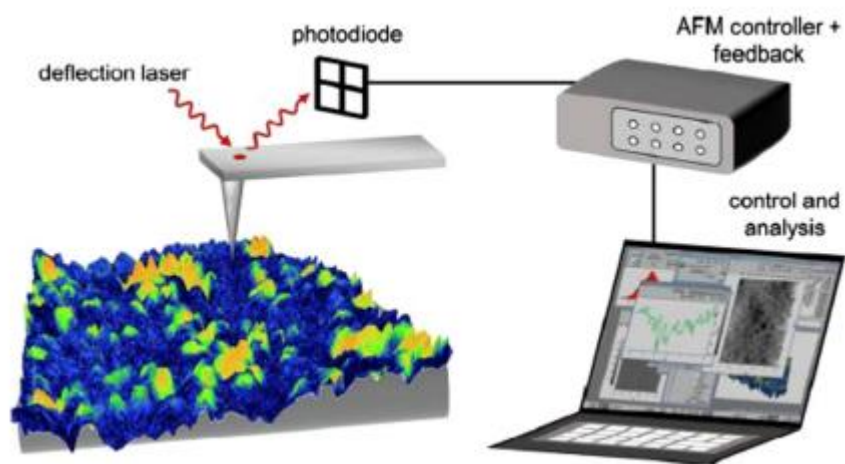


Figure 35: Basic components of atomic force microscopy[124].

An atomic force microscope can operate under various modes, however, there are only two imaging modes namely static and dynamic modes. In a static mode, the sample surface is scanned with a probe having a constant contact between the tip and sample surface. The dynamic mode involves scanning a sample surface using the probe oscillating or vibrating at a certain frequency. This mode is better than the contact mode, because it can scan a sample gently. When characterising samples with atomic force microscope it is important to keep sufficient distance between the sample and tip as the continuous interaction force between the sample and tip may damage the sample.

The BRUKER atomic force microscope, shown in Figure 36, was used in this work to study the morphology of In_2S_3 thin films. This microscope has a resolution to the order of nanometre.



Figure 36: The BRUKER Atomic Force Microscope.

3.8 Studying the performance of the cell

The performance (the dark and illuminated I-V curve) of the solar cell prototypes was studied under the standard test conditions by using a solar simulator in conjunction with the Keithley 4200A parameter analyser, a solar simulator provides a solar irradiation of 100mW per cm^2 by keeping the solar cell temperature at 25°C for testing the produced solar cell prototypes. In this research a low-cost and simple SciSun-150 solar simulator, shown in Figure 37, was used for illumination of the solar cell prototypes. This solar simulator falls under the class AAA and its maximum power is 150 W. The SciSun solar simulators can provide maximum illumination of about two suns. Most of the SciSun models from Sciencetech consist of: xenon lamp, filter holder, arc lamp housing with an integrated igniter, beam tuner and quality control report. The different filters used the SciSun solar simulators are found in the filter holder and the level of output irradiance can be varied using a variable aperture.



Figure 37: The SciSun-150 solar simulator.

When SciSun solar simulators are used with suitable air mass filters, they can perform measurement of class A spectral match. The results vary according the model of solar simulator used. Figure 38 shows the results obtained from the SciSun solar simulator using the AM1.5G filter. Moreover, the SciSun simulators can meet both class A spatial non-uniformity and class A temporal instability. Class A spatial non-uniformity is usually achieved on a default mode. In addition, class B spectral match which is required for larger target sizes may also be available on these simulators by request.

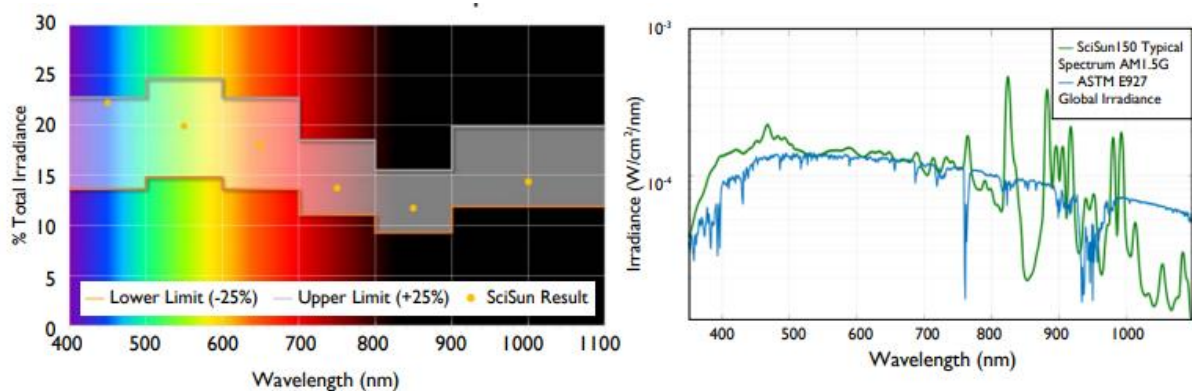
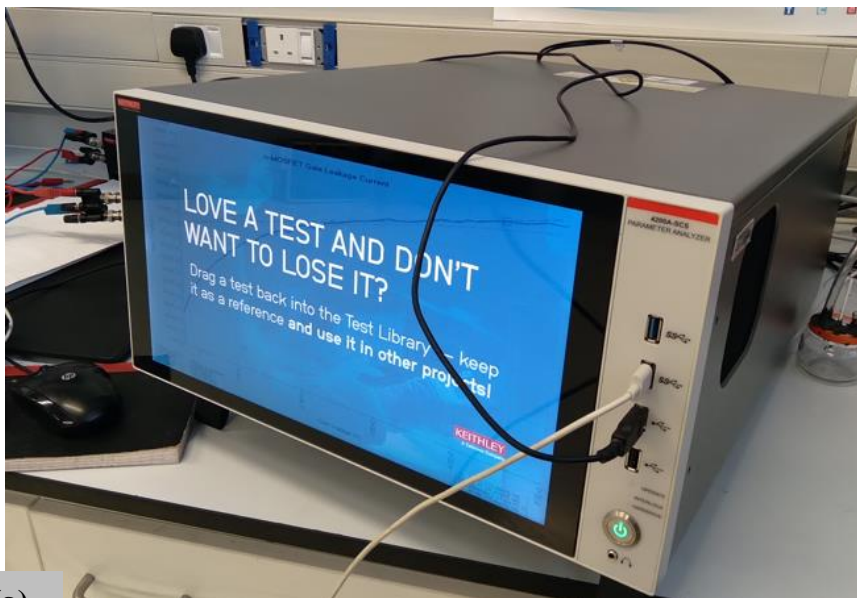


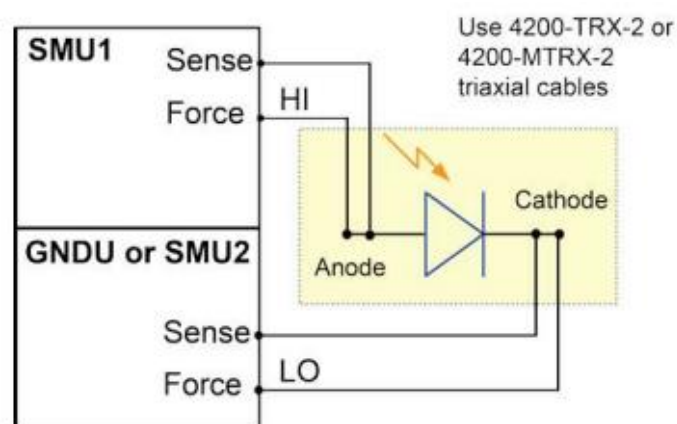
Figure 38: The spectral Match obtained from SciSun-150 solar simulator[125].

The Keithley 4200A parameter analyzer is used in conjunction with a solar simulator to measure voltage variation on a forward biased solar cell connected in a four wire configuration, while the current flowing through the solar cell is also measured at every step.

The data obtained are then used to produce a graph of current as a function of voltage (I-V curve). Various parameters about the solar cell such as open circuit voltage, short circuit current, maximum power and others can be determined from the obtained I-V curve. Additional materials required when performing measurement on a solar cell when using Keithley are four triaxial cables and two SMUs (Source Measurement units). In this work, the Keithley 4200A-SCS parameter analyzer shown in Figure 39 (a) was used for performing measurements by using the Clarius 1.9 software. The best method for performing measurements on the cell is to connect the output terminals of the SMUs to the solar cell in a 4-wire configuration. This method helps to reduce resistance due to the test leads and unwanted potential drops. Figure 39 (b) shows the schematic connection of the solar cell to the one SMU and the ground unit (GNDU), which is a built-in SMU of the Keithley 4200A.



(a)



(b)

Figure 39: (a) The Keithley 4200A-SCS parameter analyzer and (b) schematic connection of the solar cell to one SMU and GNDU[126].

In this work, the current-voltage curves for the photo conductivity measurements were obtained in the dark and under illumination. Just like for photo conductivity measurements, the current-voltage characteristics for the solar cells were measured in the dark and under illumination conditions. Figure 40 shows a biased solar cell. The positive terminal of a cell was connected to SMU1 and negative terminal of a cell was connected to GNDU. All current-voltage curves were obtained by biasing the devices as shown in Figure 40. The bias voltage for photo conductivity measurements was ranging from -4 V to 4 V and the solar cells were biased from 0 V to 8 V. Under illumination conditions, a solar simulator was used for testing the solar cell prototypes under illumination by applying a solar irradiation of 100 mW/m². All measurements were performed under air mass (AM) of 1.5 G. Finally, the current-voltage characteristics were obtained and stored on the Keithley 4200A-SCS parameter analyser by using the Clarius software.

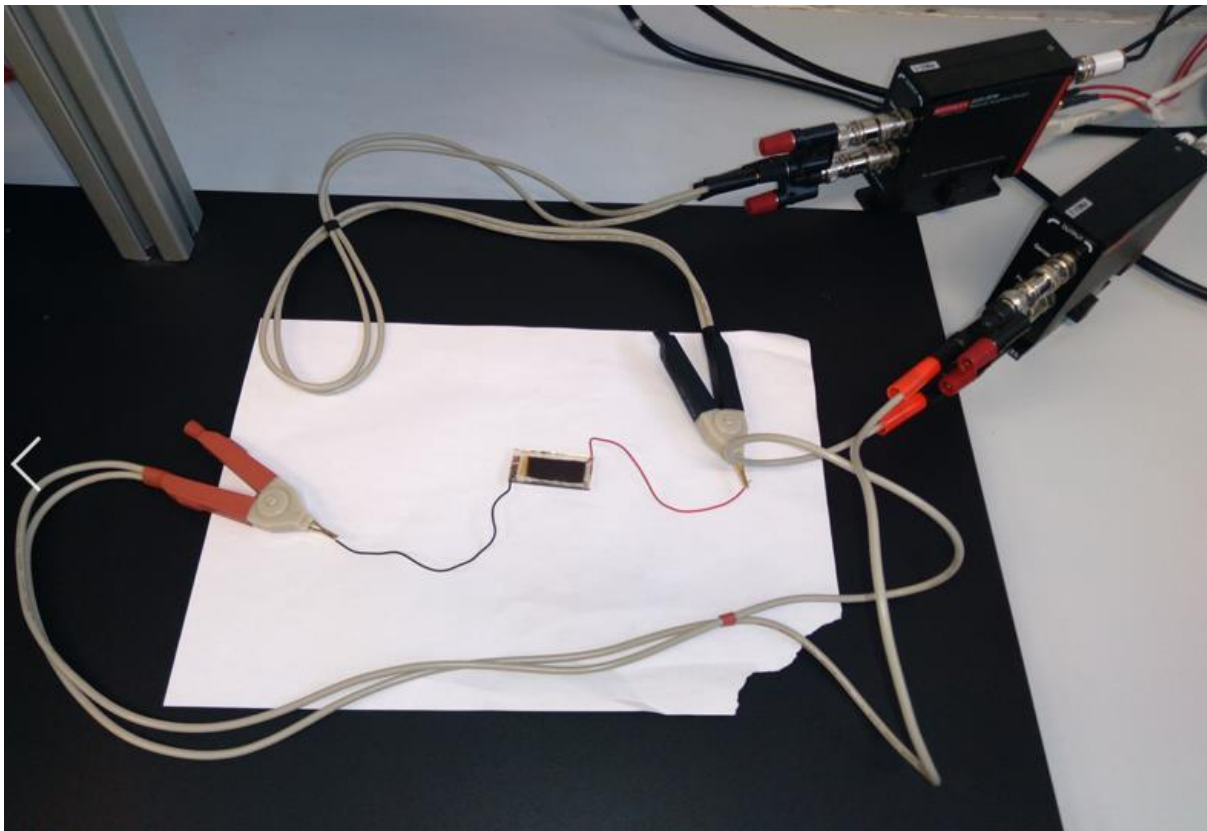


Figure 40: A circuit for finding the I-V curve of a cell.

CHAPTER 4 RESULTS AND DISCUSSION

4.1 Characterisation of CZTS thin films

4.1.1 Structural Characterization of CZTS thin films

4.1.1.1 X-Ray Diffraction Studies

X-Ray diffraction was used to study the crystallinity and identify the presence of the CZTS phases in the films. Figure 41 presents the obtained diffractograms of the CZTS samples. The X-Ray diffraction patterns revealed three phases which match with the (1 1 2), (2 2 0) and (3 1 2) crystallographic planes of the kesterite CZTS in a tetragonal lattice structure (PDF 00-026-0575 Cu₂ Zn Sn S₄ K_λsterite, syn). However, there is an extra peak at 2θ (equal to 46.4°), which is associated with Cu_xS and it most visible for samples (CZTS003 and CZTS004, see Figure 41) prepared using tin (IV) chloride solution as one of the components of the precursor. This peak might be caused by high amount of Cu in the samples[127]. All samples were growing along the (1 1 2) direction. The crystallinity of the samples prepared using tin (IV) chloride as a source of tin is higher than those of samples prepared using tin (II) chloride as proved by the intensity of the (1 1 2) peak in Figure 41. This shows that the precursor solution plays a crucial role on the structural properties of CZTS films, however, changing the zinc sources does not show a significant change in the crystallinity of the samples. These findings agree with results published recently. Khalate et al [128] obtained similar XRD patterns from the CZTS films deposited by chemical spray pyrolysis technique at various substrate temperatures. Chtouki et al [129] also reported similar diffractograms of the CZTS thin films grown by spin-coating and spray pyrolysis.

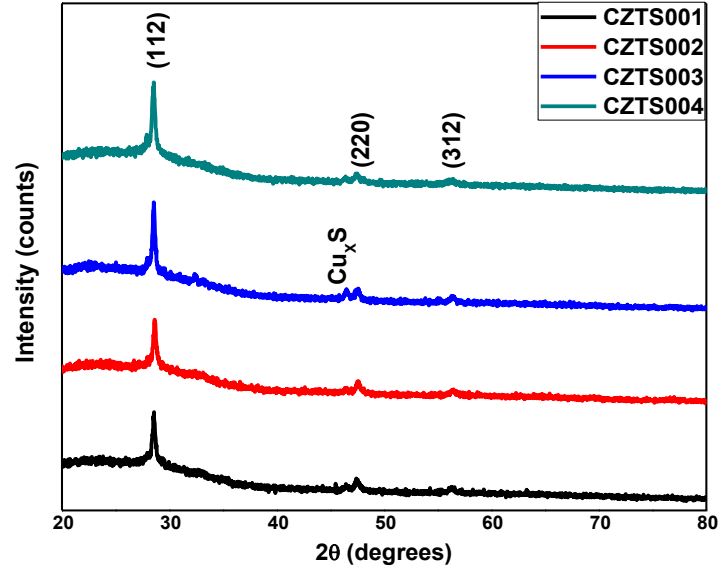


Figure 41: X-Ray diffraction patterns of the CZTS samples.

The crystallite size (D), dislocation density (δ) and the lattice parameters of the samples were calculated using equations (18)[130], (19)[131], and (20)[132]. In equation (18) the parameters λ , β and θ refers to the wavelength of the X-Ray, full width at half maximum and Bragg's angle, respectively. The parameters of dominant peak were used for calculating the crystallite size in all samples. The d in equation (20) is the inter planner spacing, the h , k and l represent the values of a miller index labelling the plane by the expression ($h k l$).

$$D = \frac{0.9\lambda}{\beta \cos(\theta)} \quad (18)$$

$$\delta = \frac{1}{D^2} \quad (19)$$

$$\frac{1}{d^2} = \frac{h^2+k^2}{a^2} + \frac{l^2}{c^2} \quad (20)$$

Table 3 shows the values of the crystallite sizes, dislocation densities, and lattice parameters for all CZTS thin films. As shown in table 2 crystallite sizes ranges from 29.36 nm to 38.52 nm. Remarkable, CZTS003 has the highest crystallite size. The crystallite size depend on the full width at half maximum of the dominant peak, the dominant (1 1 2) peak was narrow for CZTS003 and broad for CZTS004. This shows that highly crystalline CZTS thin films can be achieved by varying the precursor solution. Moreover, CZTS003 has the lowest value of dislocation density and this also indicates that CZTS003 has the best crystalline structure.

The obtained values of lattice parameters (a and c) are in agreement with other values reported in literature. The reported theoretical values of a and c are 5.427 Å and 10.848 Å [133], respectively. Note that the small difference observed in values of lattice constants may be due to slight shift of the peaks.

Table 3: Values of crystallite sizes, dislocation densities and lattice parameters for CZTS samples.

Sample name	Crystallite size (nm)	Dislocation density x 10^{14} (1/m ²)	a (Å)	c (Å)
CZTS001	34.79	8.262	5.422	10.847
CZTS002	30.58	10.800	5.402	10.846
CZTS003	38.52	6.740	5.408	10.847
CZTS004	29.36	11.600	5.414	10.487

4.1.1.2 Raman results

The XRD analysis does not prove the purity of the CZTS samples as some secondary phases (such as SnS₂) with similar XRD pattern as CZTS might be formed during the preparation of the CZTS samples. To avoid the misinterpretation of the results, the Raman spectroscopy technique was used to study further the purity of CZTS samples. Figure 42 shows the Raman spectra of all the spray deposited CZTS samples. All samples exhibit two wide peaks at around 248 and 331 cm⁻¹. The dominant peak at 331 cm⁻¹ belongs to a kesterite CZTS with a symmetry [134], while the small peak at 248 cm⁻¹ is associated with kesterite having B symmetry [135]. There is also a blue-shift of the dominant peak from the theoretically calculated value (338 cm⁻¹) to 331 cm⁻¹. This shifting might be caused due to the presence of internal stresses in the films and shrinking of the substrate during cooling of the samples [136]. Valdes et al [137] obtained similar results (dominant peak at 332 cm⁻¹) on the films deposited by spray pyrolysis. Two samples (CZTS003 and CZTS004) have good crystallinity and the crystallinity is higher for CZTS003 as in XRD results.

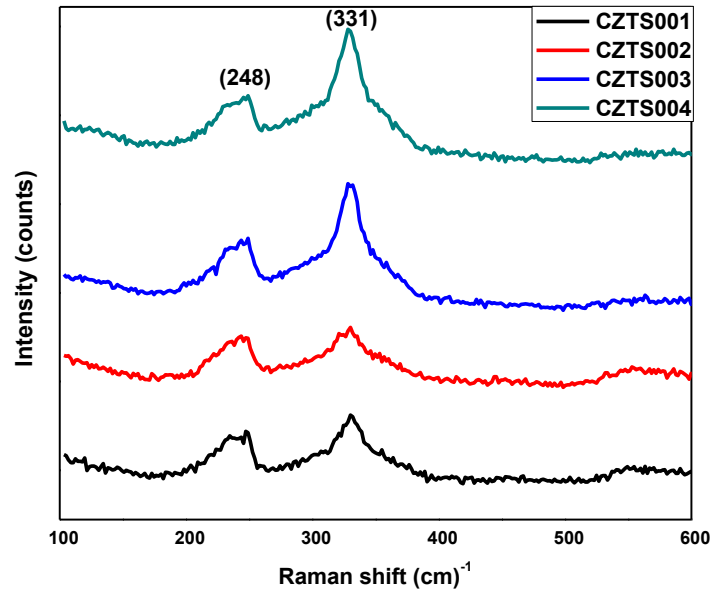


Figure 42: Raman spectra of the CZTS thin films.

4.1.2 Thickness measurements

Various properties (structural, optical and electrical) of thin films are influenced by their thickness. Thickness of thin films can be measured through optical and mechanical methods. In this work the thickness of the CZTS thin films was determined through mechanical method using an instrument called stylus profilometer and the results are summarised in table 4.

As shown in table 4, the values of thickness obtained for all CZTS thin films are between 1 370 nm and 2 545 nm. There is a huge difference in the values of thickness obtained for different CZTS thin films and this huge difference clearly indicates the pivotal role played by different precursors that were used for preparing CZTS thin films. However, most of the values of thickness achieved are in agreement with the required range of thickness (1 000 nm – 2 000 nm) [138] for the CZTS absorber layer in a CZTS solar cell. There is only one sample (CZTS004) with the thickness greater 2 000 nm.

Table 4: Thickness of the CZTS thin films.

Sample name	Thickness (nm)
CZTS001	1 932.05
CZTS002	1 374.07
CZTS003	1 779.63
CZTS004	2 542.73

4.1.3 Optical studies of CZTS samples

4.1.3.1 Absorbance and Reflectance

The absorbance and reflectance spectra of the CZTS samples have been measured from 400 nm to 1100 nm using UV-Vis spectrometer. Figure 43 (a) shows the absorbance spectra of the CZTS samples. The absorbance spectra for the samples CZTS001, CZTS002 and CZTS004 exhibit higher absorbance in the visible region compared to CZTS003. This shows that using the different precursors to deposit the CZTS thin films have an impact on the optical properties of the obtained films, the absorbance of the obtained films is dependent on their composition. The maximum absorbance of CZTS001, CZTS002 and CZTS004 in the visible region of the spectrum ranges from 2.8 to 3.2. The CZTS003 sample has the lowest absorbance of around 1.8. All samples have a good absorbance compared to the findings in the literature. For example, Islam et al [139] obtained the maximum absorbance of 0.9299 and 0.8571 for two CZTS thin films prepared by the spin coating technique.

Figure 43 (b) shows the optical reflectance spectra of the CZTS samples. All samples show a reflectance lower than 15 % in the visible region and 20 % near the infrared region. The samples CZTS003 and CZTS004 have higher reflectance than the samples CZTS001 and CZTS002. We found that the sample CZTS003 reveals the highest reflectance in both the visible and the infrared region. Based on the results for the reflectance in the visible regions, we conclude that all samples (CZTS001 – CZTS004) are in principle suitable to be used as absorbers for solar cells.

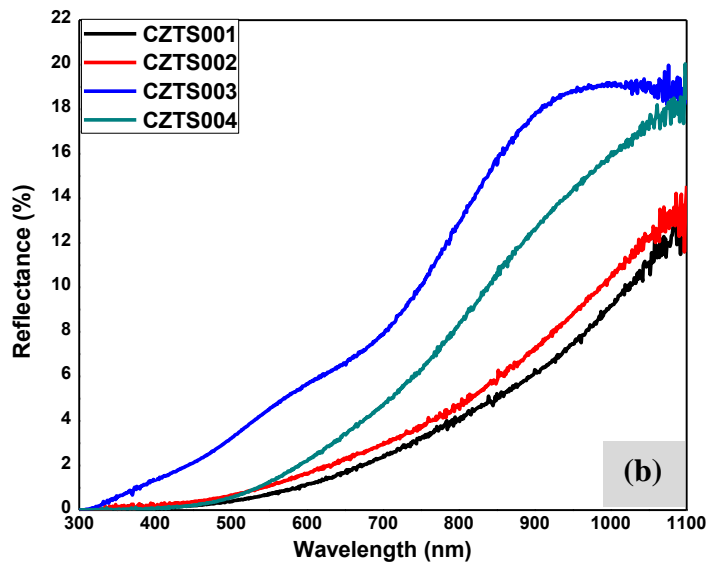
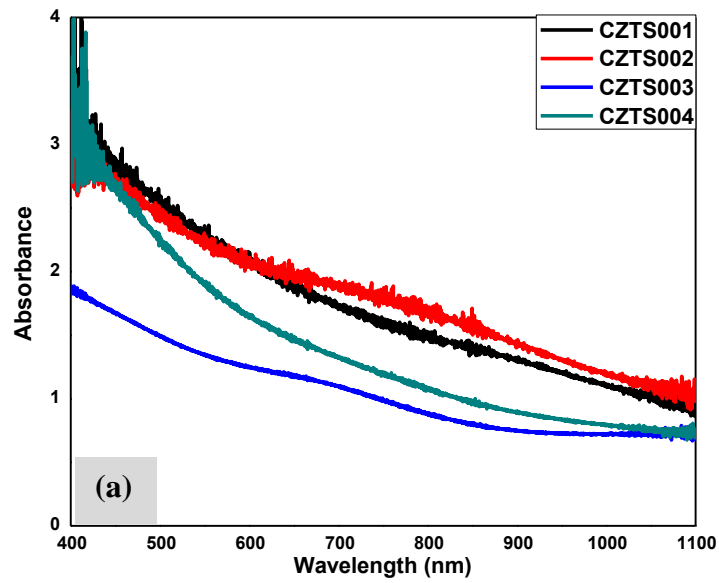


Figure 43: (a) Absorbance and (b) Reflectance of the CZTS thin films.

4.1.3.2 Absorption coefficient and Band gap

Absorption coefficient (α) and optical band gap (E_g) are very important optical parameters that helps to determine the material's suitability for certain applications. In case of an absorber the absorption coefficient must high and band gap should be narrow (approximately

1.5eV). In this work the absorption coefficient of the CZTS thin films was calculated from the absorbance data using the relation given in equation (21) [140], where A and d denote the absorbance and the thickness of the films, respectively. Furthermore, the band gap of the films was determined using the tauc's relation shown by equation (22) [141], here $h\nu$ represent the energy of the incident photon, k is a constant of proportionality, and E_g denotes the optical band gap of the material

$$\alpha = \frac{2.303A}{d} \quad (21)$$

$$(\alpha h\nu)^2 = k(h\nu - E_g) \quad (22)$$

Figure 44 shows the graphs that describe the relationship between absorption coefficient and photon energy for all CZTS samples. All samples have absorption coefficients ranging from 10^5 cm^{-1} to 10^6 cm^{-1} in the visible and near infrared region, which is greater than the theoretical value of 10^4 cm^{-1} . This obtained absorption coefficients are close to those reported in literature. Thiruvankadam et al [142] reported spray deposited thick CZTS thin films with absorption coefficient values of order 6. Moreover, it was also observed that the samples CZTS001 and CZTS002 have higher values of absorption coefficients compared to the samples, CZTS003 and CZTS004. The higher absorption coefficients found make all obtained layers to be suitable absorber layers because a good absorber must have a large value of the absorption coefficient as mentioned earlier.

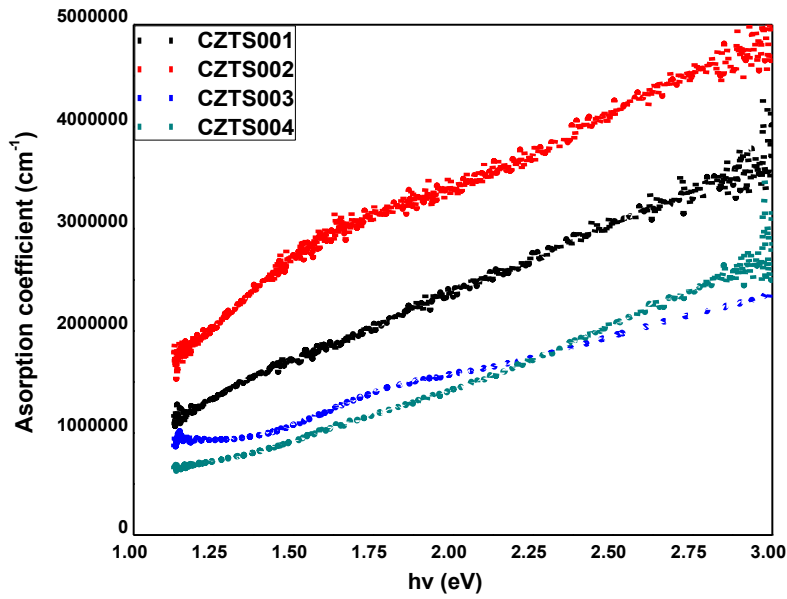


Figure 44: Absorption coefficient (α) for the CZTS thin films.

The tauc's plots were used to estimate the band gaps of all CZTS thin films (CZTS001-CZTS004), Figure 45 presents the tauc's plots of all samples. Optical band gaps were found by extending the linear portions of the curves towards the photon energy axes as shown on the Figure 45. The intersection of the extrapolated line and the horizontal energy axes gives the optical band gap. The band gaps of the CZTS samples ranges from 1.75 eV to 2.0 eV. These values are closer to the theoretically calculated band gap of CZTS (1.5 eV) and similar to other band gap values obtained in literature. Vanalakar et al [143] reported the pulsed prepared CZTS thin films with band gap values ranging from 1.53 eV to 1.83 eV before and after annealing. Note that the larger values of the band gaps (greater than 1.5 eV) might be attributed to quantum confinement effects caused by very small particles that make these films [144]. CZTS003 has smaller optical band gaps of 1.78 eV compared to CZTS001, CZTS002 and CZTS004. This difference in optical band gaps of the samples indicates that the precursor solution plays a pivotal role on the optical properties of the CZTS thin films.

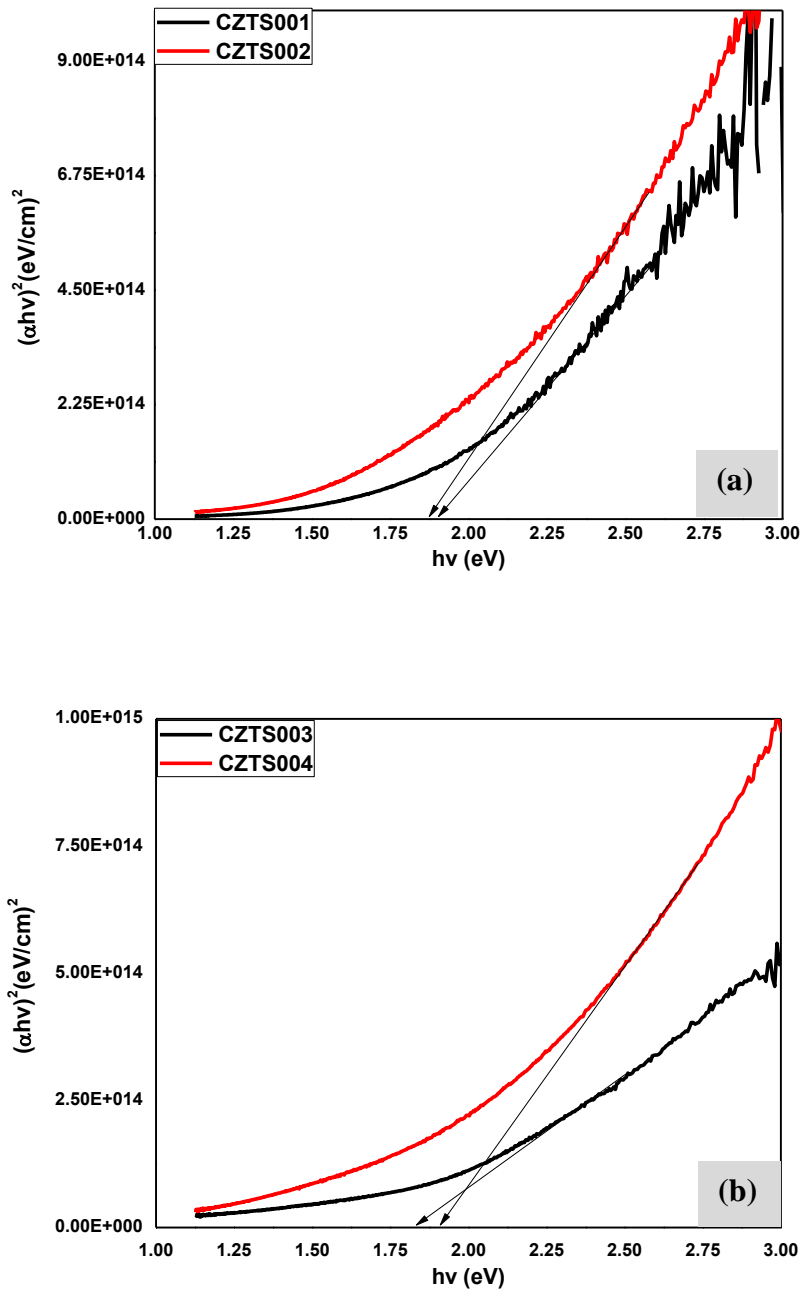


Figure 45: Tauc's plots for the CZTS samples prepared from solutions containing (a) SnCl₂ and (b) SnCl₄.

4.1.4 Electrical properties

The electrical properties are very important for choosing the best absorber layers for solar cells. In this research the Hall Effect method was employed to study the electrical parameters (bulk concentration, resistivity, mobility, and average Hall coefficient) of the CZTS samples at room temperature. Table 5 shows a summary of electrical parameters for all CZTS

samples. While the bulk concentration of the samples CZTS001, CZTS002, and CZTS004 is of order 10^{19} cm^{-3} , the bulk concentration of sample CZTS003 is of order 10^{20} cm^{-3} . Just like the bulk concentration results, the order of the resistivity of three of the four CZTS samples was the same ($10^{-1} \text{ } \Omega\text{cm}$), however, CZTS003 had the lowest resistivity which was of order $10^{-2} \text{ } \Omega\text{cm}$. Conductivity is inversely related to resistivity. This means that semi-conductor materials with smaller values of resistivity will have larger values of conductivity and in this case a CZTS003 has the largest conductivity compared to the other samples. The values of mobility for the samples ranges from 0.74 to 2.04 cm^2/Vs . The values of the electrical parameters summarized in table 5 are in good agreement with the values reported in literature. Kodigal et al [145] achieved a carrier concentration to the order 10^{19} cm^{-3} from CZTS thin films deposited via chemical spray pyrolysis, and Tanaka et al [146] obtained resistivity values ranging from $10^{-3} \text{ } \Omega\text{cm}$ to $10^{-1} \text{ } \Omega\text{cm}$ from co-evaporated CZTS thin films. The variation of the bulk concentration, resistivity and mobility of the samples shows that precursor plays a vital role on the electrical parameters of the CZTS absorber layer. Moreover, the positive values of the average Hall coefficient, stated on table 5, indicate that all the samples exhibit p-type conductivity.

Table 5: The electrical parameters of the CZTS samples prepared from different precursor solutions

Name of the sample	Bulk concentration (cm^{-3})	Resistivity (Ω/cm)	Mobility (cm^2/Vs)	Average Hall Coefficient (cm^3/C)
CZTS001	1.22×10^{19}	2.50×10^{-1}	2.04	5.11×10^{-1}
CZTS002	2.52×10^{19}	1.86×10^{-1}	1.33	3.48×10^{-2}
CZTS003	1.80×10^{20}	2.84×10^{-2}	2.01	3.47×10^{-2}
CZTS004	2.56×10^{19}	3.29×10^{-1}	0.74	2.44×10^{-1}

4.1.5 Morphology

The Scanning electron microscope was used to study the morphology of the CZTS thin films. Figure 46 depicts the SEM micrographs of the films prepared from various precursor solutions. It was observed that most of the samples (CZTS001, CZTS002, and CZTS003) except CZTS004 exhibit well defined grains, while the sample CZTS004 shows a smeary appearance with some regions like islands. The grains observed on CZTS003 were larger compared to the grains observed on other three samples (CZTS001, CZTS002, and CZTS003). This clearly demonstrates again that the properties of the CZTS thin films can be

enhanced by varying the type of precursor solutions. Voids had been also observed in all films, which might be due to the S deficiency, and this voids can lead to poor performance of a solar cell [147]. Chalapathi et al [148] also reported CZTS thin films with a similar morphology having voids at the surface. The values of grain sizes obtained from all films lie between 1 μm and 2 μm . These values match with most of the values reported in literature. For example, Mahewar et al [149] reported the spray deposited CZTS thin films with an average grain size of 1.63 μm .

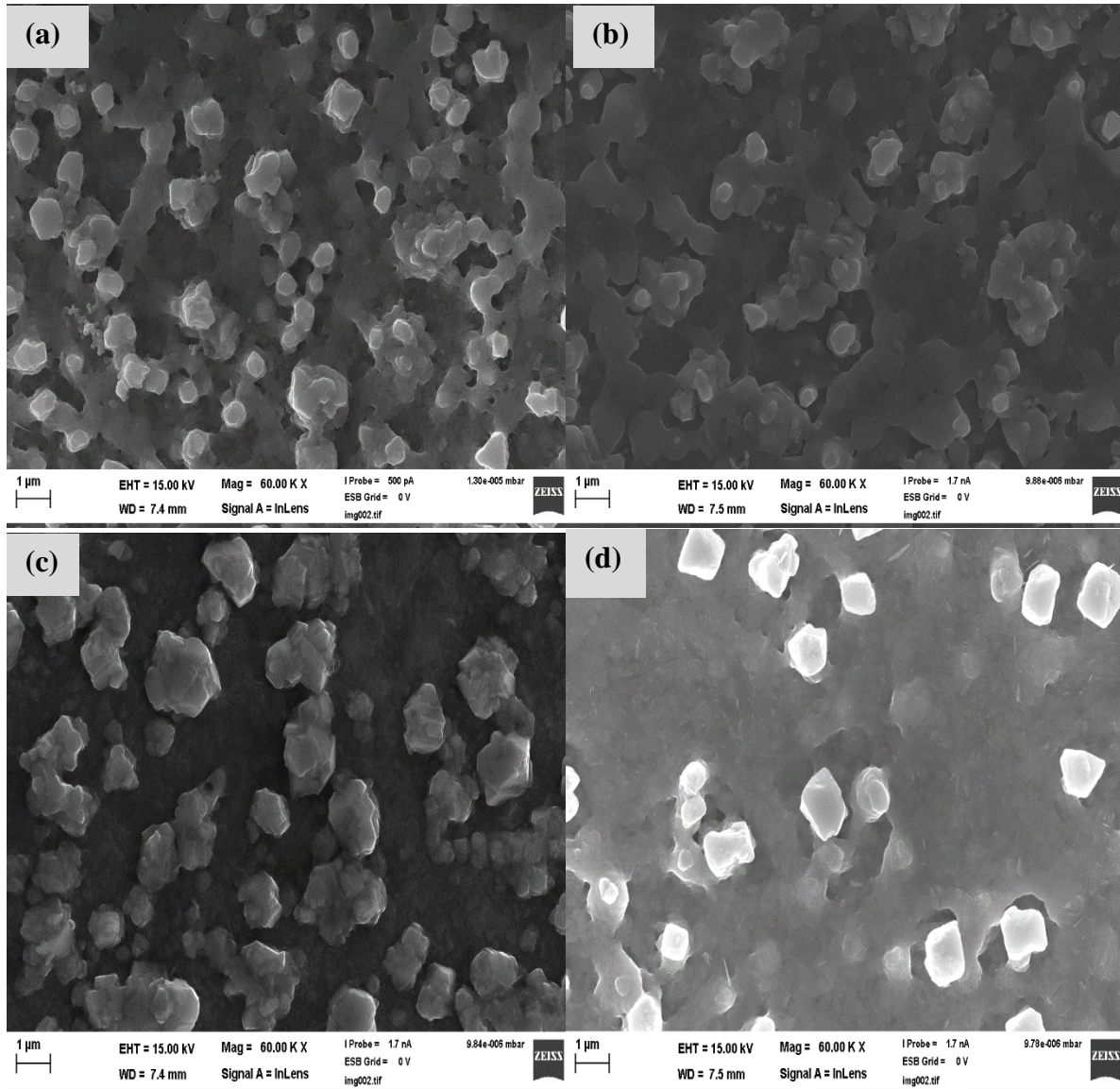
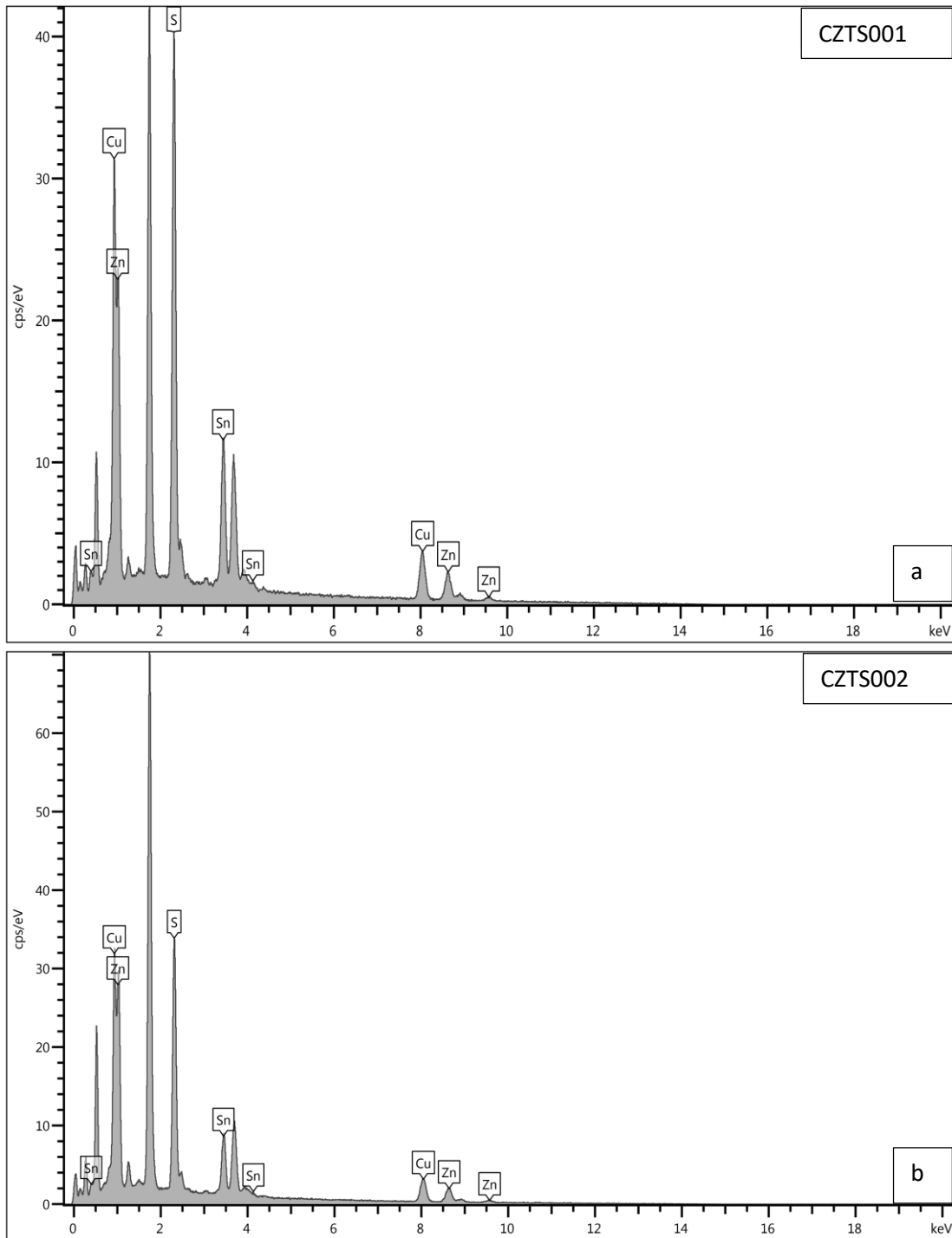


Figure 46: SEM images of (a) CZTS001, (b) CZTS002, (c) CZTS003, and (d) CZTS004 thin films.

4.1.6 Elemental composition

The elemental composition of the CZTS thin films was carried out using Energy Dispersive X-Ray technique. Figure 47 presents the EDX spectra of all samples as obtained from the machine.



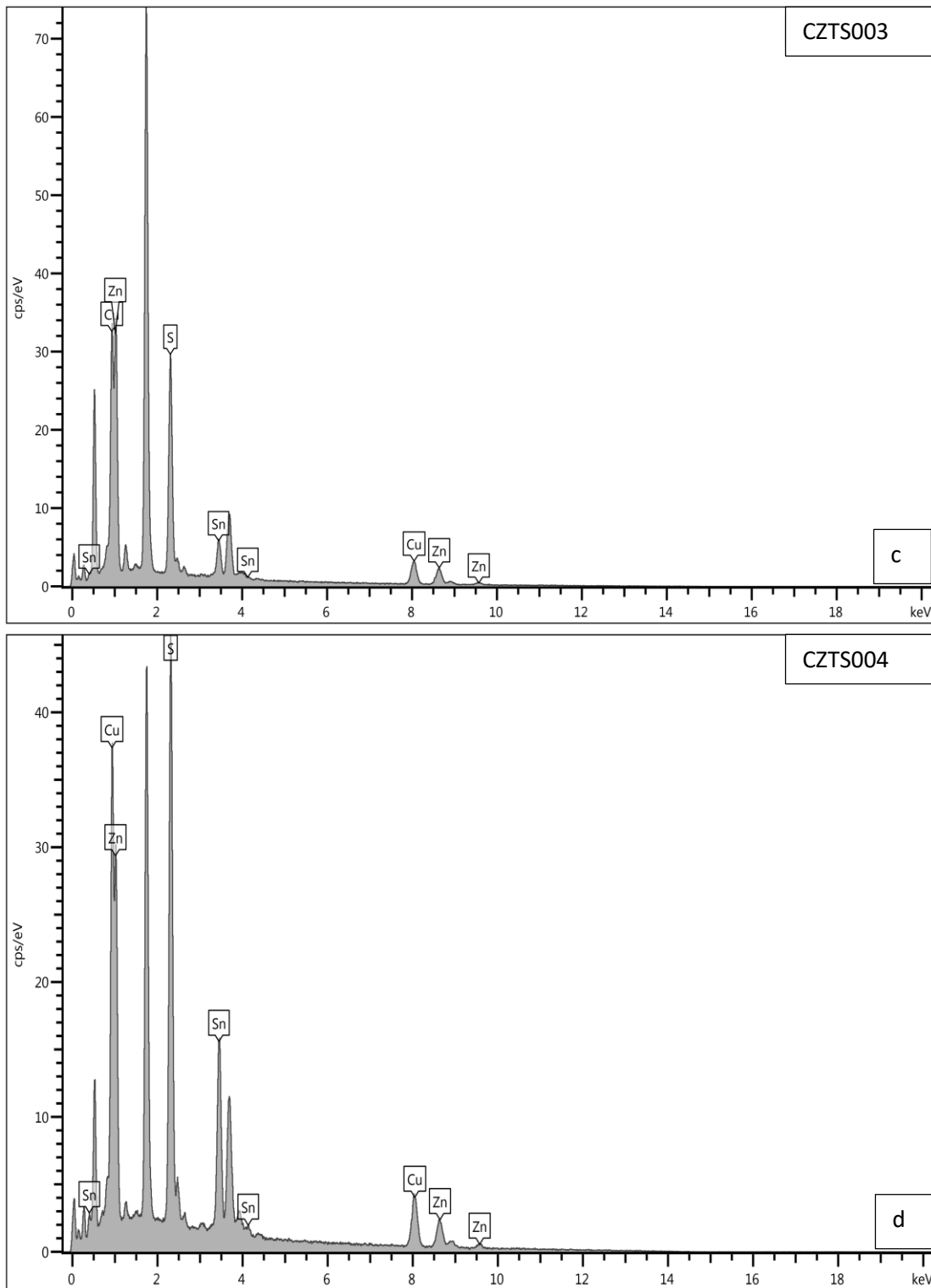


Figure 47: The EDX spectra of (a) CZTS001, (b) CZTS002, (c) CZTS003 and (d) CZTS004

All samples were scanned using three different spectrums and the results were averaged. The findings are summarized in table 6. As shown in Figure 47 and table 6 all CZTS samples reveal a large variation from stoichiometry. For a stoichiometric CZTS thin film the atomic

percentages of Cu, Zn, Sn and S are 25, 12.5, 12.5, and 50, respectively [150]. In addition, the Cu/ (Zn +Sn) and Zn/ Sn ratios are both equal to one. All CZTS thin films had higher amount of Cu ranging from 31.56 % to 37.29 %, which might be caused by the higher concentration of Cu in the used precursor solutions. These results agree with XRD results which showed that there might be a high amount of Cu in the sprayed samples. This is in agreement with previous findings, e.g., Arba et al [151] achieved a Cu proportion of 37.73 % and 37.92 % in CZTS thin films grown at 375 °C and 425 °C by spray pyrolysis method.

Moreover, our analysis also exhibited S deficiency. The lower amount of S might be due to evaporation of sulfur as the films were prepared at higher temperatures. Despite S deficiency, the results agree with other results reported in literature. Espindola – Rodriguez et al [152] reported CZTS thin films with a S content ranging from 32 % - 33 % before any treatment. From table 6, we can see that CZTS001 has the smallest Cu/ (Zn + Sn) ratio. This means that sample CZTS001 is Cu poor compared to the remaining three CZTS samples. On the other hand, CZTS003 had the highest amount of Zn/Sn ratio and its Cu/ (Zn + Sn) ratio was approximately equal to one. Thus, the sample CZTS003 is Zn rich.

Table 6: Elemental composition of the CZTS thin films.

Name of the sample	Cu (at. %)	Zn (at. %)	Sn (at. %)	S (at. %)	$\frac{Cu}{Zn + Sn}$	$\frac{Zn}{Sn}$
CZTS001	31.56	23.11	26.12	19.21	0.64	0.88
CZTS002	34.70	18.85	9.92	36.53	1.21	1.90
CZTS003	33.60	28.30	5.07	33.04	1.01	5.58
CZTS004	37.29	17.96	9.10	35.65	1.38	1.97

4.2 Characterisation of In₂S₃ thin films

4.2.1 Structural properties

4.2.1.1 XRD results

Figure 48 shows the XRD spectra of In₂S₃ thin films prepared by varying the concentration of thiourea. All samples exhibit three peaks at $2\theta = 27.5^\circ$, 33.3° and 43.7° matching with (1 0 9), (2 2 0) and (3 0 9) planes of β -In₂S₃, values of d obtained from these films match well with those in JCPDS data card (25 – 390). Jayakrishnan [153] obtained similar XRD patterns for the In₂S₃ thin films that were prepared using spray pyrolysis method. However, there is a weak peak found at $2\theta = 31.6^\circ$ on the pattern of the sample In₂S₃_0.90 which belongs to In₂O₃[154]. This might be caused by the low content of sulfur as the low concentration of

thiourea was used for preparation that sample. Some In might have reacted with oxygen from the surrounding during deposition forming In_2O_3 . The intensity of the dominant peak (2 2 0) decreased as the concentration of thiourea was increased. Sample $\text{In}_2\text{S}_3_{-0.090}$ had the highest intensity, while sample $\text{In}_2\text{S}_3_{-0.105}$ showed the lowest intensity (see Figure 48).

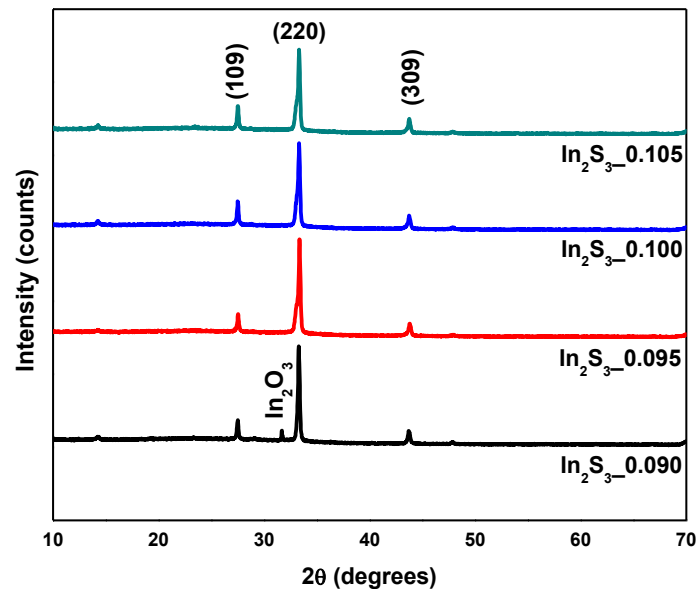


Figure 48: XRD spectra of In_2S_3 thin films.

Both the crystallite sizes and dislocation densities of all In_2S_3 samples were determined using equation (18) and equation (19), respectively. The results are summarised in table 7. As shown in table 7, when the concentration of thiourea was increased from 0.090 M to 0.100 M the crystallite size decreased and the dislocation density increased due broadening of the most intense (2 2 0) peak. However, if the concentration of thiourea was further increased to 0.105 M, the crystallite size increased, while the dislocation density decreased. The decreasing values of crystallite size and increasing values of dislocation density show that a high amount sulfur degrades the crystallinity of the In_2S_3 thin films.

Table 7: Values of crystallite sizes and dislocation densities of In_2S_3 thin films.

Sample name	Crystallite size (nm)	Dislocation density $\times 10^{14}$ ($1/\text{m}^2$)
$\text{In}_2\text{S}_3_{-0.090}$	46.89	4.55
$\text{In}_2\text{S}_3_{-0.095}$	46.01	4.72
$\text{In}_2\text{S}_3_{-0.100}$	41.63	5.77
$\text{In}_2\text{S}_3_{-0.105}$	43.46	5.30

4.2.1.2 Raman spectroscopy studies

The properties of the In_2S_3 thin films were further characterized through Raman spectroscopy to confirm the presence on In_2S_3 phases. Figure 49 shows the Raman spectra of the sprayed thin films. All samples exhibit similar patterns and have two peaks at 306 cm^{-1} and 365 cm^{-1} belonging $\beta\text{-In}_2\text{S}_3$. The peak at 306 cm^{-1} is associated with the vibration of InS_4 tetrahedra [155]. Just like in XRD results, the intensity decreased if the amount of S was increased, indicating that increasing the amount of S degrades the crystallinity of In_2S_3 thin films. A similar behaviour of decreasing crystallinity with increased S content was shown by S. Elfarras et al [156].

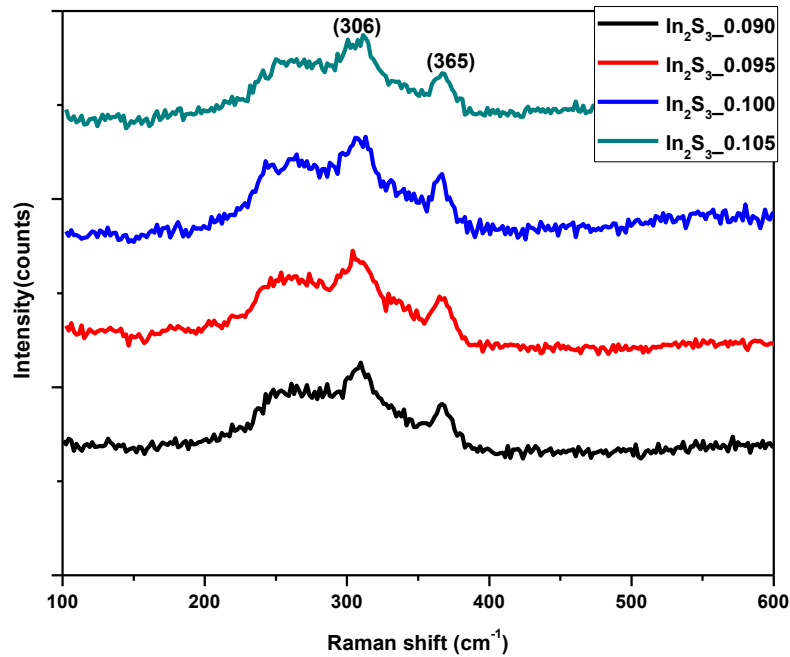


Figure 49: Raman spectra of In_2S_3 thin films.

4.2.2 Measurement of thickness

The thickness of the In_2S_3 thin films was measured with a stylus profilometer, and a graph of thickness as a function of thiourea concentration was plotted (see Figure 50). The thickness of the In_2S_3 films was increasing as the concentration of thiourea was increased from 0.090 M to 0.100 M. Mohamed et al [157] achieved a similar trend from the sprayed deposited In_2S_3 thin films that were prepared by varying precursor concentration. However, when the

concentration of thiourea was increased further to 0.105 M, we observed that the thickness of the In_2S_3 thin film decreased.

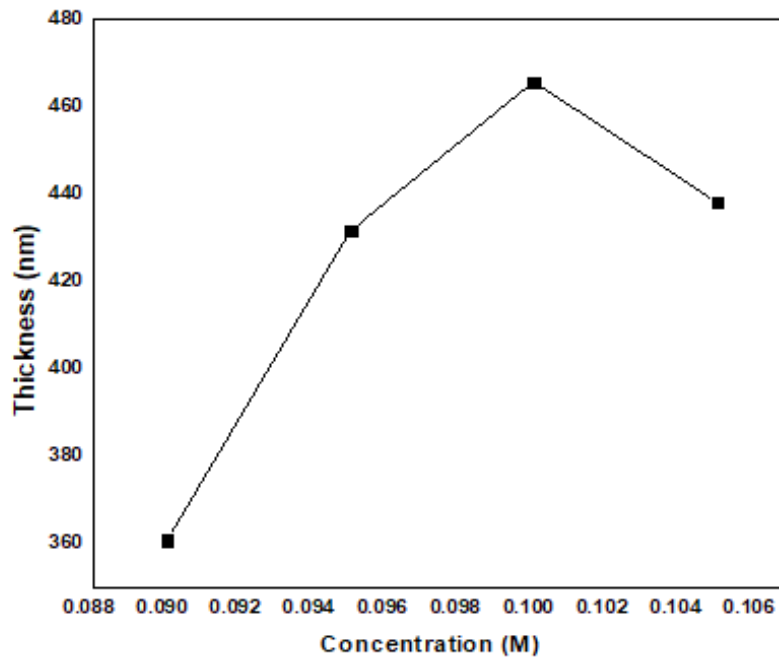


Figure 50: Thickness of In_2S_3 thin films prepared at various concentrations of thiourea.

4.2.3 Optical measurements

4.2.3.1 Transmittance and optical band gap

The optical transmittance spectra of the In_2S_3 thin films were recorded in the range from 300 nm to 1100 nm. Figure 51 shows the transmittance spectra of all sprayed In_2S_3 thin films. All In_2S_3 samples had similar spectra and fringes observed on the transmittance spectra usually arise from films with uniform thickness due to interference of reflected light [158]. Moreover, all samples show a good transparency in the visible region (from 300 nm to 800 nm) as well as in the near-infrared region of the spectrum. The average transmittance of the samples ranges from 70% to 80% in the visible region. The $\text{In}_2\text{S}_3_{0.095}$ sample shows the highest transmittance in the visible region. Moreover, the transmittance of both the $\text{In}_2\text{S}_3_{0.095}$ and $\text{In}_2\text{S}_3_{0.100}$ near the infrared region is greater than 80%. As shown by the hump between 700 nm and 800 nm on the transmittance spectra, the transmittance of the films in the visible region increased as the concentration of thiourea was increased from 0.090 M to 0.095 M, this might be associated with good formation of In_2S_3 phases and better crystallinity of a sample prepared from a solution containing 0.095 M of thiourea. However, when the concentration of thiourea was increased beyond 0.095 M the transmittance started to drop due to degrading

crystallinity. The obtained optical transmittance of the samples is similar to what others achieved in literature. Sall et al [159] reported In_2S_3 buffer layers deposited by spray pyrolysis at a temperatures ranging from 250 °C to 330 °C and the average transmittance of the layers in the visible region was lying between 50 % and 70 %.

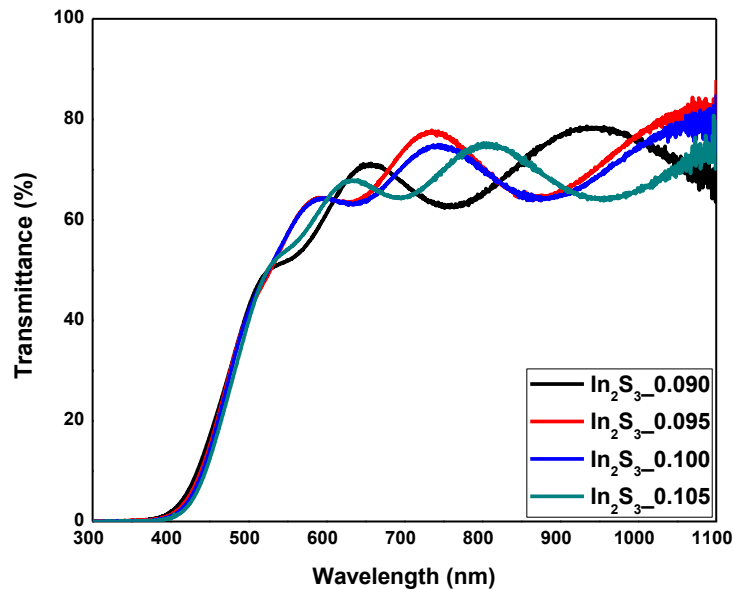


Figure 51: Transmittance spectra of spray deposited and annealed In_2S_3 thin films

The transmittance data of the samples was converted to absorbance and then the absorption coefficients of the samples were calculated using equation (22). Just like for the CZTS samples, the optical band gaps of the In_2S_3 thin films was determined by plotting the tauc^2 plots of each sample. The optical band gaps were found by extending the linear portion of the graphs towards the energy axes as shown on Figure 52. The obtained In_2S_3 thin films have wide optical band gaps ranging from 2.75 eV to 2.88 eV, which are close to values of In_2S_3 films band gaps (2.3 eV to 2.8 eV) reported in literature. Sanz et al [160] achieved the band gaps ranging from 2.58 eV to 2.73 eV from the In_2S_3 thin films that were deposited by evaporation at low temperature. Note that both the $\text{In}_2\text{S}_3_{0.095}$ and $\text{In}_2\text{S}_3_{0.100}$ thin films have larger band gap than the $\text{In}_2\text{S}_3_{0.090}$ and $\text{In}_2\text{S}_3_{105}$ thin films. Differently speaking, the results for the optical band gaps agrees with transmittance measurements since highly transparent materials have wide band gaps compared to materials that exhibit lower transmittance.

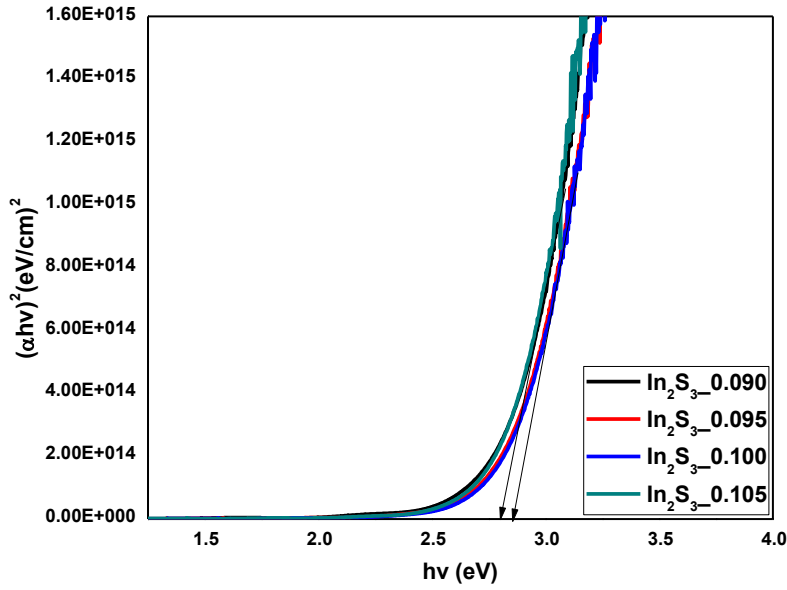


Figure 52: Optical band gaps of In_2S_3 thin films obtained by varying thiourea concentration.

4.2.4 Electrical properties

The Hall measurement system that was used to determine the electrical parameters of the CZTS thin films was also used to evaluate the electrical properties of the In_2S_3 thin films at room temperature, and the results were summarized in table 8. It was observed that the bulk concentration of the films also increased from 10^{17} cm^{-3} to 10^{18} cm^{-3} when the concentration of thiourea was increased from 0.090 M to 0.105 M. The resistivity of the In_2S_3 thin films increased from order $10^{-2} \text{ } \Omega\text{cm}$ to $10^0 \text{ } \Omega\text{cm}$ when the concentration of the thiourea was increased from 0.090 M to 0.100 M, however, then the resistivity decreased when the concentration thiourea was increased to 0.105 M. Our values of the resistivity for all In_2S_3 thin films are in range with values reported in literature. Lugo-Loredo et al [161] obtained highly resistive In_2S_3 thin films by chemical bath deposition technique, their conductivity values ranging from order $10^{-8} (\text{ } \Omega\text{cm})^{-1}$ to $10^{-3} (\text{ } \Omega\text{cm})^{-1}$. Kundakci et al [162] reported for In_2S_3 thin films which are prepared via SILAR method a very high resistivity value of about $1.5 \times 10^7 \text{ } \Omega\text{cm}$.

It was also observed that the mobility of the In_2S_3 thin films decreased from order $10^2 \text{ cm}^2/\text{Vs}$ to $10^{-1} \text{ cm}^2/\text{Vs}$ when the concentration of thiourea was increased from 0.090 M to 0.100 M. The mobility then rose up to order $10^1 \text{ cm}^2/\text{Vs}$ when the thiourea concentration was further

increased to 0.105 M. All observed values of average Hall coefficients were negative and this shows that the prepared In_2S_3 thin films were n-type.

Table 8: The bulk concentration, resistivity, mobility and average hall coefficient of In_2S_3 thin films.

Sample name	Bulk concentration (cm^{-3})	Resistivity (Ωcm)	Mobility (cm^2/Vs)	Average Hall Coefficient (cm^3/C)
$\text{In}_2\text{S}_3_{-0.090}$	-6.9956×10^{17}	5.6249×10^{-2}	1.5863×10^2	-8.9231×10^1
$\text{In}_2\text{S}_3_{-0.095}$	-1.0478×10^{18}	1.0896×10^{-1}	5.4677×10^1	-5.9576×10
$\text{In}_2\text{S}_3_{-0.100}$	-1.9538×10^{18}	4.0953×10^0	7.8012×10^{-1}	-3.1948×10
$\text{In}_2\text{S}_3_{-0.105}$	-7.5288×10^{18}	7.0257×10^{-2}	1.1801×10^1	-8.2911×10^{-1}

The electrical conductivity of the In_2S_3 thin films as a function of thiourea concentration was also studied and the results were presented using a linear graph (see Figure 53). Figure 53 reveals that the conductivity of the sprayed In_2S_3 thin films was lying between $0.2 (\Omega\text{cm})^{-1}$ and $18 (\Omega\text{cm})^{-1}$. It was further observed that the conductivity of the films dropped when the concentration of thiourea was increased from 0.090 M to 0.100 M. This might be attributed decrease in the crystallite size as observed under section 4.2.1.1 which may lead to increase of the grain boundaries, the scattering of charges at the grain boundaries may cause the resistivity to increase hence lowering the conductivity of the material. Moreover, when the concentration of thiourea was further increased to 0.105 M the conductivity increased as shown by rising portion of the graph from 0.100 M and beyond 0.100 M. The higher conductivity of $\text{In}_2\text{S}_3_{-0.090}$ might be due to excess In in the thin-films and In_2S_3 thin films with high conductivity are good candidates to be used as window layers for photovoltaic cells [163].

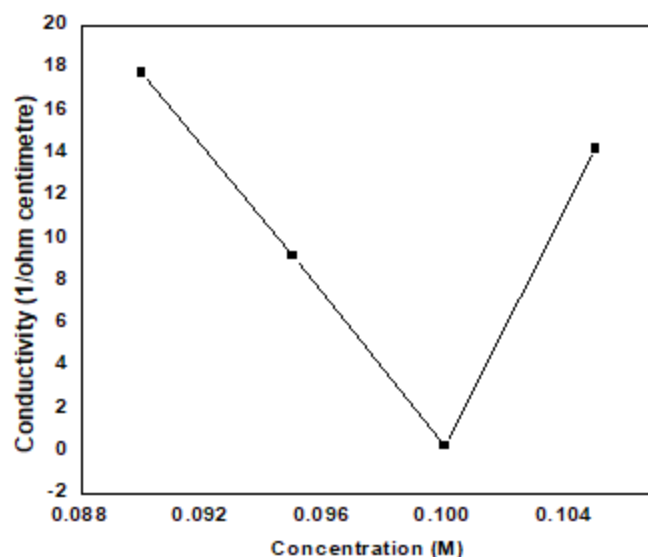


Figure 53: Conductivity of In₂S₃ thin films as a function of thiourea concentration.

4.2.5 Atomic Force Microscopy results

AFM was used to analyse the surface morphology and roughness of the In₂S₃ thin films. The AFM micrographs shown in Figure 54 indicate that all films adhered very well to the surfaces of glass substrates. In addition, the morphologies shown on the AFM micrographs indicate that the composition of In₂S₃ thin films play a very crucial role on the grain sizes. As shown on Figure 54, the samples prepared from a solution containing thiourea at a lower concentration (In₂S₃_0.090 and In₂S₃_0.095) revealed smaller grain sizes. The films grown from solutions containing thiourea at higher concentration (In₂S₃_0.100 and In₂S₃_0.105) exhibit large irregular shaped grains which might be formed by agglomeration of small grains. The roughness measurements (shown in table 9) indicate that the roughness of the In₂S₃ films depend on the composition. The roughness of the films decreased with increase in the amount of sulfur in the films. This decrease in roughness values might be associated to the large irregular shaped grains formed when the amount of S in the films increased [164].

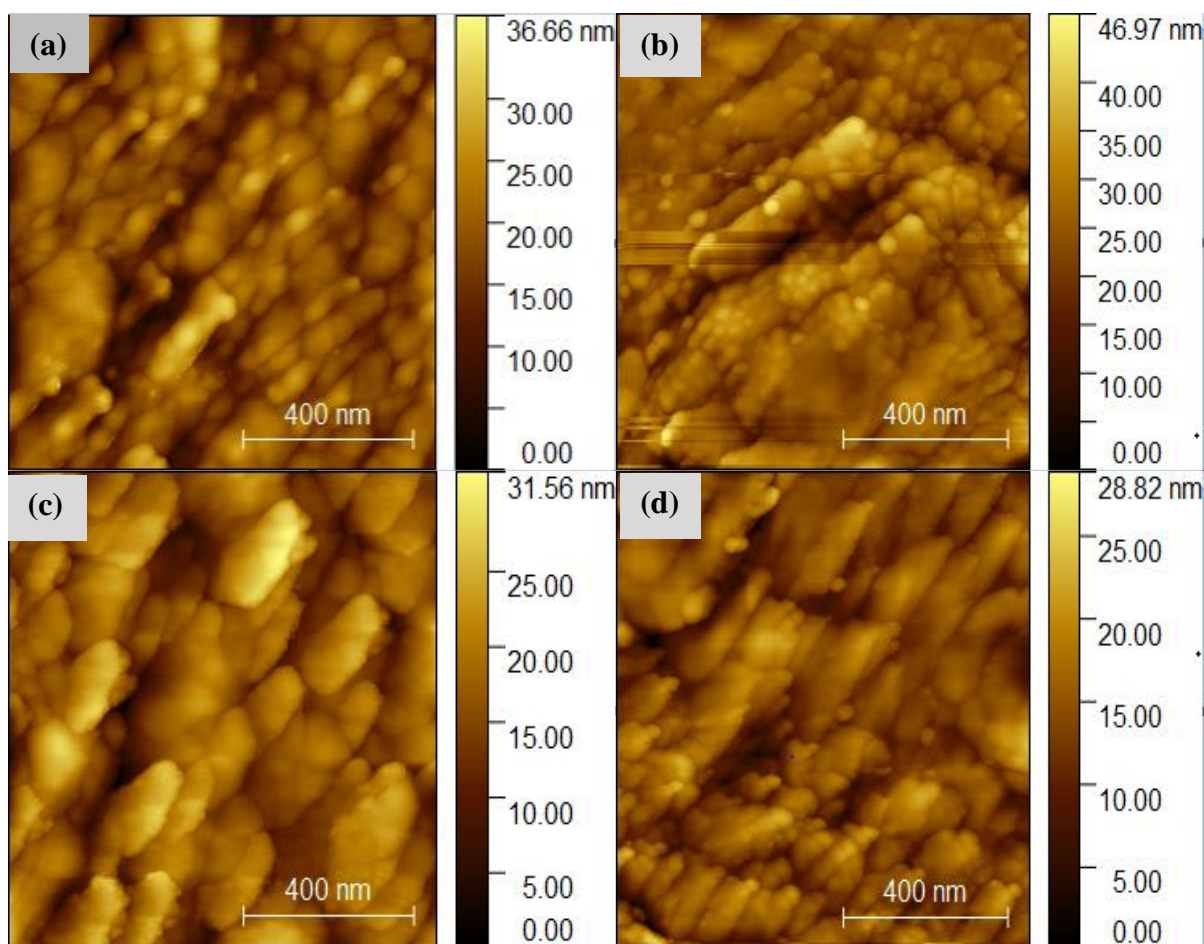


Figure 54: AFM micrographs of (a) $\text{In}_2\text{S}_3_{0.090}$, (b) $\text{In}_2\text{S}_3_{0.095}$, (c) $\text{In}_2\text{S}_3_{0.100}$ and (d) $\text{In}_2\text{S}_3_{0.105}$ thin films.

Table 9: Roughness of In_2S_3 thin films.

Sample name	Roughness (nm)
$\text{In}_2\text{S}_3_{0.090}$	2.84
$\text{In}_2\text{S}_3_{0.095}$	2.76
$\text{In}_2\text{S}_3_{0.100}$	2.70
$\text{In}_2\text{S}_3_{0.105}$	2.57

4.3 PERFORMANCE OF THE CELLS

4.3.1 The photo-conductivity of CZTS thin films

The potential of the chosen CZTS layers (CZTS001 and CZTS003) in photovoltaic applications was investigated by studying their photo-conductivity. In order to study the photo response, the CZTS absorber layer was sprayed on a FTO coated glass substrate followed by the deposition of an Ag contact on top of the CZTS layer. The current-voltage (I-V) curves of both samples were measured in the dark as well as under illumination. A solar

simulator ((AM 1.5G, 100 mW/cm²)) was used for illuminating both samples, which were kept at a temperature of 25°C. As shown in Figure 55, it was observed that illumination of both thin films (CZTS001 and CZTS003) leads to an increased current. The increment of current shows that a photo current is generated and hence the samples can be used for photovoltaic applications. It was also observed that CZTS003 has a higher current than CZTS001 both in the dark and under illumination. The higher current observed in CZTS003 compared to CZTS001 might be due to its lowest resistivity ($2.84 \times 10^{-2} \Omega/\text{cm}$) and higher mobility reported under section 4.14 (Hall measurements) [165]. In particular, for CZTS003 we observed a current increment by an order of 42% under illumination, while for CZTS001 we found a current increment by an order of 15% under illumination.

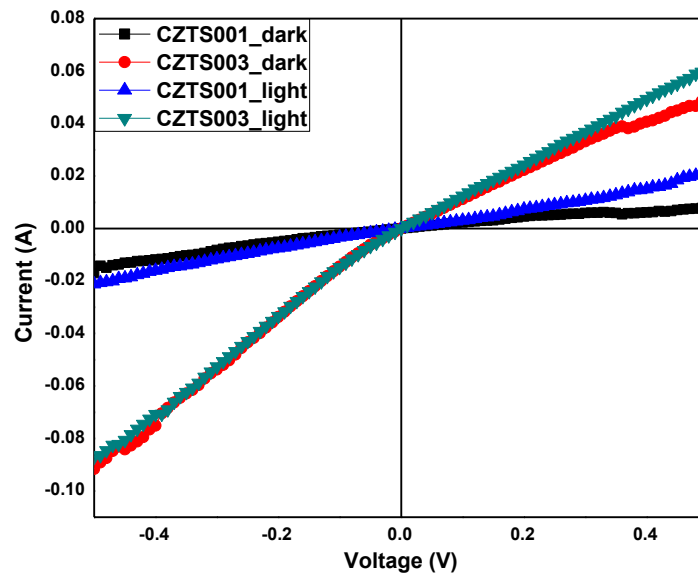


Figure 55: I-V curves of the samples CZTS001 and CZTS003 measured in the dark and under illumination.

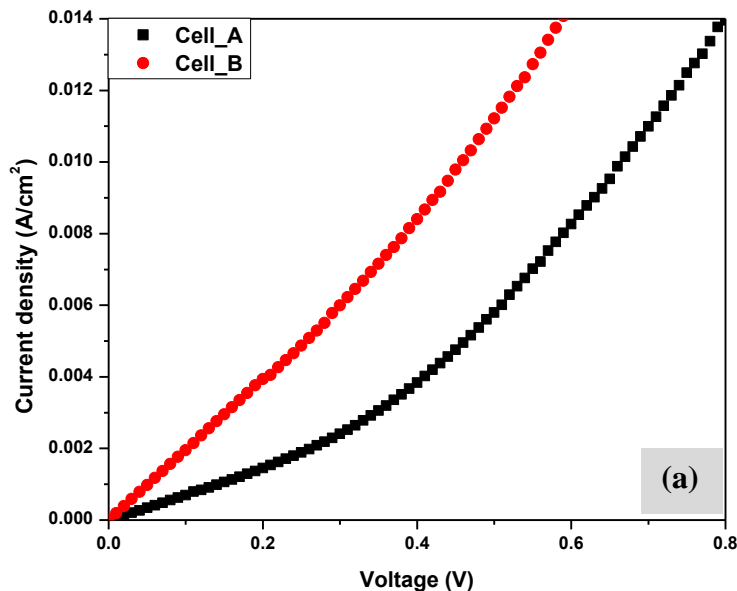
4.3.2 The I-V characteristics of the CZTS solar cells

In this section we summarize our findings for first CZTS thin film solar cell prototypes, we were able to produce in our Lab based on spray pyrolysis and RF magnetron sputtering. In order to study the performance of the produced devices (Cell-A and Cell-B), the current density – voltage (I–V) characteristics of both Cell-A and Cell-B were measured in the dark (see Figure 56(a)) and under illumination (see Figure 56(b)). In addition, the power – voltage (P–V) curves were measured under illumination (see Figure 56(c)). Table 10 summarizes the

photovoltaic parameters of both prototypes. The dark curves (shown in Figure 56 (a)) reveal that both solar cells behaved like diodes and this confirms that p-n junctions were formed between the respective CZTS absorber layer and In₂S₃ buffer layer in both prototypes. However, a straight line was obtained for Cell-B under illumination (see Figure 56 (b) and this is attributed to low shunt resistance. The values of short-circuit current density J_{SC} are 2.225 mA/cm² and 1.748 mA/cm² for Cell-A and Cell-B, respectively. Moreover, we measured an open-circuit voltage V_{OC} of 200 mV for Cell-A, while Cell-B has an open-circuit voltage of 80 mV. Low values of short-circuit current density and open-circuit voltage leads to low efficiency, the values of efficiency η at maximum power point are 0.158 % and 0.07% for Cell-A and Cell-B, respectively. The most probable power (P_{MP}) was 0.158 mW/cm² for Cell-A and 0.070 mW/cm² for Cell-B (see Figure 56(c)). The efficiencies for Cell-A and Cell-B were calculated as described under section 2.5.6 and sample calculations of efficiencies are shown below.

$$\eta_A = \frac{0.158}{100} \times 100 = 0.158 \%$$

$$\eta_B = \frac{0.070}{100} \times 100 = 0.070 \%$$



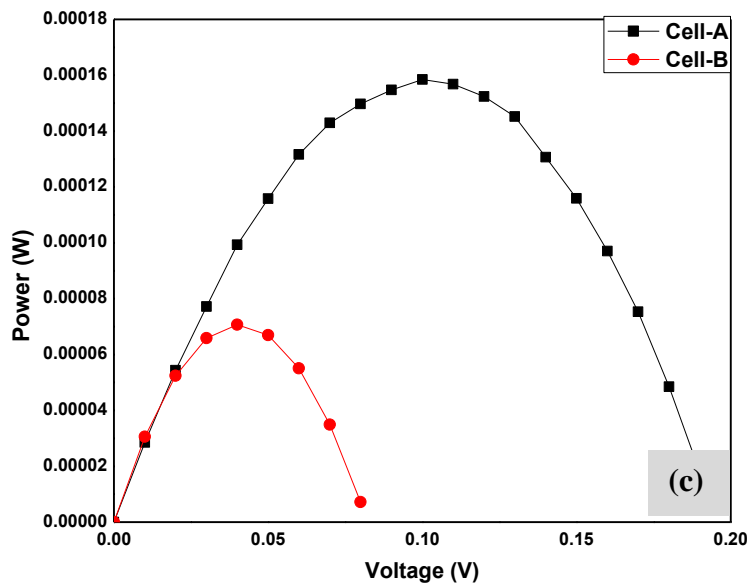
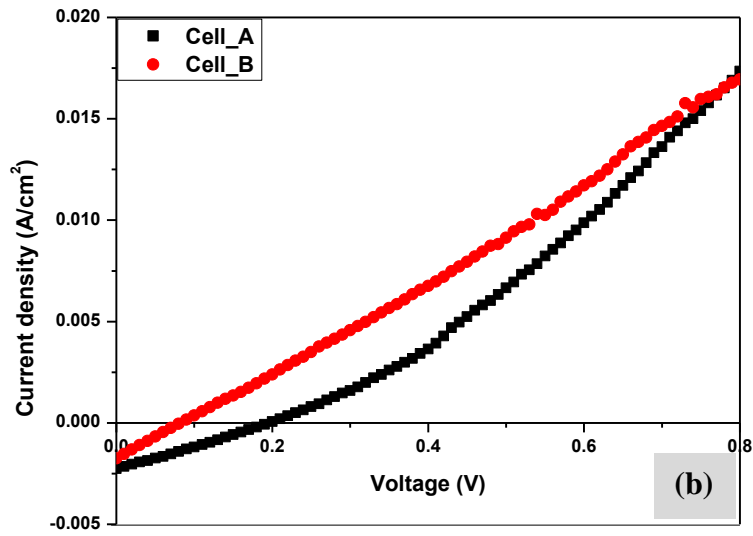


Figure 56: The (a) dark, (b) illuminated I – V characteristics and (c) P – V curves for cell-A and cell-B.

Recently D. Payno et al [166] reported the performance of CZTS solar cells with superstrate configuration. They achieved similar values of short-circuit current density (2.4 mA/cm² – 7.6 mA/cm²), the open-circuit voltage (164 mV – 258 mV) and efficiency (1.128 % - 0.518 %). R. N. Gayen and T. Chakrabarti [167] obtained superstrate type CZTS cell with a low

short-circuit current density of 0.837 mA/cm², open-circuit voltage of 285 mV and efficiency of 0.08 %. Our results for both J_{SC} and V_{OC} are in the same range with those found in literature [168],[169].

The poor performance of the sprayed CZTS solar cell prototypes might be attributed to higher values of bulk concentration and lower values of mobility of the absorber layers as observed under Hall measurement results (section 4.1.4). Moreover, values of series and shunt resistance were determined for both cell prototypes. The values of series resistance were calculated using the suns-V_{oc} method [170] and those of shunt resistance were found by calculating the inverse of the slopes for J–V curves at the point where voltage is equal to zero [171]. The values of series and shunt resistance found for Cell-A were 47.59 Ω/cm² and 105.90 Ω/cm², respectively, Cell-B had a series resistance of 11.30 Ω/cm² and shunt resistance of about 13.55 Ω/cm². Lower values of shunt resistance might be caused by poor morphology (voids and low quality of crystals) and high recombination, this also contributes to low efficiency of the cells [172].

In summary, Cell-A exhibits a higher open-circuit voltage and short-circuit current density than Cell-B due to higher crystallinity, better composition and large grain sizes of the CZTS003 absorber layer compared to CZTS001. Furthermore Cell-A has the highest efficiency of 0.158 % at the maximum power point and most probable power of about 0.158 mW/cm². This might be due lower electrical resistivity and higher photo current [146] observed for absorber layer (CZTS003) used for building Cell-A. The thickness of the absorber layer also plays an important role on the performance of a solar cell. Cell-A prepared from a thin layer (CZTS003 with thickness of 1 779.63 nm) had a better performance compared to Cell-B, which was prepared from a thick layer (CZTS001 with a thickness of 1 932.05 nm). The effect of absorber thickness had been studied by A. Tumbul et al [173], and the results revealed that decreasing thickness of the absorber layer lowers the rate of recombination and enhances the performance of a cell. They also reported that current density through thick absorber layers is decreased after reaching certain values of thickness.

Table 10: The photovoltaic parameters of Cell – A and Cell – B.

Name of the Cell	V _{oc} (mV)	I _{sc} (mA/cm ²)	FF (%)	η (%)	R _s (Ω/cm ²)	R _{sh} (Ω/cm ²)
Cell - A	200	2.26	17.53	0.158	47.59	105.90
Cell - B	80	1.75	25.25	0.070	11.30	13.55

CHAPTER 5 CONCLUSION AND RECOMMENDATIONS

5.1 Conclusion

The main aim of this work was to fabricate superstrate-type CZTS solar cells by a simple spray pyrolysis method based on different precursor solutions. In the first part of this work, CZTS thin films were successfully prepared on the borosilicate glass substrates from various precursor solutions and their properties were studied. Structural characterization confirmed the formation of CZTS thin films. According to XRD results, highly crystalline CZTS thin films were formed and all thin films were growing along the (1 1 2) direction. In addition, Raman results confirmed the formation of CZTS thin films with a more intense peak at 331 cm^{-1} . The crystallinity of the thin films was dependent on the solutions used, and it was found that a source of tin had a strong influence on the structural properties. CZTS thin films prepared from solutions containing SnCl_4 were highly crystalline compared to the CZTS thin films prepared from solution containing SnCl_2 . Furthermore, the optical and morphological properties of all CZTS thin films were also studied. The optical band gap of the sprayed CZTS thin films were varying ranging from 1.75 eV to 2.0 eV. The CZTS thin films grown from a solution containing SnCl_4 had a smaller band gap. The electrical resistivity of the sprayed CZTS layers varied between $2.84 \times 10^{-2}\ \Omega/\text{cm}$ and $1.86 \times 10^{-1}\ \Omega/\text{cm}$: the sample CZTS003 revealed the lowest resistivity.

In the second part of this work, In_2S_3 thin films were grown on glass substrates by varying the S/In ratio and characterization of those thin films was carried out. Both XRD and Raman results confirmed formation of highly crystalline $\beta\text{-In}_2\text{S}_3$ thin films. The XRD results revealed that all In_2S_3 thin films were growing along (2 2 0) plane and Raman spectra showed a major peak at 306 cm^{-1} for all In_2S_3 thin films. Increasing the amount of S degraded the crystallinity of the In_2S_3 thin films. All In_2S_3 thin films showed good transmittance (70 % - 80%) in visible and near infrared region. The films had also a wide band gap ranging from 2.75 eV to 2.88 eV. The AFM results revealed that grain size increased with the amount of S in the film and roughness decreased with the amount of S in the film. Lastly, electrical measurement revealed that the resistivity of In_2S_3 thin films increased with amount of S in the samples. However, after reaching a certain S/In ratio, the resistivity decreased.

Finally, two superstrate-type CZTS solar cell prototypes (Cell-A and Cell-B) were fabricated based on CZTS layers and an In_2S_3 layer with good energy conversion properties. The performance of the CZTS solar cell prototypes were studied. Both solar cells exhibited low

short circuit current density. The values of the short-circuit current density were 2.225 mA/cm² and 1.748 mA/cm² for Cell-A and Cell-B, respectively. The values of open-circuit voltage were 200 mV for Cell-A and 80 mV for Cell-B, respectively, which are rather low compared to theoretically possible values for CZTS solar cells. Moreover, Cell-A and Cell-B had efficiency at maximum power point of 0.158 % and 0.07 %, respectively. The rather poor performance of both solar cell prototypes was caused by large values of series resistance and small values of shunt resistance. Based on the measured photovoltaic parameters, Cell-A performed better than Cell-B, because the absorber layer that was used for fabricating Cell-A had better structural, morphological and electrical properties compared to the one used for fabricating Cell-B.

5.2 Recommendations

The objectives of this work were successfully achieved, however, there are some interesting tasks that can be carried in future to improve the performance of sprayed CZTS based solar cells, such as:

- Carry out sulfurization for the CZTS absorber layers under S and H₂S atmosphere to improve the morphology.
- Anneal the CZTS absorber layers under a vacuum or in presence of unreactive gases such as nitrogen to avoid formation of secondary phases and improve their structural, optical and electrical properties.
- Decrease thickness of the CZTS absorber layers to about 1 μm and those of In₂S₃ thin films to about 100 nm to minimize recombination.
- Perform the XPS measurements for CZTS thin films.
- Improve the contacts of cells to lower series resistance and improve the short circuit current.
- Measure the External Quantum Efficiency (EQE) for the cells.

REFERENCES

- [1] Goswami D Y, Vijayaraghavan S, Lu S and Tamm G 2004 New and emerging developments in solar energy *Sol. Energy* **76** 33–43
- [2] Fell M J 2017 Energy services: A conceptual review *Energy Res. Soc. Sci.* **27** 129–40
- [3] Khalate S A, Kate R S and Deokate R J 2018 A review on energy economics and the recent research and development in energy and the Cu₂ZnSnS₄ (CZTS) solar cells: A focus towards efficiency *Sol. Energy* **169** 616–33
- [4] Brunet C, Savadogo O, Baptiste P and Bouchard M A 2018 Shedding some light on photovoltaic solar energy in Africa – A literature review *Renew. Sustain. Energy Rev.* **96** 325–42
- [5] Lotfalipour M R, Falahi M A and Ashena M 2010 Economic growth, CO₂ emissions, and fossil fuels consumption in Iran *Energy* **35** 5115–20
- [6] Yue D, You F and Darling S B 2014 Domestic and overseas manufacturing scenarios of silicon-based photovoltaics: Life cycle energy and environmental comparative analysis *Sol. Energy* **105** 669–78
- [7] Agency I E, Joule P- and Co-operation E 2017 Solar Radiation 2.1 13–28
- [8] Ketlogetswe C and Mothudi T H 2009 Solar home systems in Botswana — Opportunities and constraints **13** 1675–8
- [9] Wang Z 2019 Chapter 1 - Introduction *Design of Solar Thermal Power Plants* ed Z Wang (Academic Press) pp 1–46
- [10] Pitz-Paal R 2013 *Solar Energy - Concentrating Solar Power* (Elsevier Ltd)
- [11] Shubbak M H 2019 Advances in solar photovoltaics: Technology review and patent trends *Renew. Sustain. Energy Rev.* **115** 109383
- [12] Phillips L 2018 *Solar energy* (Elsevier Inc.)
- [13] Gloeckler M, Sankin I and Zhao Z 2013 CdTe solar cells at the threshold to 20% efficiency *IEEE J. Photovoltaics* **3** 1389–93
- [14] Reinhard P, Chirilă A, Blösch P, Pianezzi F, Nishiwaki S, Buechelers S and Tiwari A N 2012 Review of progress toward 20% efficiency flexible CIGS solar cells and manufacturing issues of solar modules *Conf. Rec. IEEE Photovolt. Spec. Conf.*
- [15] Suryawanshi M P, Agawane G L, Bhosale S M, Shin S W, Patil P S, Kim J H and Moholkar A V. 2013 CZTS based thin film solar cells: A status review *Mater. Technol.* **28** 98–109
- [16] Ravindiran M and Praveenkumar C 2018 Status review and the future prospects of CZTS based solar cell – A novel approach on the device structure and material modeling for CZTS based photovoltaic device *Renew. Sustain. Energy Rev.* **94** 317–29
- [17] Ennaoui A, Lux-Steiner M, Weber A, Abou-Ras D, Kötschau I, Schock H W, Schurr R, Hölzing A, Jost S, Hock R, Voß T, Schulze J and Kirbs A 2009 Cu₂ZnSnS₄ thin

- film solar cells from electroplated precursors: Novel low-cost perspective *Thin Solid Films* **517** 2511–4
- [18] Yan C, Liu F, Sun K, Song N, Stride J A, Zhou F, Hao X and Green M 2016 Boosting the efficiency of pure sulfide CZTS solar cells using the In/Cd-based hybrid buffers *Sol. Energy Mater. Sol. Cells* **144** 700–6
- [19] Liu X, Guo J, Hao R, Zhao Q, Chang F, Wang L, Liu B, Li Y and Gu K 2019 Cliff-like conduction band offset at CdS/Cu₂ZnSnS₄ heterojunction prepared by sputtering CuSn alloy target using different stacking order *Sol. Energy* **183** 285–92
- [20] Djinkwi Wanda M, Ouédraogo S and Ndjaka J M B 2019 Theoretical analysis of minority carrier lifetime and Cd-free buffer layers on the CZTS based solar cell performances *Optik (Stuttg)*. **183** 284–93
- [21] Kumar M, Dubey A, Adhikari N, Venkatesan S and Qiao Q 2015 Strategic review of secondary phases, defects and defect-complexes in kesterite CZTS-Se solar cells *Energy Environ. Sci.* **8** 3134–59
- [22] Robles R, Barreau N, Vega A, Marsillac S, Bernède J C and Mokrani A 2005 Optical properties of large band gap β -In₂S_{3-3x}O_{3x} compounds obtained by physical vapour deposition *Opt. Mater. (Amst)*. **27** 647–53
- [23] Barreau N, Marsillac S, Bernède J C, Ben Nasrallah T and Belgacem S 2001 Optical properties of wide band gap indium sulphide thin films obtained by physical vapor deposition *Phys. Status Solidi Appl. Res.* **184** 179–86
- [24] Sudhakar Y N, Selvakumar M and Bhat D K 2018 *Biopolymer Electrolytes for Solar Cells and Electrochemical Cells*
- [25] Tiantian Z 2018 *High efficiency plants and building integrated renewable energy systems*
- [26] Schwarz A and Van Langenhove L 2013 *Types and processing of electro-conductive and semiconducting materials for smart textiles* (Woodhead Publishing Limited)
- [27] Haraoubia B 2018 Nonlinear Two-terminal Devices *Nonlinear Electron. I* 1–81
- [28] Poole C and Darwazeh I 2016 *Microwave semiconductor materials and diodes*
- [29] Thompson M T 2014 *Review of Diode Physics and the Ideal (and Later, Nonideal) Diode*
- [30] El-saba M 2018 *Introduction to Microelectronic & Nanoelectronic Devices*
- [31] Fortunato E, Gaspar D, Duarte P, Pereira L, Águas H, Vicente A, Dourado F, Gama M and Martins R 2016 *NanoCellulose* (Elsevier B.V.)
- [32] Stepniak G, Schüppert M and Bunge C A 2017 *Polymer-optical fibres for data transmission*
- [33] Viswanath A K 2001 Chapter 3 - SURFACE AND INTERFACIAL RECOMBINATION IN SEMICONDUCTORS *Handbook of Surfaces and Interfaces of Materials* ed H S Nalwa (Burlington: Academic Press) pp 217–84

- [34] Meyaard D S, Lin G B, Cho J and Schubert E F 2014 Efficiency droop in gallium indium nitride (GaInN)/gallium nitride (GaN) LEDs *Nitride Semicond. Light. Diodes Mater. Technol. Appl.* 279–300
- [35] Fu H and Zhao Y 2018 9 - Efficiency droop in GaInN/GaN LEDs *Nitride Semiconductor Light-Emitting Diodes (LEDs) (Second Edition)* Woodhead Publishing Series in Electronic and Optical Materials ed J Huang, H-C Kuo and S-C Shen (Woodhead Publishing) pp 299–325
- [36] Wurfel P 2005 *Physics of solar cells* (Weinheim: WILEY-VCH Verlag GmbH & Co, KGaA)
- [37] Rusirawan D and Farkas I 2014 Identification of model parameters of the photovoltaic solar cells *Energy Procedia* **57** 39–46
- [38] Jones M 2014 Chapter 4 - Test Equipment Principles *Building Valve Amplifiers (Second Edition)* ed M Jones (Oxford: Newnes) pp 235–380
- [39] Courtier N E 2020 Interpreting ideality factors for planar perovskite solar cells: Ectypal diode theory for steady-state operation *Phys. Rev. Appl.* **14** 1
- [40] Brooks A E 2013 Solar Energy. Photovoltaics. *Futur. Energy Improv. Sustain. Clean Options our Planet* 383–404
- [41] Cuevas A 2014 The recombination parameter J_0 *Energy Procedia* **55** 53–62
- [42] Seki K, Furube A and Yoshida Y 2015 Theoretical limit of power conversion efficiency for organic and hybrid halide perovskite photovoltaics *Jpn. J. Appl. Phys.* **54**
- [43] Dincer I and Rosen M A 2021 Chapter 11 - Exergy analyses of renewable energy systems *Exergy (Third Edition)* ed I Dincer and M A Rosen (Elsevier) pp 241–324
- [44] Reusch M, Bivour M, Hermle M and Glunz S W 2013 Fill factor limitation of silicon heterojunction solar cells by junction recombination *Energy Procedia* **38** 297–304
- [45] Ray B and Alam M A 2012 Achieving fill factor above 80% in organic solar cells by charged interface *Conf. Rec. IEEE Photovolt. Spec. Conf.*
- [46] Benda V 2020 18 - Photovoltaics, Including New Technologies (Thin Film) and a Discussion on Module Efficiency *Future Energy (Third Edition)* ed T M Letcher (Elsevier) pp 375–412
- [47] Rühle S 2016 Tabulated values of the Shockley-Queisser limit for single junction solar cells *Sol. Energy* **130** 139–47
- [48] Kodigala S R 2010 Chapter 1 - Introduction *Cu(InGa)Se₂ Based Thin Film Solar Cells Thin Films and Nanostructures* vol 35, ed S R Kodigala (Academic Press) pp 1–19
- [49] Shockley W and Queisser H J 1961 Detailed balance limit of efficiency of p-n junction solar cells *J. Appl. Phys.* **32** 510–9
- [50] Irvine S J C 2012 *Photovoltaic (PV) thin-films for solar cells* (Woodhead Publishing Limited)

- [51] Zhu H, Hüpkes J, Bunte E, Owen J and Huang S M 2011 Novel etching method on high rate ZnO:Al thin films reactively sputtered from dual tube metallic targets for silicon-based solar cells *Sol. Energy Mater. Sol. Cells* **95** 964–8
- [52] Green M A 2007 Thin-film solar cells: Review of materials, technologies and commercial status *J. Mater. Sci. Mater. Electron.* **18** 15–9
- [53] Chopra K L, Paulson P D and Dutta V 2004 Thin-film solar cells: an overview *Prog. Photovoltaics Res. Appl.* **12** 69–92
- [54] Hegedus S S and Shafarman W N 2004 Thin-film solar cells: Device measurements and analysis *Prog. Photovoltaics Res. Appl.* **12** 155–76
- [55] Green M A 2002 Third generation photovoltaics: Solar cells for 2020 and beyond *Phys. E Low-Dimensional Syst. Nanostructures* **14** 65–70
- [56] Kim S, Chung J W, Lee H, Park J, Heo Y and Lee H M 2013 Remarkable progress in thin-film silicon solar cells using high-efficiency triple-junction technology *Sol. Energy Mater. Sol. Cells* **119** 26–35
- [57] Badawy W A 2015 A review on solar cells from Si-single crystals to porous materials and Quantum dots *J. Adv. Res.* **6** 123–32
- [58] Jayawardena K D G I, Rozanski L J, Mills C A, Beliatas M J, Nismy N A and Silva S R P 2013 “Inorganics-in-Organics”: Recent developments and outlook for 4G polymer solar cells *Nanoscale* **5** 8411–27
- [59] Choubey P C, Oudhia A and Dewangan R 2009 Recent research in science and technology : an international refereed journal for all aspects of science research. *Recent Res. Sci. Technol.* **4** 99–101
- [60] Jeager-Waldau A 2011 Photovoltaic Status Report 2011 - Research, Solar Cell Production and Market Implementation of Photovoltaics *Eur. Comm.*
- [61] JÄGER-WALDAU A 2018 *JRC Science for policy report. PV status report 2018*
- [62] Lloyd B and Forest A S 2010 The transition to renewables: Can PV provide an answer to the peak oil and climate change challenges? *Energy Policy* **38** 7378–94
- [63] Tyagi V V., Rahim N A A, Rahim N A and Selvaraj J A L 2013 Progress in solar PV technology: Research and achievement *Renew. Sustain. Energy Rev.* **20** 443–61
- [64] Jimbo K, Kimura R, Kamimura T, Yamada S, Maw W S, Araki H, Oishi K and Katagiri H 2007 Cu₂ZnSnS₄ -type thin film solar cells using abundant materials **515** 5997–9
- [65] Katagiri H, Jimbo K, Maw W S, Oishi K, Yamazaki M, Araki H and Takeuchi A 2009 Development of CZTS-based thin film solar cells *Thin Solid Films* **517** 2455–60
- [66] Shin S W, Pawar S M, Park C Y, Yun J H, Moon J H, Kim J H and Lee J Y 2011 Studies on Cu₂ZnSnS₄ (CZTS) absorber layer using different stacking orders in precursor thin films *Sol. Energy Mater. Sol. Cells* **95** 3202–6
- [67] Nguyen M, Ernits K, Tai K F, Ng C F, Pramana S S, Sasangka W A, Batabyal S K,

- Holopainen T, Meissner D, Neisser A and H.Wong L 2015 ZnS buffer layer for Cu₂ZnSn(SSe)₄ monograin layer solar cell *Sol. Energy* **111** 344–9
- [68] Siebentritt S, Kampschulte T, Bauknecht A, Blieske U, Harneit W, Fiedeler U and Lux-Steiner M 2002 Cd-free buffer layers for CIGS solar cells prepared by a dry process *Sol. Energy Mater. Sol. Cells* **70** 447–57
- [69] Spiering S, Hariskos D, Powalla M, Naghavi N and Lincot D 2003 CD-free Cu(In,Ga)Se₂ thin-film solar modules with In₂S₃ buffer layer by ALCVD *Thin Solid Films* **431–432** 359–63
- [70] Ferhati H and Djeflal F 2018 Graded band-gap engineering for increased efficiency in CZTS solar cells *Opt. Mater. (Amst)*. **76** 393–9
- [71] Izatt R M, Izatt S R, Bruening R L, Izatt N E and Moyer B A 2014 Challenges to achievement of metal sustainability in our high-tech society *Chem. Soc. Rev.* **43** 2451–75
- [72] Schorr S 2011 Solar Energy Materials & Solar Cells The crystal structure of kesterite type compounds : A neutron and X-ray diffraction study *Sol. Energy Mater. Sol. Cells* **95** 1482–8
- [73] Wang W, Chen G, Cai H, Chen B, Yao L, Yang M, Chen S and Huang Z 2018 The effects of SnS₂ secondary phases on Cu₂ZnSnS₄ solar cells: A promising mechanical exfoliation method for its removal *J. Mater. Chem. A* **6** 2995–3004
- [74] Olekseyuk I D, Dudchak I V. and Piskach L V. 2004 Phase equilibria in the Cu₂S-ZnS-SnS₂ system *J. Alloys Compd.* **368** 135–43
- [75] Jung H R, Shin S W, Gurav K V., Suryawanshi M P, Hong C W, Yang H S, Lee J Y, Moon J H and Kim J H 2015 Phase evolution of Cu₂ZnSnS₄ (CZTS) kesterite thin films during the sulfurization process *Ceram. Int.* **41** 13006–11
- [76] Tanaka T, Yoshida A, Saiki D, Saito K, Guo Q, Nishio M and Yamaguchi T 2010 Influence of composition ratio on properties of Cu₂ZnSnS₄ thin films fabricated by co-evaporation *Thin Solid Films* **518** 29–33
- [77] Shinde N M, Deokate R J and Lokhande C D 2013 Properties of spray deposited Cu₂ZnSnS₄ (CZTS) thin films *J. Anal. Appl. Pyrolysis* **100** 12–6
- [78] Vigil-Galán O, Courel M, Espindola-Rodriguez M, Jiménez-Olarte D, Aguilar-Frutis M and Saucedo E 2015 Electrical properties of sprayed Cu₂ZnSnS₄ thin films and its relation with secondary phase formation and solar cell performance *Sol. Energy Mater. Sol. Cells* **132** 557–62
- [79] González J C, Fernandes P A, Ribeiro G M, Abelenda A, Viana E R, Salomé P M P and Da Cunha A F 2014 Influence of the sulphurization time on the morphological, chemical, structural and electrical properties of Cu₂ZnSnS₄ polycrystalline thin films *Sol. Energy Mater. Sol. Cells* **123** 58–64
- [80] Gurav K V., Pawar S M, Shin S W, Suryawanshi M P, Agawane G L, Patil P S, Moon J H, Yun J H and Kim J H 2013 Electrosynthesis of CZTS films by sulfurization of CZT precursor: Effect of soft annealing treatment *Appl. Surf. Sci.* **283** 74–80

- [81] Pawar S M, Moholkar A V, Kim I K, Shin S W, Moon J H, Rhee J I and Kim J H 2010 Effect of laser incident energy on the structural , morphological and optical properties of $\text{Cu}_2\text{ZnSnS}_4$ (CZTS) thin films *Curr. Appl. Phys.* **10** 565–9
- [82] Rao S, Morankar A, Verma H and Goswami P 2016 Emerging Photovoltaics: Organic, Copper Zinc Tin Sulphide, and Perovskite-Based Solar Cells *J. Appl. Chem.* **2016** 1–12
- [83] Barkhouse D A R, Haight R, Sakai N, Hiroi H, Sugimoto H and Mitzi D B 2012 Cd-free buffer layer materials on $\text{Cu}_2\text{ZnSn}(\text{S}_x\text{Se}_{1-x})_4$: Band alignments with ZnO , ZnS , and In_2S_3 *Appl. Phys. Lett.* **100**
- [84] Kim J, Park C, Pawar S M, Inamdar A I, Jo Y, Han J, Hong J, Park Y S, Kim D Y, Jung W, Kim H and Im H 2014 Optimization of sputtered ZnS buffer for $\text{Cu}_2\text{ZnSnS}_4$ thin film solar cells *Thin Solid Films* **566** 88–92
- [85] Cui X, Sun K, Lee C, Yan C, Sun H, Zhang Y, Liu F, Hoex B, Hao X, Engineering R E and Sydney U 2018 ALD ZnSnO buffer layer for enhancing heterojunction interface quality of CZTS solar cells 1511–3
- [86] Cui X, Sun K, Lee C Y, Yan C, Sun H, Zhang Y, Liu F, Green M, Hoex B and Hao X 2018 ALD ZnSnO buffer layer for enhancing heterojunction interface quality of CZTS solar cells *2018 IEEE 7th World Conf. Photovolt. Energy Conversion, WCPEC 2018 - A Jt. Conf. 45th IEEE PVSC, 28th PVSEC 34th EU PVSEC* 1511–3
- [87] Luan H, Yao B, Li Y, Liu R, Ding Z, Sui Y, Zhang Z, Zhao H and Zhang L 2019 Influencing mechanism of cationic ratios on efficiency of $\text{Cu}_2\text{ZnSn}(\text{S},\text{Se})_4$ solar cells fabricated with DMF-based solution approach *Sol. Energy Mater. Sol. Cells* **195** 55–62
- [88] Saha S 2020 A Status Review on $\text{Cu}_2\text{ZnSn}(\text{S}, \text{Se})_4$ -Based Thin-Film Solar Cells *Int. J. Photoenergy* **2020**
- [89] Zeng X, Fai K, Zhang T, Wan C, Ho J, Chen X, Huan A, Chien T and Wong L H 2014 Solar Energy Materials & Solar Cells $\text{Cu}_2\text{ZnSn}(\text{S}, \text{Se})_4$ kesterite solar cell with 5.1 % efficiency using spray pyrolysis of aqueous precursor solution followed by selenization *Sol. Energy Mater. Sol. Cells* **124** 55–60
- [90] Vigil-Galán O, Espíndola-Rodríguez M, Courel M, Fontané X, Sylla D, Izquierdo-Roca V, Fairbrother A, Saucedo E and Pérez-Rodríguez A 2013 Secondary phases dependence on composition ratio in sprayed $\text{Cu}_2\text{ZnSnS}_4$ thin films and its impact on the high power conversion efficiency *Sol. Energy Mater. Sol. Cells* **117** 246–50
- [91] Tong Z, Yan C, Su Z, Zeng F, Yang J, Li Y, Jiang L, Lai Y and Liu F 2014 Effects of potassium doping on solution processed kesterite $\text{Cu}_2\text{ZnSnS}_4$ thin film solar cells *Appl. Phys. Lett.* **105**
- [92] Tiwari D, Koehler T, Lin X, Harniman R, Griffiths I, Wang L, Cherns D, Klenk R and Fermin D J 2016 $\text{Cu}_2\text{ZnSnS}_4$ Thin Films Generated from a Single Solution Based Precursor: The Effect of Na and Sb Doping *Chem. Mater.* **28** 4991–7
- [93] Karade V, Lokhande A, Babar P, Gang M G, Suryawanshi M, Patil P and Kim J H 2019 Insights into kesterite's back contact interface: A status review *Sol. Energy*

Mater. Sol. Cells **200** 109911

- [94] Kim J, Kang J and Hwang D 2016 High efficiency bifacial Cu₂ZnSnSe₄ thin- film solar cells on transparent conducting oxide glass substrates **096101**
- [95] Nazligul A S, Wang M and Choy K L 2020 Recent development in earth-abundant kesterite materials and their applications *Sustain.* **12**
- [96] Yan C, Huang J, Sun K, Johnston S, Zhang Y, Sun H, Pu A, He M, Liu F, Eder K, Yang L, Cairney J M, Ekins-Daukes N J, Hameiri Z, Stride J A, Chen S, Green M A and Hao X 2018 Cu₂ZnSnS₄ solar cells with over 10% power conversion efficiency enabled by heterojunction heat treatment *Nat. Energy* **3** 764–72
- [97] Quero J M, Perdignes F and Aracil C 2013 *Microfabrication technologies used for creating smart devices for industrial applications* (Woodhead Publishing Limited)
- [98] Grèzes-Besset C and Chauveau G 2013 *Optical coatings for large facilities* (Woodhead Publishing Limited)
- [99] Adeyeye A O and Shimon G 2015 *Growth and Characterization of Magnetic Thin Film and Nanostructures* vol 5 (Elsevier B.V.)
- [100] Shi C, Shi G, Chen Z, Yang P and Yao M 2012 Deposition of Cu₂ZnSnS₄ thin films by vacuum thermal evaporation from single quaternary compound source *Mater. Lett.* **73** 89–91
- [101] Jiang X, Shao L X, Zhang J, Li D, Xie W, Zou C W and Chen J M 2013 Preparation of Cu₂ZnSnS₄ thin films by sulfurization of metallic precursors evaporated with a single source *Surf. Coatings Technol.* **228** 408–11
- [102] Michelmore A 2016 *Thin film growth on biomaterial surfaces* (Elsevier Ltd)
- [103] Zafar M S, Farooq I, Awais M, Najeeb S, Khurshid Z and Zohaib S 2019 *Bioactive Surface Coatings for Enhancing Osseointegration of Dental Implants* (Elsevier Ltd.)
- [104] Tanaka T, Nagatomo T, Kawasaki D, Nishio M, Guo Q, Wakahara A, Yoshida A and Ogawa H 2005 Preparation of Cu₂ZnSnS₄ thin films by hybrid sputtering *J. Phys. Chem. Solids* **66** 1978–81
- [105] Sun L, He J, Chen Y, Yue F, Yang P and Chu J 2012 Comparative study on Cu₂ZnSnS₄ thin films deposited by sputtering and pulsed laser deposition from a single quaternary sulfide target *J. Cryst. Growth* **361** 147–51
- [106] Inamdar A I, Lee S, Jeon K Y, Lee C H, Pawar S M, Kalubarme R S, Park C J, Im H, Jung W and Kim H 2013 Optimized fabrication of sputter deposited Cu₂ZnSnS₄ (CZTS) thin films *Sol. Energy* **91** 196–203
- [107] Buonomenna M G 2016 *Smart composite membranes for advanced wastewater treatments 14.1 Introduction 14.1.1 Why smart composite membranes for wastewater treatment?*
- [108] Sakka S 2013 *Sol-Gel Process and Applications* (Elsevier)
- [109] Tanaka K, Oonuki M, Moritake N and Uchiki H 2009 Cu₂ZnSnS₄ thin film solar

- cells prepared by non-vacuum processing *Sol. Energy Mater. Sol. Cells* **93** 583–7
- [110] Tanaka K, Fukui Y, Moritake N and Uchiki H 2011 Chemical composition dependence of morphological and optical properties of Cu₂ZnSnS₄ thin films deposited by sol-gel sulfurization and Cu₂ZnSnS₄ thin film solar cell efficiency *Sol. Energy Mater. Sol. Cells* **95** 838–42
- [111] Maeda K, Tanaka K, Fukui Y and Uchiki H 2011 Influence of H₂S concentration on the properties of Cu₂ZnSnS₄ thin films and solar cells prepared by solgel sulfurization *Sol. Energy Mater. Sol. Cells* **95** 2855–60
- [112] Ashour A, Kaid M A, El-Sayed N Z and Ibrahim A A 2006 Physical properties of ZnO thin films deposited by spray pyrolysis technique *Appl. Surf. Sci.* **252** 7844–8
- [113] Sumanth Kumar D, Jai Kumar B and Mahesh H M 2018 *Quantum Nanostructures (QDs): An Overview* (Elsevier Ltd.)
- [114] Gavrilović T V., Jovanović D J and Dramićanin M D 2018 Synthesis of multifunctional inorganic materials: From micrometer to nanometer dimensions *Nanomater. Green Energy* 55–81
- [115] Perednis D and Gauckler L J 2005 Thin Film Deposition Using Spray Pyrolysis 103–11
- [116] Kamoun N, Bouzouita H and Rezig B 2007 Fabrication and characterization of Cu₂ZnSnS₄ thin films deposited by spray pyrolysis technique **515** 5949–52
- [117] Kumar Y B K, Babu G S, Bhaskar P U and Ā V S R 2009 Solar Energy Materials & Solar Cells Preparation and characterization of spray-deposited Cu₂ZnSnS₄ thin films *Sol. Energy Mater. Sol. Cells* **93** 1230–7
- [118] Rajeshmon V G, Kartha C S, Vijayakumar K P, Sanjeeviraja C, Abe T and Kashiwaba Y 2011 Role of precursor solution in controlling the opto-electronic properties of spray pyrolysed Cu₂ZnSnS₄ thin films *Sol. Energy* **85** 249–55
- [119] Douglas C. Giancoli 2014 Diffraction and Polarization *Phys. Sci. Eng. with Mod. Phys.* **5** 921–50
- [120] Le Pevelen D D 2010 Small Molecule X-Ray Crystallography, Theory and Workflow *Encyclopedia of Spectroscopy and Spectrometry (Second Edition)* ed J C Lindon (Oxford: Academic Press) pp 2559–76
- [121] Worsfold P J 2005 SPECTROPHOTOMETRY | Overview *Encyclopedia of Analytical Science (Second Edition)* ed P Worsfold, A Townshend and C Poole (Oxford: Elsevier) pp 318–21
- [122] Mayerhöfer T G, Pahlow S and Popp J 2020 The Bouguer-Beer-Lambert Law: Shining Light on the Obscure *ChemPhysChem*
- [123] Kafle B P 2020 Chapter 6 - Introduction to nanomaterials and application of UV–Visible spectroscopy for their characterization *Chemical Analysis and Material Characterization by Spectrophotometry* ed B P Kafle (Elsevier) pp 147–98
- [124] Shinato K W, Huang F and Jin Y 2020 Principle and application of atomic force

- microscopy (AFM) for nanoscale investigation of metal corrosion *Corros. Rev.* **38** 423–32
- [125] Light M and Better W 2019 Small Area Solar Simulators SciSun series Features Small Area Solar Simulators SciSun series **0135** 1–6
- [126] Formulator T and Four S M U Section 6 Make I-V measurements on a solar cell 1–10
- [127] Rajeshmon V G, Menon M R R, Kartha C S and Vijayakumar K P 2014 Effect of copper concentration and spray rate on the properties Cu₂ZnSnS₄ thin films deposited using spray pyrolysis *J. Anal. Appl. Pyrolysis* **110** 448–54
- [128] Khalate S A, Kate R S, Kim J H, Pawar S M and Deokate R J 2017 Effect of deposition temperature on the properties of Cu₂ZnSnS₄ (CZTS) thin films *Superlattices Microstruct.* **103** 335–42
- [129] Chtouki T, Soumahoro L, Kulyk B, Bougharraf H, Erguig H, Ammous K and Sahraoui B 2017 Comparative Study on the Structural, Morphological, Linear and Nonlinear Optical Properties of CZTS Thin Films Prepared by Spin-Coating and Spray Pyrolysis *Mater. Today Proc.* **4** 5146–53
- [130] Ganesh Kumar C, Pombala S, Poornachandra Y and Vinod Agarwal S 2016 Chapter 4 - Synthesis, characterization, and applications of nanobiomaterials for antimicrobial therapy *Nanobiomaterials in Antimicrobial Therapy* ed A M Grumezescu (William Andrew Publishing) pp 103–52
- [131] Nithin K S, Shilpa K N, Thimmaiah R, Jagajeevan Raj B M, Sachhidananda S and Siddaramaiah H 2021 4 - Tools and techniques toward characterizing polymer-based smart composites for optical, optoelectronic, and energy-related applications†Deceased. *Polymer-Based Advanced Functional Composites for Optoelectronic and Energy Applications* ed N K Subramani, H Siddaramaiah and J H Lee (Elsevier) pp 91–115
- [132] Kumar V, Dutta A and Singh U P 2020 Optimization of selenization parameters for fabrication of CZTSe thin film *Superlattices Microstruct.* **144** 106578
- [133] Kattan N, Hou B, Fermín D J and Cherns D 2015 Crystal structure and defects visualization of Cu₂ZnSnS₄ nanoparticles employing transmission electron microscopy and electron diffraction *Appl. Mater. Today* **1** 52–9
- [134] Fan J, Chen R, Fan J, Li H, Liu C and Mai Y 2018 Subject Category : Subject Areas : Authors for correspondence : Efficiency enhancement of Cu₂ZnSnS₄ solar cells via surface treatment engineering
- [135] Dimitrievska M, Boero F, Litvinchuk A P, Delsante S, Borzone G, Perez-Rodriguez A and Izquierdo-Roca V 2017 Structural Polymorphism in “Kesterite” Cu₂ZnSnS₄: Raman Spectroscopy and First-Principles Calculations Analysis *Inorg. Chem.* **56** 3467–74
- [136] Thiruvankadam S, Prabhakaran S, Chakravarty S, Ganesan V, Sathe V, Santhosh Kumar M C and Leo Rajesh A 2018 Effect of Zn/Sn molar ratio on the microstructural and optical properties of Cu₂Zn_{1-x}Sn_xS₄ thin films prepared by spray pyrolysis technique *Phys. B Condens. Matter* **533** 22–7

- [137] Valdés M, Santoro G and Vázquez M 2014 Spray deposition of Cu₂ZnSnS₄ thin films *J. Alloys Compd.* **585** 776–82
- [138] Zhang J and Jung Y G 2017 *Advanced Ceramic and Metallic Coating and Thin Film Materials for Energy and Environmental Applications*
- [139] Islam S, Hossain M A, Kabir H, Rahaman M, Bashar M S, Gafur M A, Kabir A, R Bhuiyan M M, Ahmed F and Khatun N 2015 Optical, Structural and Morphological Properties of Spin Coated Copper Zinc Tin Sulfide Thin Films *Int. J. Thin Film. Sci. Technol.* **4** 155
- [140] Al-Saadi T M, Hussein B H, Hasan A B and Shehab A A 2019 Study the structural and optical properties of Cr doped SnO₂ nanoparticles synthesized by sol-gel method *Energy Procedia* **157** 457–65
- [141] Mir F A 2014 Transparent wide band gap crystals follow indirect allowed transition and bipolaron hopping mechanism *Results Phys.* **4** 103–4
- [142] Thiruvankadam S, Jovina D and Leo Rajesh A 2014 The influence of deposition temperature in the photovoltaic properties of spray deposited CZTS thin films *Sol. Energy* **106** 166–70
- [143] Vanalakar S A, Shin S W, Agawane G L, Suryawanshi M P, Gurav K V., Patil P S and Kim J H 2014 Effect of post-annealing atmosphere on the grain-size and surface morphological properties of pulsed laser deposited CZTS thin films *Ceram. Int.* **40** 15097–103
- [144] Diwate K, Mohite K, Shinde M, Rondiya S, Pawbake A, Date A, Pathan H and Jadkar S 2017 Synthesis and Characterization of Chemical Spray Pyrolysed CZTS Thin Films for Solar Cell Applications *Energy Procedia* **110** 180–7
- [145] Kodigala S R 2014 *The Role of Characterization Techniques in the Thin Film Analysis*
- [146] Tanaka T, Yoshida A, Saiki D, Saito K, Guo Q, Nishio M and Yamaguchi T 2010 Influence of composition ratio on properties of Cu₂ZnSnS₄ thin films fabricated by co-evaporation **518** 29–33
- [147] Bhosale S M, Suryawanshi M P, Kim J H and Moholkar A V. 2015 Influence of copper concentration on sprayed CZTS thin films deposited at high temperature *Ceram. Int.* **41** 8299–304
- [148] Chalapathi U, Uthanna S and Sundara Raja V 2015 Growth of Cu₂ZnSnS₄ thin films by a two-stage process - Effect of incorporation of sulfur at the precursor stage *Sol. Energy Mater. Sol. Cells* **132** 476–84
- [149] Mahewar R B 2020 Structure, morphology and optical parameters of spray deposited CZTS thin films for solar cell applications *Indian J. Sci. Technol.* **13** 2149–56
- [150] Choudhari N J, Raviprakash Y, Bellarmine F, Ramachandra Rao M S and Pinto R 2020 Investigation on the sulfurization temperature dependent phase and defect formation of sequentially evaporated Cu-rich CZTS thin films *Sol. Energy* **201** 348–61
- [151] Arba Y, Rafi M, Hartiti B, Ridah A and Thevenin P 2011 Preparation and Properties

- of Czts Thin Film Prepared By Spray Pyrolysis *Moroccan J. Condens. Matter* **13** 100–2
- [152] Espindola-rodriguez M, Placidi M, Vigil-galán O, Izquierdo-roca V, Fontané X and Fairbrother A 2013 Compositional optimization of photovoltaic grade Cu₂ZnSnS₄ films grown by pneumatic spray pyrolysis *Thin Solid Films* **535** 67–72
- [153] Jayakrishnan R 2018 Photoluminescence in Spray Pyrolysis Deposited β -In₂S₃ Thin Films *J. Electron. Mater.* **47** 2249–56
- [154] Soulantica K, Erades L, Sauvan M, Senocq F, Maisonnat A and Chaudret B 2003 Synthesis of indium and indium oxide nanoparticles from indium cyclopentadienyl precursor and their application for gas sensing *Adv. Funct. Mater.* **13** 553–7
- [155] Kärber E, Otto K, Katerski A, Mere A and Krunks M 2014 Raman spectroscopic study of In₂S₃ films prepared by spray pyrolysis *Mater. Sci. Semicond. Process.* **25** 137–42
- [156] Elfarrass S, Hartiti B, Ridah A and Thevenin P 2015 Effect of different S/In ratio of In₂S₃ films prepared by chemical spray pyrolysis method *J. Mater. Environ. Sci.* **6** 487–90
- [157] Raj Mohamed J and Amalraj L 2016 Effect of precursor concentration on physical properties of nebulized spray deposited In₂S₃ thin films *J. Asian Ceram. Soc.* **4** 357–66
- [158] Ahmed N M, Sauli Z, Hashim U and Al-douri Y 2009 Investigation of the absorption coefficient, refractive index, energy band gap, and film thickness for Al_{0.11}Ga_{0.89}N by optical transmission method *Int. J. Nanoelectron. Mater.* **2** 189–95
- [159] Sall T, Marí Soucase B, Mollar M, Hartitti B and Fahoume M 2015 Chemical spray pyrolysis of β -In₂S₃ thin films deposited at different temperatures *J. Phys. Chem. Solids* **76** 100–4
- [160] Sanz C, Guillén C, Gutiérrez M T and Herrero J 2013 Investigation of optical, structural, and chemical properties of indium sulfide thin films evaporated at low temperature by modulated flux deposition *Phys. Status Solidi Appl. Mater. Sci.* **210** 320–6
- [161] Lugo-Loredo S, Peña-Méndez Y, Calixto-Rodríguez M, Messina-Fernández S, Alvarez-Gallegos A, Vázquez-Dimas A and Hernández-García T 2014 Indium sulfide thin films as window layer in chemically deposited solar cells *Thin Solid Films* **550** 110–3
- [162] Kundakci M, Ateş A, Astam A and Yildirim M 2008 Structural, optical and electrical properties of CdS, Cd_{0.5}In_{0.5}S and In₂S₃ thin films grown by SILAR method *Phys. E Low-Dimensional Syst. Nanostructures* **40** 600–5
- [163] Calixto-Rodríguez M, Tiburcio-Silver A, Ortiz A and Sanchez-Juarez A 2005 Optoelectronic properties of indium sulfide thin films prepared by spray pyrolysis for photovoltaic applications *Thin Solid Films* **480–481** 133–7
- [164] Spasevska H, Kitts C C, Ancora C and Ruani G 2012 Optimised In₂S₃ thin films deposited by spray pyrolysis *Int. J. Photoenergy* **2012**

- [165] Ananthoju B, Mohapatra J, Jangid M K, Bahadur D, Medhekar N V. and Aslam M 2016 Cation/Anion Substitution in Cu₂ZnSnS₄ for Improved Photovoltaic Performance *Sci. Rep.* **6** 1–11
- [166] Payno D, Kazim S, Salado M and Ahmad S 2021 Sulfurization temperature effects on crystallization and performance of superstrate CZTS solar cells *Sol. Energy* **224** 1136–43
- [167] Gayen R N and Chakrabarti T 2019 Effect of series and shunt resistance on the photovoltaic properties of solution-processed zinc oxide nanowire based CZTS solar cell in superstrate configuration *Mater. Sci. Semicond. Process.* **100** 1–7
- [168] Lee D and Yang J Y 2020 Superstrate structured FTO/TiO₂/In₂S₃/Cu₂ZnSnS₄ solar cells fabricated by a spray method with aqueous solutions *Coatings* **10** 9–11
- [169] Fathima M I, Arulanantham A M S and Wilson K S J 2019 Effect of ZnS nanowire ARC on CZTS/CdS thin film solar cell by Nebulizer Spray Pyrolysis Technique *Mater. Res. Express* **7** 0–12
- [170] Hansen C W and King B H 2019 Determining Series Resistance for Equivalent Circuit Models of a PV Module *IEEE J. Photovoltaics* **9** 538–43
- [171] Ma L, Xu L, Zhang K, Wu W and Ma Z 2011 The measurement of series and shunt resistances of the silicon solar cell based on LabVIEW 2011 *Int. Conf. Electr. Control Eng. ICECE 2011 - Proc.* 2711–4
- [172] Zhong M, Liu S, Li H and Li C 2018 Superstrate-type Cu₂ZnSnS₄ solar cells without sulfurization fabricated by spray pyrolysis *Chalcogenide Lett.* **15** 133–7
- [173] Tumbul A, Aslan F, Göktaş A and Mutlu I H 2019 All solution processed superstrate type Cu₂ZnSnS₄ (CZTS) thin film solar cell: Effect of absorber layer thickness *J. Alloys Compd.* **781** 280–8